Membrane topology inversion of GGCX mediates cytoplasmic carboxylation for antiviral defense

Tomohiko Okazaki[1,2,3]*, Keiji Nozaki[2], Nao Morimoto[1], Yuta Otobe[4], Riho Saito[2], Shuntaro Abe[1], Miyuki Okajima[2], Hikari Yoshitane[3,4,5], Tomohisa Hatta[6], Shun-ichiro Iemura[7], Tohru Natsume[8], Hidetaka Kosako[9], Miwako Yamasaki[10], Satoshi Inoue[11,12], Takashi Kondo[13], Haruhiko Koseki[14] & Yukiko Gotoh[2,15]

[1] Institute for Genetic Medicine, Graduate School of Life Science, Hokkaido University, Sapporo, Japan.

[2]Graduate School of Pharmaceutical Sciences, University of Tokyo, Tokyo, Japan.

[3]Japan Science and Technology Agency (JST) Fusion Oriented Research for Disruptive Science and Technology (FOREST) Program, Kawaguchi, Japan.

[4]Circadian Clock Project, Tokyo Metropolitan Institute of Medical Science, Tokyo, Japan.

[5]Department of Biological Sciences, School of Science, The University of Tokyo, Tokyo, Japan.

[6]Robotic Biology Institute, Inc., Tokyo, Japan.

[7]Translational Research Center, Fukushima Medical University, Fukushima, Japan.

[8]Molecular Profiling Research Center for Drug Discovery, National Institute of Advanced Industrial Science and Technology, Tokyo, Japan.

[9]Institute of Advanced Medical Sciences, Tokushima University, Tokushima, Japan.

[10]Department of Anatomy, Faculty of Medicine, Hokkaido University, Sapporo, Japan.

[11]Department of Systems Aging Science and Medicine, Tokyo Metropolitan Institute of Gerontology, Itabashi, Tokyo, Japan.

[12]Research Center for Genomic Medicine, Saitama Medical University, Hidaka, Saitama, Japan.

[13]Laboratory for Developmental Genetics, RIKEN Center for Integrative Medical Sciences (RIKEN-IMS), Yokohama, Japan.

[14]International Research Center for Neurointelligence (WPI-IRCN), University of Tokyo, Tokyo, Japan.

*Corresponding author. Email: okazaki@igm.hokudai.ac.jp

Abstract: Mitochondrial antiviral signaling protein (MAVS) is an adaptor involved in antiviral immunity, but its regulation is not fully understood. We identified carboxylation of MAVS by vitamin K (VK)-dependent γ-glutamyl carboxylase (GGCX), which was unexpected due to the reported membrane topology of GGCX. We found that GGCX could undergo topology inversion to carboxylate MAVS within the cytoplasm. This carboxylation enhanced the ability of MAVS to induce interferon while suppressing the induction of apoptosis. Genetic knockout of GGCX, a VK-free diet, or depletion of VK by inhibiting vitamin K epoxide reductase 1 with warfarin increased viral susceptibility in mice. Thus, we identified a MAVS regulatory mechanism, the existence of cytoplasmic protein carboxylation and topological inversion of GGCX, and demonstrated how modulating VK levels may influence antiviral defense.

One-Sentence Summary: Vitamin K-dependent ‘cytoplasmic’ carboxylation of MAVS suppresses apoptosis and promotes antiviral interferon responses

Main Text: Innate immune responses of mammalian cells to viral infection include the production of interferons (IFNs) and the execution of apoptosis (*1-3*). Type I IFNs such as IFN-α and IFN-β induce the expression of hundreds of IFN-stimulated genes (ISGs) that play a major role in restricting viral replication within infected cells, whereas apoptosis eliminates infected cells to prevent further viral spread (*2, 3*). These IFN-mediated and apoptotic responses appear to be differentially regulated in a context-dependent manner upon viral infection, with clearance of infected cells by apoptosis considered beneficial in tissues with a high regenerative capacity (such as skin and lung)(*4*) but detrimental in those in which regeneration rarely occurs (such as brain). Recognition of viral RNA within the host cell by pattern recognition receptors including retinoic acid-inducible gene I (RIG-I)-like receptors (RLRs) such as RIG-I and melanoma differentiation-associated protein 5 (MDA5) (*5, 6*), results in the activation of mitochondrial antiviral signaling protein (MAVS) (*7-10*), a transmembrane protein that localizes to mitochondria and peroxisomes and plays an essential role in mediating both IFN and apoptosis responses (*11, 12*). However, the molecular mechanisms that control the switch between these two arms of the MAVS-mediated antiviral defense system remain unclear.

Results

MAVS is carboxylated in its cytoplasmic domain by GGCX

To explore the molecular mechanisms that underlie discrimination between MAVS-mediated antiviral responses, we investigated post-translational modification (PTM) of MAVS by performing mass spectrometric analysis of a decahistidine (His_{10})- and Flag epitope-tagged NH_2-terminal fragment (ΔC) of human MAVS (hMAVS) expressed in HEK293T (293T) cells. Since detecting PTMs of endogenous MAVS was challenging due to its low abundance, we overexpressed MAVS for facilitating identification of its PTMs. Recombinant MAVS protein was isolated from cell lysates under denaturing conditions to prevent artifactual PTMs (Fig. S1A, B). We identified carboxylation at residues Asp^{53}, Glu^{70}, Glu^{80}, and Asp^{83} of hMAVS, all of which are located in the cytoplasmic domain of the protein (Fig. 1A and Fig. S1C, Fig. S2A). In addition, the His_{10}-Flag-tagged full-length hMAVS protein expressed in 293T cells was recognized by a commercially available antibody against pan-carboxylated Glu (Gla), which detects Gla residues in proteins irrespective of species specificity, in immunoblot analysis (Fig. 1B).

In addition, we generated a rabbit polyclonal antibody to recognize the Glu80-carboxylated (Gla80) form of mouse MAVS (mMAVS), which detected His_{10}-Flag-mMAVS in 293T cells (Fig. 1C and Fig. S3A). A mutant of mMAVS, in which Glu80 was replaced with alanine (mMAVS(E80A)), as well as a double mutant in which both Glu70 and Glu80 were replaced with alanine (mMAVS(2EA)), were not detected by the anti-Gla80 antibodies (Fig. 1C and Fig. S3B). Knockdown of γ-glutamyl carboxylase (GGCX), which adds a carboxyl group to glutamate or aspartate residues (*13-15*), reduced MAVS carboxylation detected by anti-Gla80 antibodies (Fig. 1C). We also found that carboxylation of mMAVS at Gla80 gradually increased following VSV infection 293T cells (Fig. 1D, Fig. S4A-C). Furthermore, we generated knock-in (KI) mice where the sequence encoding His_{10}-tag was inserted so that it would be expressed at the N-terminus of the endogenous MAVS protein to facilitate isolation of endogenous mMAVS from primary mouse tissues (Fig. S5). Using lysates from the liver of these KI mice, we found that endogenous mMAVS was indeed recognized by pan-Gla antibodies (Fig. 1E).

Detection of cytoplasmic carboxylation using a reporter

GGCX is a transmembrane protein that resides on membranes of the endoplasmic reticulum (ER) and its activity is dependent on vitamin K (VK), an essential dietary nutrient. VK can be depleted by warfarin, which inhibits vitamin K epoxide reductase 1. Approximately 20 protein substrates of GGCX have been identified (*16*-*18*) and all are exclusively extracellular or reside within the ER lumen. This is consistent with the catalytic domain of GGCX being reported to face the luminal side of ER and unable to access to cytoplasmic targets (*19*). In general, membrane proteins have a fixed orientation and misoriented membrane proteins are destined to be corrected as an error (*20*-*24*). Therefore, GGCX was not thought to carboxylate proteins in the cytoplasm given its membrane topology. Our finding that cytoplasmic carboxylation of MAVS was dependent on GGCX was, thus, unexpected (Fig. 1C). The N-terminal domains of MAVS (MAVS ΔC) and full-length MAVS overexpressed in 293T cells, as well as endogenous His_{10}-tag KI MAVS in MEFs, were localized to either the cytosolic or the extraorganellar space of the organelle fraction, indicating that they were not mistargeted to the ER lumen (fig. S6A-D).

We examined whether GGCX was able to carboxylate cytoplasmic substrates by generating a cytoplasmic Gla reporter (cytoGla) consisting of tandemly repeated Gla domains and a conserved recognition sequence (CRS) for GGCX as well as a nuclear export signal (NES) (Fig. S7A). Carboxylation of cytoGla was detected in 293T cells in the presence, but not the absence, of vitamin K (VK), a cofactor for GGCX (Fig. 1F). Carboxylation of cytoGla was lost in cells where endogenous GGCX had been depleted (Fig. 1G). Moreover, carboxylation of cytoGla was only detected when MAVS or a constitutively active form of RIG-I or MDA5 was overexpressed (Fig. 1F and Fig. S8A). Subcellular fractionation and immunostaining confirmed that MAVS overexpression increased cytoGla carboxylation in the cytoplasm (Fig. 1H, I).

These results suggested that cytoplasmic proteins were potential targets of carboxylation by GGCX, and that the RLR-MAVS pathway promoted such cytoplasmic carboxylation.

Topology inversion of GGCX

We considered that one potential mechanism of cytoplasmic carboxylation may be inversion of GGCX topology. GGCX is described as a type II integral membrane protein with multiple N-linked glycosylation sites in its C-terminal region (*25*). If the topology of GGCX were to be inverted, the C-terminal domain would be localized in the cytoplasm, which would be expected to result in loss of glycosylation (Fig. 2A). We expressed Myc-tagged GGCX in 293T cells, and analyzed its apparent molecular weight by SDS-PAGE and immunoblotting. We observed a slower-migrating band (Fig. S9A), designated GGCX(A), in addition to a band migrating according to the expected molecular weight (88 kDa), designated GGCX(B). The faster migration of GGCX(B) appeared to be due to lack of glycosylation in its C-terminal region, given that GGCX(A), but not GGCX(B), was bound by the lectin concanavalin A (ConA) and that treatment with endoglycosidase H (EndoH) reduced the apparent molecular size only of GGCX(A), resulting in the merging of both bands into one migrating at the position of GGCX(B) (Fig. 2B).

MAVS expression did not overtly affect the overall level or localization of GGCX (Fig. S9B-C). The relative abundance of GGCX(B) was greatly increased by forced expression of MAVS or a constitutively active form of RIG-I or MDA5 (Fig. 2B and Fig. S8B)

We explored whether loss of glycosylation of GGCX(B) corresponded to a change of its topology. We performed a split mNeonGreen2 (mNG2) assay, in which the mNG2 protein is divided into two non-fluorescent fragments, $mNG2_{1–10}$ and $mNG2_{11}$. Fluorescence is only detected

when these fragments are brought into proximity and reconstituted in the same subcellular compartment (Fig. 2C and Fig. S9D). A low level of mNG2 fluorescence was detected when KDEL-tagged (ER-localized) $mNG2_{1–10}$ and N-terminally $mNG2_{11}$-tagged GGCX were coexpressed in 293T cells (Fig. 2D), indicating that a small fraction of GGCX existed with type III topology. The intensity of this signal increased by overexpression of MAVS (Fig. 2D).

We investigated other proteins inserted into the ER membrane, transmembrane 4 six family member 20 (TM4SF20) and cluster of differentiation 38 (CD38), and did not detect their topology changed upon MAVS expression (Fig. S10A-C). In addition, we did not detected elevation of ER stress markers such as spliced X-box binding protein 1 (XBP1) and heat shock protein family A member 5 (HSPA5), suggesting that MAVS overexpression did not cause ER malfunction (Fig. S10D–G).

Stress-activated MAPK pathways, which are crucial for type I interferon induction, are known to be activated downstream of MAVS(*26*). We found that GGCX(B) was increased upon expression of active forms of mitogen-activated protein kinase (MAPK) kinase kinase (MAPKKK) apoptosis signal-regulating kinase 1 (ASK1) and MAPK kinase 6 (MKK6), both of which activate p38 MAPK (Fig. S11A). Furthermore, the increase in GGCX(B) by MAVS expression was blocked in cells expressing a dominant-negative (AGF) p38 MAPK mutant (Fig. S11B). These findings suggested that p38 MAPK may mediate MAVS-induced topology inversion of GGCX. Additionally, co-immunoprecipitation assays suggested that MAVS preferentially interacted with GGCX(B) rather than GGCX(A). Therefore, MAVS might stabilize inverted GGCX through interactions in the cytoplasm (Fig. S12A).

Mutation of MAVS carboxylation sites suppresses IFN production and promotes caspase activation

We examined whether carboxylation affected MAVS-induced production of type I IFN and activation of caspases. We generated alanine substitution mutants for each carboxylation site (D53A, E70A, E80A, and D83A) of hMAVS. Overexpression of wild-type (WT) hMAVS in 293T cells was sufficient to activate the mouse IFN-β gene (Ifnb1) promoter in a reporter assay, induce phosphorylation of interferon regulatory factor 3 (IRF3)—a critical step for IFN induction—and trigger caspase activation, as evidenced by the cleavage of both poly(ADP-ribose) polymerase (PARP) and MAVS itself (Fig. 3A, B, and Fig. S13A, B). In contrast, expression of the D53A mutant or the E70A/E80A/D83A (3A) triple mutant failed to induce IRF3 phosphorylation and subsequent IFN-β promoter activation but strongly enhanced caspase activation, as assessed by immunoblot analysis of the cleavage of both poly(ADP-ribose) polymerase (PARP) and MAVS itself (Fig. 3B and Fig. S13B). Treatment with the pan-caspase inhibitor zVAD did not rescue IRF3 phosphorylation by these carboxylation-deficient MAVS mutants (Fig. S14A), suggesting that suppression of *Ifnb1* expression was not a secondary effect of enhanced cell death. We concluded that mutation of the carboxylation sites of MAVS did not inhibit overall protein function, but rather induced a switch in regulation from type I IFN induction to caspase activation.

To determine the role of MAVS carboxylation in immune defense, we used mouse embryonic fibroblasts (MEFs) derived from MAVS knockout (KO) mice and expressed either WT or 3A mutant forms of mMAVS. We then examined the responses to polyinosinic-polycytidylic acid poly(I:C) double-stranded RNA (as a model of RNA virus infection) and to infection with vesicular stomatitis virus (VSV). Poly(I:C) and VSV infection increased the levels of *Ifnb1* mRNA and IRF3 phosphorylation in MEFs expressing WT mMAVS but not in those expressing the 3A

mutant (Fig. 3C, D, and Fig. S15A, B). By contrast, the extent of VSV-induced PARP cleavage was greater in cells expressing the 3A mutant of mMAVS than in those expressing the WT protein (Fig. S15B). The titer of VSV in culture supernatants at 24 h after infection was higher for MEFs expressing the 3A mutant than for those expressing WT mMAVS (Fig. 3E). The effects of the MAVS 3A mutation on *Ifnb1* expression and viral replication were observed even in the presence of zVAD (Fig. S16A–C). Together, these results indicated that carboxylation of MAVS played a role in the induction of IFN-β in response to viral RNA, and in the suppression of viral expansion.

GGCX promotes type I IFN production and inhibits caspase activation

As mutation of MAVS carboxylation sites altered its function, we investigated how GGCX influenced antiviral responses. Depletion of GGCX in HeLa S3 cells attenuated the increase in *IFNB1* mRNA and IRF3 phosphorylation, as well as in enhancement of PARP cleavage induced by poly(I:C) treatment (Fig. 3F, G). Depletion of GGCX in the neuronal cell line N2a attenuated interferon-inducing signaling but enhanced caspase activation in response to VSV infection (Fig. S17A). The effect of GGCX RNAi on *IFNB1* induction in HeLa S3 cells was observed even in the presence of zVAD (Fig. S18A, B). Overexpression of mGGCX in 293T cells promoted hMAVS-induced *IFNB1* expression without affecting the abundance of *MAVS* mRNA (Fig. 3H and Fig. S19A) and inhibited hMAVS-induced caspase-3 cleavage (Fig. 3I). However, these effects of mGGCX were not observed with the MAVS 4A mutant (Fig. S20A–C). Furthermore, mGGCX overexpression did not affect *IFNB1* expression (Fig. S19B) or caspase-3 activation (Fig. 3I) induced by TANK binding kinase 1 (TBK1), suggesting that GGCX regulated the switch from caspase activation to type I IFN induction through MAVS rather than its downstream mediator TBK1.

We treated HeLa S3 cells with warfarin to deplete VK and found that it inhibited poly(I:C)-mediated induction of *IFNB1* mRNA (Fig. S21A). In addition, warfarin enhanced PARP cleavage induced by poly(I:C) transfection in these cells (Fig. S21B). These results supported the conclusion that VK-dependent carboxylation of MAVS by GGCX promoted the type I IFN response and, in parallel, suppresses the apoptotic response to viral infection.

Proteomic identification of MAVS carboxylation site-associated proteins

We hypothesized that proteins that specifically associated with either carboxylated or noncarboxylated MAVS may account for the functional switch between IFN induction and caspase activation. We used mass spectrometry to identify proteins differentially bound by Flag-tagged WT or a carboxylation-deficient form of hMAVS (4A, with the substitutions D53A, E70A, E80A, and D83A) isolated from 293T cells.

Among the differentially associated proteins, we found that the translocase of outer mitochondrial membrane (TOMM) subunit TOMM40 associated preferentially with the 4A mutant form of MAVS relative to the WT protein (Fig. 4A, and Data S1). This preferential association was confirmed by co-immunoprecipitation (Fig. 4B). We also found that overexpression of hTOMM40 enhanced MAVS-mediated caspase activation but not IRF-3 phosphorylation, and attenuated MAVS-mediated IFN-β induction in 293T cells (Fig. 4C, D). Conversely, knockdown of TOMM40 inhibited MAVS-mediated caspase activation but had little effect on MAVS-mediated IRF3 phosphorylation and IFN-β induction in HeLa S3 cells (Fig. 4E,

F). These results indicated that TOMM40, which associated preferentially with MAVS 4A rather than MAVS WT, selectively promoted MAVS-mediated caspase activation.

We searched for a potential mediator of the effect of MAVS carboxylation on type I IFN induction. Our proteomics analysis revealed that Polo-like kinase 1 (PLK1), known to inhibit MAVS-mediated IRF3 activation (*27*), was also preferentially associated with the 4A mutant of MAVS compared with the WT protein (Fig. 4A). We confirmed the specificity of the interaction by co-immunoprecipitation (Fig. 4B). We concluded that carboxylation site-dependent effectors of MAVS such as TOMM40 and PLK1 may mediate its carboxylation-dependent functional switch.

GGCX and VK protect against viral infection *in vivo*

Given the relatively high level of GGCX activity in the brain (*28*), we investigated its role in defense against intranasal VSV infection of mouse brain (*29*). Tissue immune responses often involve resident cells as well as infiltrating immune cells such as myeloid cells. To assess the role of GGCX in these distinct cell populations, we selectively deleted *Ggcx* in neural and myeloid cells using the mouse Nestin gene (*Nes*) or LysM gene (*Lyz2*) promoters, respectively, to drive the expression of Cre recombinase in mice homozygous for a floxed allele of *Ggcx* ($Ggcx^{fl/fl}$ mice). Ablation of GGCX in neural or myeloid cells of these mice did not appear to affect the overall development or survival rate of mice in the absence of infection (Fig. 5A, B and Fig. S22A, B). However, loss of GGCX in neural cells, but not in myeloid cells, attenuated mouse survival after intranasal VSV infection (Fig. 5A, B and Fig. S22A, B). Deletion of *Ggcx* in neural cells, but not in myeloid cells, increased the titer of VSV in brain homogenates, which reflect overall immune responses in the brain (Fig. 5C and Fig. S22C). Moreover, the extent of VSV-induced expression of IFN-α and IFN-β genes in the brain was lower in mice lacking GGCX in neural cells than in control animals (Fig. 5D). The extent of VSV-induced caspase-3 cleavage in the brain was increased by ablation of GGCX in neural cells (Fig. 5E).

We concluded that GGCX in neural cells protects the central nervous system (CNS) against viral infection, and skews antiviral responses away from apoptosis and toward type I IFN induction *in vivo*.

As the activity of GGCX is dependent on VK, we examined how modulating VK availability in mice impacted antiviral responses. We fed a cohort of WT mice a VK-free diet for four weeks and administered the antibiotic cefotiam hydrochloride to both VK-free and control diets to deplete VK-producing bacteria in the gut. The bodyweight of mice fed the VK-free diet did not differ from that of mice fed the control diet (Fig. S23A, B). However, the VK-free diet exacerbated loss of bodyweight and increased the viral titer in the brain after intranasal VSV infection (Fig. S23C, D). We examined whether warfarin treatment, which suppressed VK-dependent protein carboxylation, attenuated antiviral defense *in vivo*. WT mice were treated with warfarin or vehicle for 4 weeks, then infected intranasally with VSV (Fig. 5F). Although warfarin treatment alone did not affect mouse survival, it decreased the survival rate after VSV infection (Fig. 5G). Furthermore, the viral titer in brain homogenates was higher for warfarin-treated mice than control mice (Fig. 5H). A warfarin-induced increase in susceptibility to VSV infection was not evident in MAVS KO mice under conditions in which warfarin effectively inhibited coagulation (Fig. S24A–C). These results indicated that loss of VK ability impairs immune responses in the brains of mice in part via modulation of MAVS.

Discussion

We identified the existence of cytoplasmic protein carboxylation and its relevance to antiviral defense, demonstrating topology inversion of GGCX as a mechanism enabling this modification. While a few cases of topology inversion of transmembrane proteins have been reported in mammalian cells(*30, 31*), none have been shown to transition from type II to III in a signal-dependent manner. Our findings suggested that the RLR-MAVS-ASK1-MKK6-p38 axis may play a role in this process, although the substrates of p38 required for this inversion remain unknown.

Furthermore, given that p38 MAPK signaling is activated not only by cytoplasmic viral RNA but also by various cellular stresses including cytoplasmic viral DNA(*32, 33*), cytoplasmic protein carboxylation via topologically inverted GGCX may occur in response to infection by a wide range of viruses. Moreover, carboxylation of cytoplasmic proteins other than MAVS may be induced by GGCX topology inversion and modulate cellular functions in response to viral infection or other cellular stresses.

Carboxylation of MAVS by GGCX functions to switch MAVS activity from apoptosis induction to type I IFN induction by altering its binding partners. While the precise mechanism remains unclear, carboxylation may affect the structure or association partners of MAVS, leading to alterations in its functions or subcellular localization.

References and Notes

1. D. B. Stetson, R. Medzhitov, Type I interferons in host defense. *Immunity* **25**, 373-381 (2006).
2. R. J. Clem, L. K. Miller, Apoptosis reduces both the in vitro replication and the in vivo infectivity of a baculovirus. *J Virol* **67**, 3730-3738 (1993).
3. J. Tschopp, M. Thome, K. Hofmann, E. Meinl, The fight of viruses against apoptosis. *Curr Opin Genet Dev* **8**, 82-87 (1998).
4. S. Chattopadhyay, T. Kuzmanovic, Y. Zhang, J. L. Wetzel, G. C. Sen, Ubiquitination of the Transcription Factor IRF-3 Activates RIPA, the Apoptotic Pathway that Protects Mice from Viral Pathogenesis. *Immunity* **44**, 1151-1161 (2016).
5. M. Yoneyama *et al.*, The RNA helicase RIG-I has an essential function in double-stranded RNA-induced innate antiviral responses. *Nat Immunol* **5**, 730-737 (2004).
6. L. Gitlin *et al.*, Essential role of mda-5 in type I IFN responses to polyriboinosinic:polyribocytidylic acid and encephalomyocarditis picornavirus. *Proc Natl Acad Sci U S A* **103**, 8459-8464 (2006).
7. T. Kawai *et al.*, IPS-1, an adaptor triggering RIG-I- and Mda5-mediated type I interferon induction. *Nat Immunol* **6**, 981-988 (2005).
8. R. B. Seth, L. Sun, C. K. Ea, Z. J. Chen, Identification and characterization of MAVS, a mitochondrial antiviral signaling protein that activates NF-kappaB and IRF 3. *Cell* **122**, 669-682 (2005).
9. E. Meylan *et al.*, Cardif is an adaptor protein in the RIG-I antiviral pathway and is targeted by hepatitis C virus. *Nature* **437**, 1167-1172 (2005).
10. L. G. Xu *et al.*, VISA is an adapter protein required for virus-triggered IFN-beta signaling. *Mol Cell* **19**, 727-740 (2005).
11. J. Rintahaka, D. Wiik, P. E. Kovanen, H. Alenius, S. Matikainen, Cytosolic antiviral RNA recognition pathway activates caspases 1 and 3. *J Immunol* **180**, 1749-1757 (2008).
12. R. Besch *et al.*, Proapoptotic signaling induced by RIG-I and MDA-5 results in type I interferon-independent apoptosis in human melanoma cells. *J Clin Invest* **119**, 2399-2411 (2009).
13. B. Furie, B. A. Bouchard, B. C. Furie, Vitamin K-dependent biosynthesis of gamma-carboxyglutamic acid. *Blood* **93**, 1798-1808 (1999).
14. S. E. Hamilton, D. Tesch, B. Zerner, Vitamin K1 dependent carboxylase: beta-carboxylation of t-butyloxycarbonylaspartic acid alpha-benzyl ester. *Biochem Biophys Res Commun* **107**, 246-249 (1982).
15. J. J. McTigue, M. K. Dhaon, D. H. Rich, J. W. Suttie, Vitamin K-dependent carboxylase. Carboxylation of aspartyl residues to beta-carboxyaspartyl residues in synthetic substrates. *J Biol Chem* **259**, 4272-4278 (1984).
16. A. Zhu *et al.*, Fatal hemorrhage in mice lacking gamma-glutamyl carboxylase. *Blood* **109**, 5270-5275 (2007).
17. M. Ferron, J. Lacombe, A. Germain, F. Oury, G. Karsenty, GGCX and VKORC1 inhibit osteocalcin endocrine functions. *J Cell Biol* **208**, 761-776 (2015).
18. K. Azuma *et al.*, Liver-specific γ-glutamyl carboxylase-deficient mice display bleeding diathesis and short life span. *PLoS One* **9**, e88643 (2014).
19. K. L. Berkner, The vitamin K-dependent carboxylase. *Annu Rev Nutr* **25**, 127-149 (2005).

20. R. S. Hegde, R. J. Keenan, The mechanisms of integral membrane protein biogenesis. *Nat Rev Mol Cell Biol* **23**, 107-124 (2022).
21. M. L. Wohlever, A. Mateja, P. T. McGilvray, K. J. Day, R. J. Keenan, Msp1 Is a Membrane Protein Dislocase for Tail-Anchored Proteins. *Mol Cell* **67**, 194-202.e196 (2017).
22. P. J. Chitwood, S. Juszkiewicz, A. Guna, S. Shao, R. S. Hegde, EMC Is Required to Initiate Accurate Membrane Protein Topogenesis. *Cell* **175**, 1507-1519.e1516 (2018).
23. S. Matsumoto *et al.*, Msp1 Clears Mistargeted Proteins by Facilitating Their Transfer from Mitochondria to the ER. *Mol Cell* **76**, 191-205.e110 (2019).
24. M. J. McKenna *et al.*, The endoplasmic reticulum P5A-ATPase is a transmembrane helix dislocase. *Science* **369**, (2020).
25. J. K. Tie, M. Y. Zheng, R. M. Pope, D. L. Straight, D. W. Stafford, Identification of the N-linked glycosylation sites of vitamin K-dependent carboxylase and effect of glycosylation on carboxylase function. *Biochemistry* **45**, 14755-14763 (2006).
26. T. Okazaki *et al.*, The ASK family kinases differentially mediate induction of type I interferon and apoptosis during the antiviral response. *Sci Signal* **8**, ra78 (2015).
27. D. Vitour *et al.*, Polo-like kinase 1 (PLK1) regulates interferon (IFN) induction by MAVS. *J Biol Chem* **284**, 21797-21809 (2009).
28. E. E. Romero, L. J. Velazquez-Estades, R. Deo, B. Schapiro, D. A. Roth, Cloning of rat vitamin K-dependent gamma-glutamyl carboxylase and developmentally regulated gene expression in postimplantation embryos. *Exp Cell Res* **243**, 334-346 (1998).
29. U. Kalinke, I. Bechmann, C. N. Detje, Host strategies against virus entry via the olfactory system. *Virulence* **2**, 367-370 (2011).
30. Q. Chen *et al.*, Inverting the Topology of a Transmembrane Protein by Regulating the Translocation of the First Transmembrane Helix. *Mol Cell* **63**, 567-578 (2016).
31. B. Denard, S. Han, J. Kim, E. M. Ross, J. Ye, Regulating G protein-coupled receptors by topological inversion. *Elife* **8**, (2019).
32. K. R. Balka, D. De Nardo, Molecular and spatial mechanisms governing STING signalling. *FEBS J* **288**, 5504-5529 (2021).
33. T. Abe, G. N. Barber, Cytosolic-DNA-mediated, STING-dependent proinflammatory gene induction necessitates canonical NF-κB activation through TBK1. *J Virol* **88**, 5328-5341 (2014).
34. J. C. M. Meiring, I. Grigoriev, W. Nijenhuis, L. C. Kapitein, A. Akhmanova, Opto-katanin, an optogenetic tool for localized, microtubule disassembly. *Curr Biol* **32**, 4660-4674.e4666 (2022).
35. G. Manfioletti, C. Brancolini, G. Avanzi, C. Schneider, The protein encoded by a growth arrest-specific gene (gas6) is a new member of the vitamin K-dependent proteins related to protein S, a negative coregulator in the blood coagulation cascade. *Mol Cell Biol* **13**, 4976-4985 (1993).
36. M. Fukuda, I. Gotoh, Y. Gotoh, E. Nishida, Cytoplasmic localization of mitogen-activated protein kinase kinase directed by its NH2-terminal, leucine-rich short amino acid sequence, which acts as a nuclear export signal. *J Biol Chem* **271**, 20024-20028 (1996).
37. M. Yoneyama *et al.*, Autocrine amplification of type I interferon gene expression mediated by interferon stimulated gene factor 3 (ISGF3). *J Biochem* **120**, 160-169 (1996).
38. M. Miyagishi, K. Taira, Strategies for generation of an siRNA expression library directed against the human genome. *Oligonucleotides* **13**, 325-333 (2003).

39. K. Honda *et al.*, IRF-7 is the master regulator of type-I interferon-dependent immune responses. *Nature* **434**, 772-777 (2005).
40. H. Kumar *et al.*, Essential role of IPS-1 in innate immune responses against RNA viruses. *J Exp Med* **203**, 1795-1803 (2006).
41. F. Isaka *et al.*, Ectopic expression of the bHLH gene Math1 disturbs neural development. *Eur J Neurosci* **11**, 2582-2588 (1999).
42. M. Hashimoto, T. Takemoto, Electroporation enables the efficient mRNA delivery into the mouse zygotes and facilitates CRISPR/Cas9-based genome editing. *Sci Rep* **5**, 11315 (2015).
43. H. Tanaka *et al.*, Peroxisomes control mitochondrial dynamics and the mitochondrion-dependent apoptosis pathway. *J Cell Sci* **132**, (2019).
44. F. A. Ran *et al.*, Genome engineering using the CRISPR-Cas9 system. *Nat Protoc* **8**, 2281-2308 (2013).
45. M. Kamiyama *et al.*, ASK1 facilitates tumor metastasis through phosphorylation of an ADP receptor P2Y. *Cell Death Differ* **24**, 2066-2076 (2017).
46. S. Morita, T. Kojima, T. Kitamura, Plat-E: an efficient and stable system for transient packaging of retroviruses. *Gene Ther* **7**, 1063-1066 (2000).
47. T. Okazaki, M. Higuchi, Y. Gotoh, Mitochondrial localization of the antiviral signaling adaptor IPS-1 is important for its induction of caspase activation. *Genes Cells* **18**, 493-501 (2013).
48. I. Aoki, M. Higuchi, Y. Gotoh, NEDDylation controls the target specificity of E2F1 and apoptosis induction. *Oncogene* **32**, 3954-3964 (2013).
49. A. Yokoyama *et al.*, Multiple post-translational modifications in hepatocyte nuclear factor 4α. *Biochem Biophys Res Commun* **410**, 749-753 (2011).
50. K. Imamura *et al.*, ASK family kinases mediate cellular stress and redox signaling to circadian clock. *Proc Natl Acad Sci U S A* **115**, 3646-3651 (2018).
51. H. Yoshitane *et al.*, mTOR-AKT Signaling in Cellular Clock Resetting Triggered by Osmotic Stress. *Antioxid Redox Signal* **37**, 631-646 (2022).
52. T. Natsume *et al.*, A direct nanoflow liquid chromatography-tandem mass spectrometry system for interaction proteomics. *Anal Chem* **74**, 4725-4733 (2002).

Acknowledgments: We thank S. Fujiyama, A. Yokoyama, K. Nishino, A. Abe, F. Yamamoto, N. Kato for technical assistance; T. Mizuno, H. Kusuhara, and members of the Gotoh laboratory for discussion; T. Taniguchi for providing VSV; and T. Taniguchi, J. A. Cooper, and C. Yokoyama for comments on the manuscript. This research was partly supported by the Promotion Project for Young Investigators in Hokkaido University. We also acknowledge the use of ChatGPT-4o (OpenAI) to assist with suggesting improvements to the text for conciseness and clarity.

Funding: This study was supported by grants as follows:

Ministry of Education, Culture, Sports, Science, and Technology of Japan (MEXT) JP16K19149 (T.O.)

MEXT JP18K07168 (T.O.)

MEXT JP21K07064 (T.O.)

MEXT JP24K02172 (T.O.)

MEXT JP24K22007 (T.O.)

MEXT JP15H05773 (Y.G.)

MEXT JP16H06481 (Y.G.)

MEXT JP16H06479 (Y.G.)

MEXT JP16H06279 (Y.G.)

MEXT JP22H00431 (Y.G.)

MEXT JP22H04925(PAGS) (Y.G.)

MEXT JP24H02322 (Y.G.)

MEXT JP18gm0610013 (Y.G.)

MEXT JP24gm1310004 (Y.G.)

MEXT JP24H02299 (H.Y.)

MEXT JP24H02302 (H.Y.)

FOREST program of the Japan Science and Technology Agency JPMJFR204Q (T.O.)

FOREST program of the Japan Science and Technology Agency JPMJFR2150 (H.Y.)

Takano Life Science Research Foundation (T.O.)

Chemo-Sero-Therapeutic Research Institute (T.O.)

Mitsubishi Foundation (T.O.)

Naito Foundation (T.O.)

Secom Foundation (T.O.)

Astellas Foundation for Research on Metabolic Disorders (T.O.)

Nagase Science and Technology Foundation (Y.G.)

Author contributions:

Conceptualization: T.O., Y.G.

Methodology: T.O., T.H., T.N., S-i.I., S.I., H.Ko., M.Y., TK., Ha.K.

Investigation: T.O., K.N., M.O., N.M., Y.O., R.S., S.A., H.Y.

Visualization: T.O., K.N.

Funding acquisition: T.O., H.Y., Y.G.

Project administration: T.O., Y.G.

Supervision: T.O., Y.G.

Writing – original draft: T.O., Y.G.

Writing – review & editing: T.O., K.N., R.S., Y.G.

Competing interests: The authors declare that they have no competing interests.

Data and materials availability: All data needed to evaluate the manuscript are available in the main text or Supplementary Materials. MS raw files and identifications were deposited at the ProteomeXChange JPOST database with the following dataset identifiers: JPST003494 (PXD058403): Proteomic identification of proteins associated with the MAVS carboxylation site. JPST003495 (PXD058405): Proteomic identification of PTMs in MAVS (residues 1–200); this dataset corresponds to Fig. S1. JPST003699 (PXD061814): Proteomic identification of PTMs in MAVS (residues 1–200); this dataset corresponds to Fig. S2.

Supplementary Materials List

Materials and Methods

Figs. S1 to S67
Data S1
References (34 - 52)

Figure Legends.

Fig. 1. MAVS is carboxylated in cells. A, Domain structure of hMAVS. Carboxylation sites (D53, E70, E80, and D83) in the cytoplasmic domain are colored red. CARD, caspase activation and recruitment domain; TM, transmembrane. **B**, His_{10}-Flag-tagged hMAVS was isolated from 293T cells using Co^{2+} resin and analysed by immunoblot using antibodies against Flag and pan-carboxylated glutamate (pan-Gla). **C**, His_{10}-Flag-tagged mMAVS or mMAVS(2EA) was isolated from 293T cells transfected with GGCX or control small interfering RNAs (siRNAs) for 4 days in the presence of 20 μM vitamin K1 (VK1) using Co^{2+} resin and analysed by immunoblot using antibodies against Flag and the Glu^{80}-carboxylated (Gla80) form of mMAVS. The signal intensities for Gla80 relative to Flag were quantified and plotted (normalized to lane 2). Note that E70A/E80A/D83A (3A) mutant of mMAVS expressed in 293T cells was still recognized by pan-Gla antibodies, suggesting that MAVS is carboxylated also at sites other than these residues in the CARD domain (Fig. S3C). **D**, His_{10}-Flag-tagged mMAVS was isolated from 293T cells infected with 0.3 multiplicity of infection (MOI) of VSV for the indicated times in the presence of 20 μM VK1 using Co^{2+} resin and analysed by immunoblot using antibodies against Flag and Gla80. The signal intensities for Gla80 relative to Flag were quantified and plotted (normalized to lane 6). **E**, His_{10}-tagged protein was isolated from liver extracts derived from WT or heterozygous His_{10}-MAVS KI mice using Co^{2+} resin and analysed by immunoblot using antibodies against pan-Gla and mMAVS. The asterisk indicates a nonspecific band. **F,** 293T cells maintained in the presence or absence of VK1 were transiently transfected with expression vectors for Flag-tagged cytoGla and Myc epitope-tagged hMAVS for 20 h, lysed, and analysed by immunoblot using antibodies against pan-Gla, Flag, Myc, and p38 MAPK (loading control). The signal intensities for Pan-Gla relative to Flag were quantified and plotted (normalized to lane 6). **G**, WT or GGCX knockout (KO) 293T cells maintained in the presence of VK1 were transiently transfected with expression vectors for Flag-cytoGla and Myc-hMAVS for 20 h, lysed, and analysed by immunoblot using antibodies against pan-Gla, Flag, Myc, GGCX, and p38 MAPK. The signal intensities for Pan-Gla relative to Flag were quantified and plotted (normalized to lane 4). **H**, 293T cells maintained in the presence of VK1 were transiently transfected with expression vectors for Flag-cytoGla and Myc-hMAVS for 20 h, lysed, and subjected to subcellular fractionation into cytosol (C) and organelle-bound (O) fractions, followed by immunoblot using antibodies against pan-Gla, Flag, Myc, KDEL (endoplasmic reticulum [ER] marker), and glyceraldehyde-3-phosphate dehydrogenase (GAPDH; cytosolic marker). The signal intensities for Pan-Gla relative to Flag were quantified and plotted (normalized to lane 5). **I**, 293T cells maintained in the presence of VK1 were transiently transfected with expression vectors for Flag-cytoGla, Myc-hMAVS (or the corresponding empty vector), and green fluorescent protein (GFP)-tagged RTN4a (ER marker) for 20 h. Cells were fixed and subjected to immunofluorescence staining with antibodies against pan-Gla, Flag, and Myc. The boxed regions in the upper panels of each set are shown at higher magnification in the corresponding lower panels. Data in **B**, **C**-**E**, **H** are representative from three independent experiments, the F is from four independent experiments, and the **D** is from five independent experiments. Individual datapoint show results for independent experiments, the bars show means ± standard error of the mean (SEM). Data in **I**, representative images (scale bars = 50 μm) are shown together with a violin plot for the relative Pan-Gla/Flag fluorescence intensity ratio determined for the indicated numbers of cells from pooled together from three independent experiments (three fields per experiment). Statistical analyses in (D) were performed using Dunnett's multiple comparison test (****$P < 0.001$), in (C,F,G,H) were performed using one sample *t* test (*$P < 0.05$, **$P < 0.01$, ***$P < 0.005$), and in (I) were performed using unpaired two-tailed Mann-Whitney *U* test (****$P < 0.0001$).

Fig. 2. Topology inversion of GGCX. A, Schematic model for the membrane topology inversion of GGCX from type II to type III, where in the type II orientation, the N-terminus is positioned in the cytoplasm and the C-terminus in the ER lumen, while in the type III orientation, the N-terminus is localized to the ER lumen and the C-terminus to the cytoplasm, and its effect on N-linked glycosylation. **B**, 293T cells maintained in the presence of VK1 were transiently transfected with expression vectors for Myc-mGGCX and Flag-hMAVS for 20 h, lysed, and subjected to EndoH treatment for 5 h followed by immunoblot using antibodies against Myc, Flag, and p38 MAPK, or to lectin blot analysis with horseradish peroxidase-conjugated *Canavalia ensiformis* lectin (ConA). Note that two bands of GGCX, corresponding to apparent high molecular weight (A) and low molecular weight (B) forms, were detected in the presence of MAVS overexpression. The signal intensities for GGCX (B) relative to GGCX (A) (normalized to lane 2) and ConA relative to Myc were quantified and plotted (normalized to GGCX (A) in lane 2). **C**, Schematic model of the split mNG2 reporter system for monitoring the membrane topology of GGCX. **D**, 293T cells were transfected with expression vectors for Flag-hMAVS, Myc-tagged $mNG2_{11}$-mGGCX, and hemagglutinin epitope (HA)-tagged $mNG2_{1–10}$-KDEL for 20 h. Cells were fixed and subjected to immunofluorescence staining with antibodies against Flag, Myc, and HA. Data in **B** is representative from three independent experiments, shown as individual points, and the bars show means ± standard error of the mean (SEM). In **D**, representative images (scale bars = 20 μm) are shown together with a violin plot for the relative mNG2/Myc fluorescence intensity ratio determined for the indicated numbers of cells pooled together from three independent experiments. Statistical analyses in (B) were performed using one sample *t* test (***P* < 0.01, ****P* < 0.005), and in (D) were performed using Kruskal-Wallis test followed by Dunn's multiple comparison test (*****P* < 0.0001).

Fig. 3. GGCX-mediated carboxylation of MAVS promotes IFN production and inhibits caspase activation. A, 293T cells were transfected for 24 h with expression plasmids for WT or the indicated mutant forms of hMAVS (100 or 500 ng), a reporter plasmid encoding *Renilla* luciferase (Luc) under the control of the mouse interferon β1 (*Ifnb1*) promoter, and the pGL3-control vector encoding firefly Luc as an internal control. Cells were lysed for measurement of Luc activity, and activity of *Renilla* Luc was normalized against that of firefly Luc. **B**, 293T cells transiently transfected for 20 h with expression plasmids for Myc-tagged WT or mutant forms of hMAVS were lysed and analysed by immunoblot using antibodies against Myc, phosphorylated IRF3 (p-IRF3), IRF-3, Poly (ADP-ribose) polymerase (PARP), p38 mitogen-activated protein kinase (MAPK), and GAPDH. **C**, **D**, MEFs isolated from MAVS KO mice were infected with retroviruses encoding either WT or 3A (D53A, E70A, and E80A) mutant forms of mMAVS, transfected with 0.25 μg/ml poly(I:C) for the indicated times (**C**) or infected with VSV for 12 h (**D**), and assayed for *Ifnb1* mRNA by reverse transcription and quantitative PCR (RT-qPCR). **E**, MAVS KO MEFs expressing WT or 3A mutant forms of mMAVS were infected for 24 h with VSV at an MOI of 0.3, washed, and incubated for 24 h in fresh medium, which was then collected for assay of VSV titer measuring plaque-forming units (PFU) by standard plaque assay. **F**, **G**, HeLa S3 cells were transfected first with GGCX or control siRNAs for 4 days, then with poly(I:C) at 2.5 μg/ml (**F**) or 0.25 or 2.5 μg/ml (**G**) for 6 h. They were then subjected to RT-qPCR analysis of *IFNB1* mRNA (**F**) or to immunoblot using antibodies against p-IRF3, IRF-3, PARP, GGCX, p38, and GAPDH (**G**). The signal intensities for p-IRF3 relative to IRF-3 and cleaved PARP

relative to full-length were quantified and plotted (normalized to lane 3). **H**, **I**, 293T cells were transfected for 20 h with expression vectors for Myc-mGGCX and Flag-hMAVS (or Flag-mTBK1) then subjected to RT-qPCR analysis of *IFNB1* mRNA (**H**) or to immunoblot using antibodies against cleaved caspase-3, Flag, Myc, and p38 MAPK (**I**). The signal intensities for cleaved caspase-3 relative to p38 were quantified and plotted (normalized to lane 3 for MAVS, and to lane 5 for TBK1, respectively). Data in **A**, **C**, and **D** are means ± standard deviation (SD) of triplicates from an experiment repeated three times with similar results. Data in **B**, **G** are representative from three independent experiments, in **I** is representative from six independent experiments, in **F** is from three independent experiments, in **H** is from six independent experiments, in **E** is from nine independent experiments. The bars show means ± standard error of the mean (SEM). Statistical analyses in (C,D,E,F,H) were performed using unpaired Student's *t* test (***P* < 0.01, ****P* < 0.005, *****P* < 0.001), and in (G,I) were performed using one sample *t* test (**P* < 0.05, ***P* < 0.01, not significant (NS)).

Fig. 4. Proteomic identification of MAVS carboxylation site-associated proteins. A, Volcano plot obtained from immunoprecipitation-mass spectrometry (IP-MS) analysis of WT versus 4A mutant forms of hMAVS in 293T cells. Red points indicate mitochondria-localized proteins and known MAVS interactors with fold change (FC) > 2 and *P* < 0.05. Polo-like kinase 1 (PLK1) and translocase of outer mitochondrial membrane 40 (TOMM40) are differentially associated proteins of WT and 4A mutant forms of hMAVS in 293T cells. **B**, 293T cells transiently transfected for 20 h with expression vectors for Flag-tagged WT or 4A mutant forms of hMAVS were subjected to IP with antibodies against Flag, and the resulting precipitates and original cell lysates (Total) were analysed by immunoblot using antibodies against TOMM40, PLK1, Flag, and GAPDH. The signal intensities for coIPed TOMM40 and PLK1 relative to total were quantified and plotted (normalized to lane 6). **C**,**D**, 293T cells transiently transfected with expression vectors for Myc-hTOMM40 and Flag-hMAVS for 20 h were either analysed by immunoblot using antibodies against p-IRF3, IRF-3, PARP, Flag, Myc, and GAPDH (**C**) or assayed for *IFNB1* and *MAVS* mRNAs by RT-qPCR (**D**). The signal intensities for p-IRF3 relative to IRF-3 (normalized to lane 2) and cleaved PARP relative to full-length were quantified and plotted (normalized to lane 4). **E**, **F**, HeLa S3 cells were transiently transfected first with expression vectors for TOMM40 or GFP (control) short hairpin RNAs (shRNAs) for 4 days, then with an expression vector for Flag-hMAVS for 20 h. Cell lysates were then either analysed by immunoblot using antibodies against cleaved PARP, p-IRF3, Flag, TOMM40, and p38 MAPK (**E**) or assayed for *IFNB1* and *MAVS* mRNAs by RT-qPCR (**F**). The signal intensities for cleaved PARP relative to p38 were quantified and plotted (normalized to lane 2). Data in **B**, **C**, **E** are representative from three independent experiments, in **D** is from three independent experiments, in **F** is from four independent experiments. Individual data points show data from independent experiments, the bars show means ± standard error of the mean (SEM). Statistical analyses in (D,F) were performed using unpaired Student's *t* test (***P* < 0.01, not significant (NS)), and in (B,C,E) were performed using one sample *t* test (**P* < 0.05, ***P* < 0.01).

Fig. 5. VK-dependent GGCX activity protects against viral infection *in vivo*. A–C, Age- and sex-matched mice with neural cell lineage-specific ablation of GGCX (*Nes-Cre;Ggcx*$^{fl/fl}$ mice) and control (*Ggcx*$^{fl/fl}$) mice were infected intranasally with VSV (1×10^7 PFU) (**A**) and monitored daily for survival for 14 days (**B**). The viral titer in the brain (PFU per gram wet weight) was also determined by standard plaque assay at 1 day after VSV infection (5×10^6 PFU) (**C**). **D**, RT-qPCR

analysis of *Ifna1*, *Ifnb1*, and *Actb* mRNAs in the brain of *Nes-Cre;Ggcx*$^{fl/fl}$ and *Ggcx*$^{fl/fl}$ mice at 1 day after VSV infection (5×10^6 PFU). Results for three control mice and GGCX-deficient mice not infected with VSV are also shown. **E**, Olfactory bulbs of mice at 3 days after VSV infection were analysed by immunoblot using antibodies against cleaved caspase-3, GGCX, and p38 MAPK. A representative blot with each lane corresponding to one mouse as well as quantitative data for the band intensity are shown. Note that the incomplete reduction of GGCX levels in Nestin-Cre knockout mice is likely due to the remaining expression of GGCX in Nestin-negative cell populations. **F–H**, Age- and sex-matched WT mice were treated with warfarin (0.96 mg/l) or vehicle (ethanol) in drinking water for 4 weeks, then infected intranasally with VSV (1×10^7 PFU) (**F**). Mice were monitored daily for survival for 14 days (**G**). The viral titer in the brain was also determined at 1 day after VSV infection (5×10^6 PFU) (**H**). Data in **B** are shown for the indicated numbers of animals pooled together from five independent experiments, in **C** are for 36 *Nes-Cre;Ggcx*$^{fl/fl}$ and 35 *Ggcx*$^{fl/fl}$ mice from eight independent experiments, in **D** are for 8 and 15 mice, respectively, from three independent experiments. Data in **E** are shown for 8 and 12 mice for caspase-3, 3 and 3 mice for GGCX quantification, respectively, from three independent experiments. Data in **G** are shown for the indicated numbers of animals pooled together from two independent experiments, in **H** are for 13 mice per group from three independent experiments. Individual data points represent data from a single animal, and bars in (C,D,H) indicate means, and the bars in (E) show means ± standard error of the mean (SEM). Statistical analyses in (C,D,E,H) were performed using unpaired Student's *t* test (*$P < 0.05$, **$P < 0.01$), and in (B,G) were performed using log-rank test (*$P < 0.05$).

Fig. 1

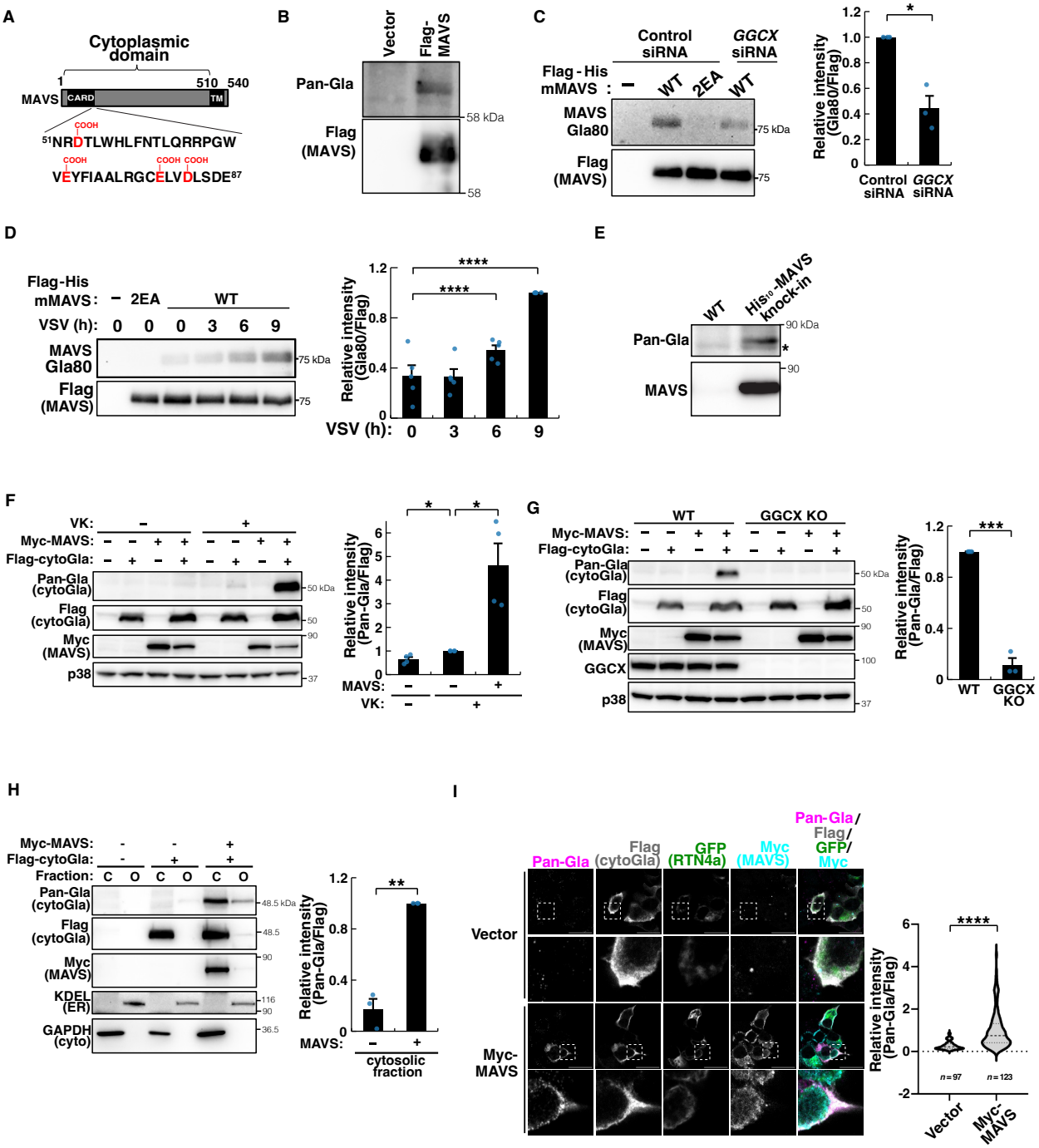
A
Cytoplasmic domain
MAVS
CARD
TM
1
510
540
51NRDTLWHLFNTLQRRPGW
VEYFIAALRGCELVDLSDE87
B
Vector
Flag-MAVS
Pan-Gla
Flag (MAVS)
58 kDa
C
Control siRNA
GGCX siRNA
Flag-His mMAVS :
WT
2EA
MAVS Gla80
Flag (MAVS)
75 kDa
Relative intensity (Gla80/Flag)
D
Flag-His mMAVS:
2EA
WT
VSV (h):
MAVS Gla80
Flag (MAVS)
Relative intensity (Gla80/Flag)
E
WT
His10-MAVS knock-in
Pan-Gla
MAVS
90 kDa
F
VK:
Myc-MAVS:
Flag-cytoGla:
Pan-Gla (cytoGla)
Flag (cytoGla)
Myc (MAVS)
p38
50 kDa
Relative intensity (Pan-Gla/Flag)
MAVS:
G
WT
GGCX KO
Myc-MAVS:
Flag-cytoGla:
Pan-Gla (cytoGla)
Flag (cytoGla)
Myc (MAVS)
GGCX
p38
Relative intensity (Pan-Gla/Flag)
H
Myc-MAVS:
Flag-cytoGla:
Fraction:
C
O
Pan-Gla (cytoGla)
Flag (cytoGla)
Myc (MAVS)
KDEL (ER)
GAPDH (cyto)
48.5 kDa
Relative intensity (Pan-Gla/Flag)
MAVS:
cytosolic fraction
I
Pan-Gla
Flag (cytoGla)
GFP (RTN4a)
Myc (MAVS)
Pan-Gla / Flag / GFP / Myc
Vector
Myc-MAVS
Relative intensity (Pan-Gla/Flag)
n=97
n=123
Vector
Myc-MAVS

Fig.2.

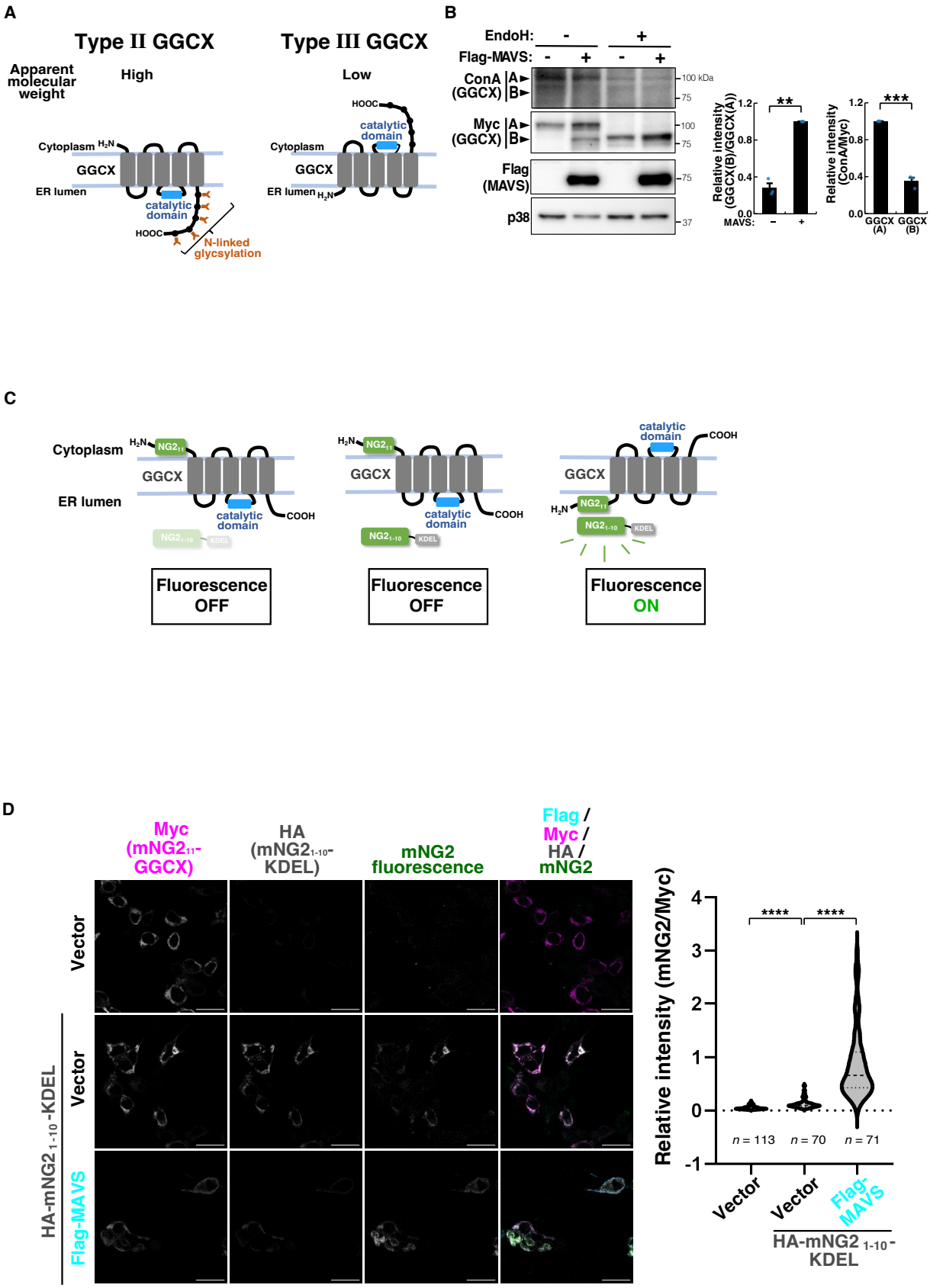
A
Type II GGCX
Type III GGCX
Apparent molecular weight
High
Low
Cytoplasm
GGCX
ER lumen
catalytic domain
N-linked glycsylation
B
EndoH:
Flag-MAVS:
ConA (GGCX)
Myc (GGCX)
Flag (MAVS)
p38
100 kDa
Relative intensity (GGCX(B)/GGCX(A))
Relative intensity (ConA/Myc)
MAVS:
GGCX (A)
GGCX (B)
C
Fluorescence OFF
Fluorescence OFF
Fluorescence ON
D
Myc (mNG2$_{11}$-GGCX)
HA (mNG2$_{1-10}$-KDEL)
mNG2 fluorescence
Flag / Myc / HA / mNG2
Vector
Flag-MAVS
HA-mNG2$_{1-10}$-KDEL
Relative intensity (mNG2/Myc)
n = 113
n = 70
n = 71
Vector
Vector
Flag-MAVS
HA-mNG2$_{1-10}$-KDEL

Fig.3.

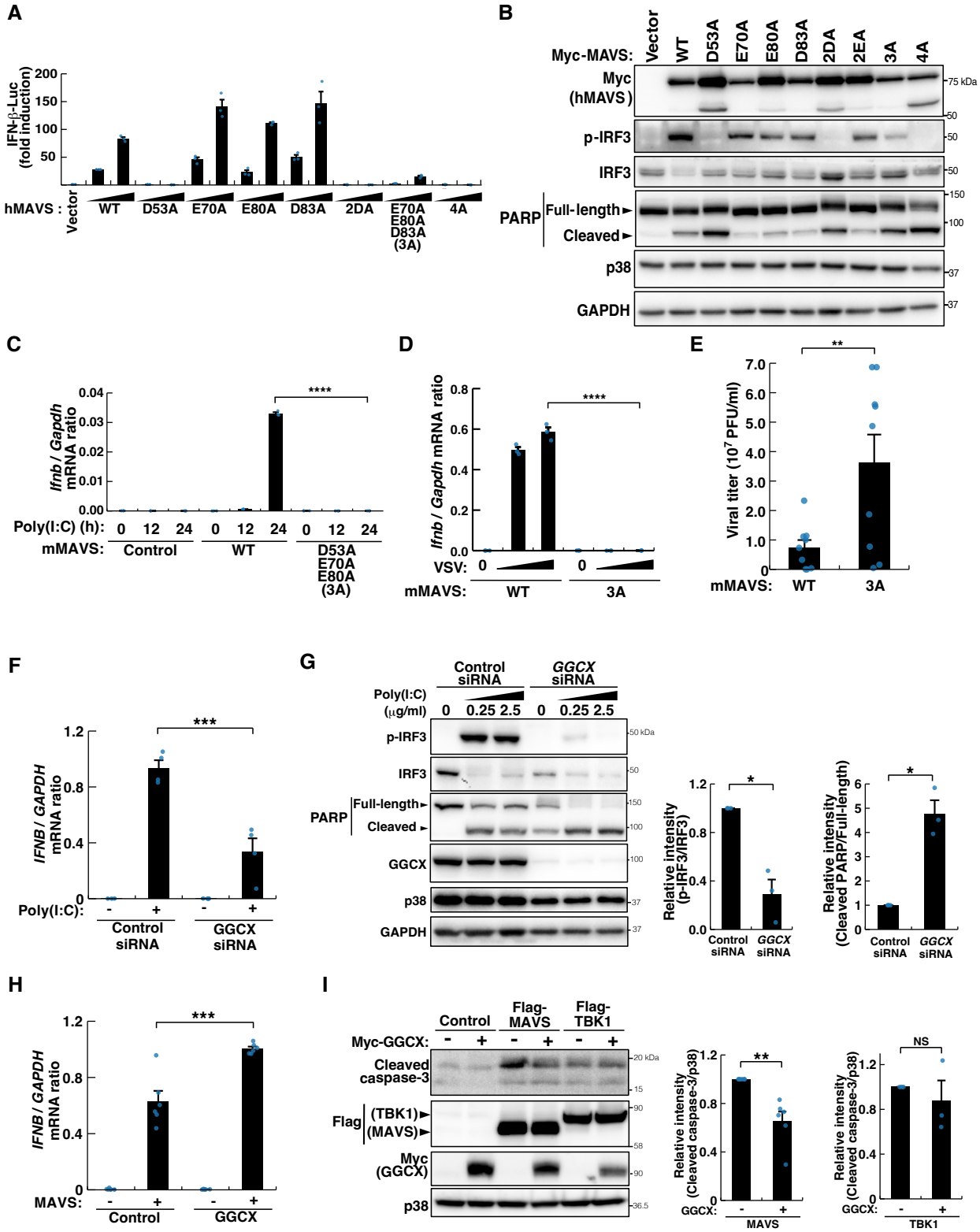
A
IFN-β-Luc (fold induction)
hMAVS : Vector WT D53A E70A E80A D83A 2DA E70A E80A D83A (3A) 4A
B
Myc-MAVS: Vector WT D53A E70A E80A D83A 2DA 2EA 3A 4A
Myc (hMAVS)
p-IRF3
IRF3
PARP Full-length Cleaved
p38
GAPDH
75 kDa
C
Ifnb / Gapdh mRNA ratio
Poly(I:C) (h): 0 12 24 0 12 24 0 12 24
mMAVS: Control WT D53A E70A E80A (3A)
D
Ifnb / Gapdh mRNA ratio
VSV: 0 0
mMAVS: WT 3A
E
Viral titer (10^7 PFU/ml)
mMAVS: WT 3A
F
IFNB / GAPDH mRNA ratio
Poly(I:C): - + - +
Control siRNA
GGCX siRNA
G
Control siRNA
GGCX siRNA
Poly(I:C) (μg/ml) 0 0.25 2.5 0 0.25 2.5
p-IRF3
IRF3
PARP Full-length Cleaved
GGCX
p38
GAPDH
Relative intensity (p-IRF3/IRF3)
Relative intensity (Cleaved PARP/Full-length)
H
IFNB / GAPDH mRNA ratio
MAVS: - + - +
Control
GGCX
I
Control
Flag-MAVS
Flag-TBK1
Myc-GGCX: - + - + - +
Cleaved caspase-3
Flag (TBK1) (MAVS)
Myc (GGCX)
p38
Relative intensity (Cleaved caspase-3/p38)
GGCX: - + MAVS
GGCX: - + TBK1
NS

Fig. 4.

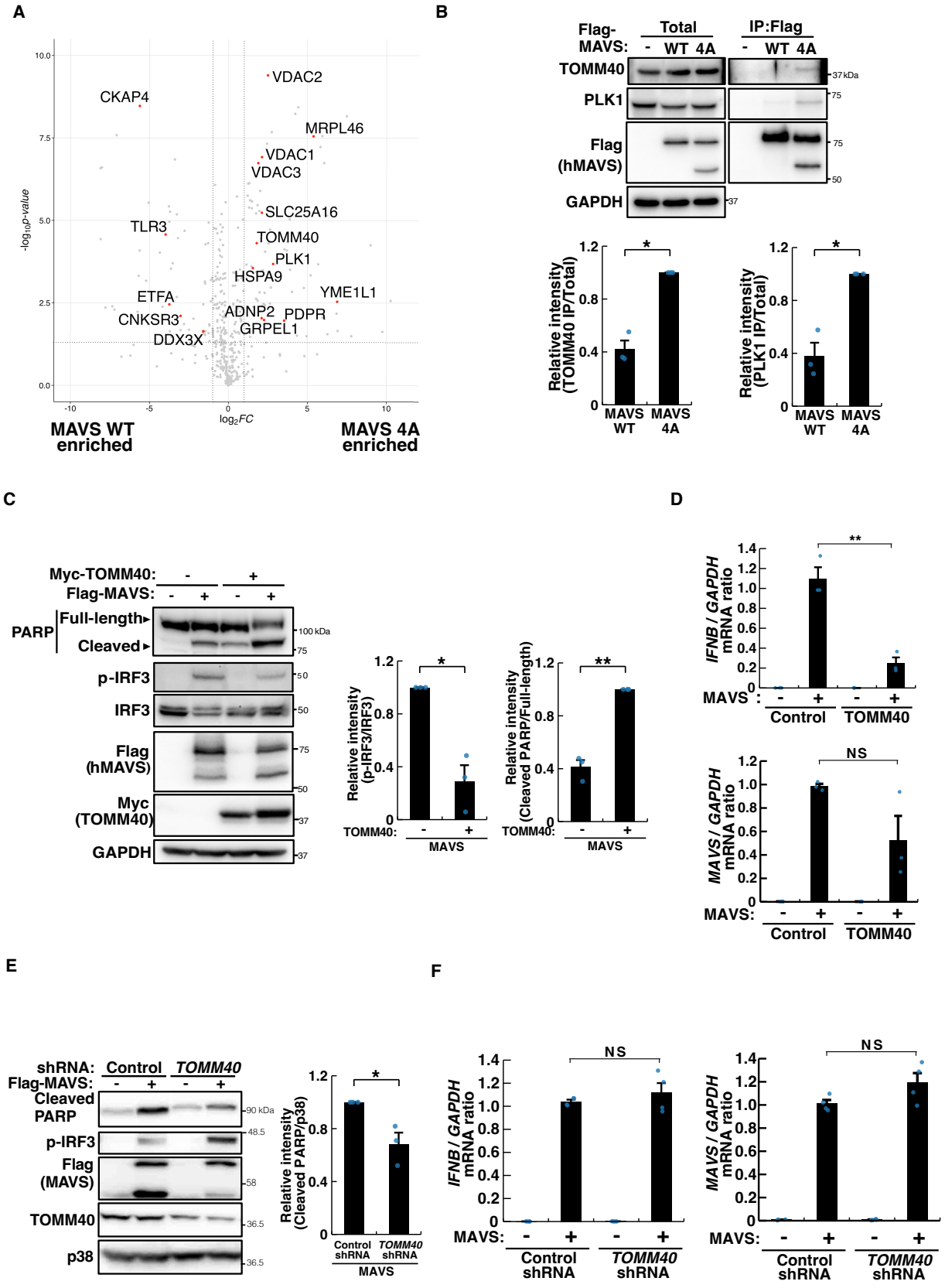
A
VDAC2
CKAP4
MRPL46
VDAC1
VDAC3
SLC25A16
TLR3
TOMM40
PLK1
HSPA9
YME1L1
ETFA
ADNP2
PDPR
CNKSR3
GRPEL1
DDX3X
-log10P-value
log2FC
MAVS WT enriched
MAVS 4A enriched
B
Flag-MAVS:
Total
IP:Flag
- WT 4A
- WT 4A
TOMM40
PLK1
Flag (hMAVS)
GAPDH
37 kDa
75
75
50
37
Relative intensity (TOMM40 IP/Total)
Relative intensity (PLK1 IP/Total)
MAVS WT
MAVS 4A
C
Myc-TOMM40:
Flag-MAVS:
PARP
Full-length
Cleaved
p-IRF3
IRF3
Flag (hMAVS)
Myc (TOMM40)
GAPDH
100 kDa
Relative intensity (p-IRF3/IRF3)
Relative intensity (Cleaved PARP/Full-length)
TOMM40:
MAVS
D
IFNB / GAPDH mRNA ratio
MAVS / GAPDH mRNA ratio
MAVS:
Control
TOMM40
NS
E
shRNA:
Control
TOMM40
Flag-MAVS:
Cleaved PARP
p-IRF3
Flag (MAVS)
TOMM40
p38
90 kDa
48.5
58
36.5
36.5
Relative intensity (Cleaved PARP/p38)
Control shRNA
TOMM40 shRNA
MAVS
F
IFNB / GAPDH mRNA ratio
MAVS / GAPDH mRNA ratio
MAVS:
Control shRNA
TOMM40 shRNA
NS

Fig.5.

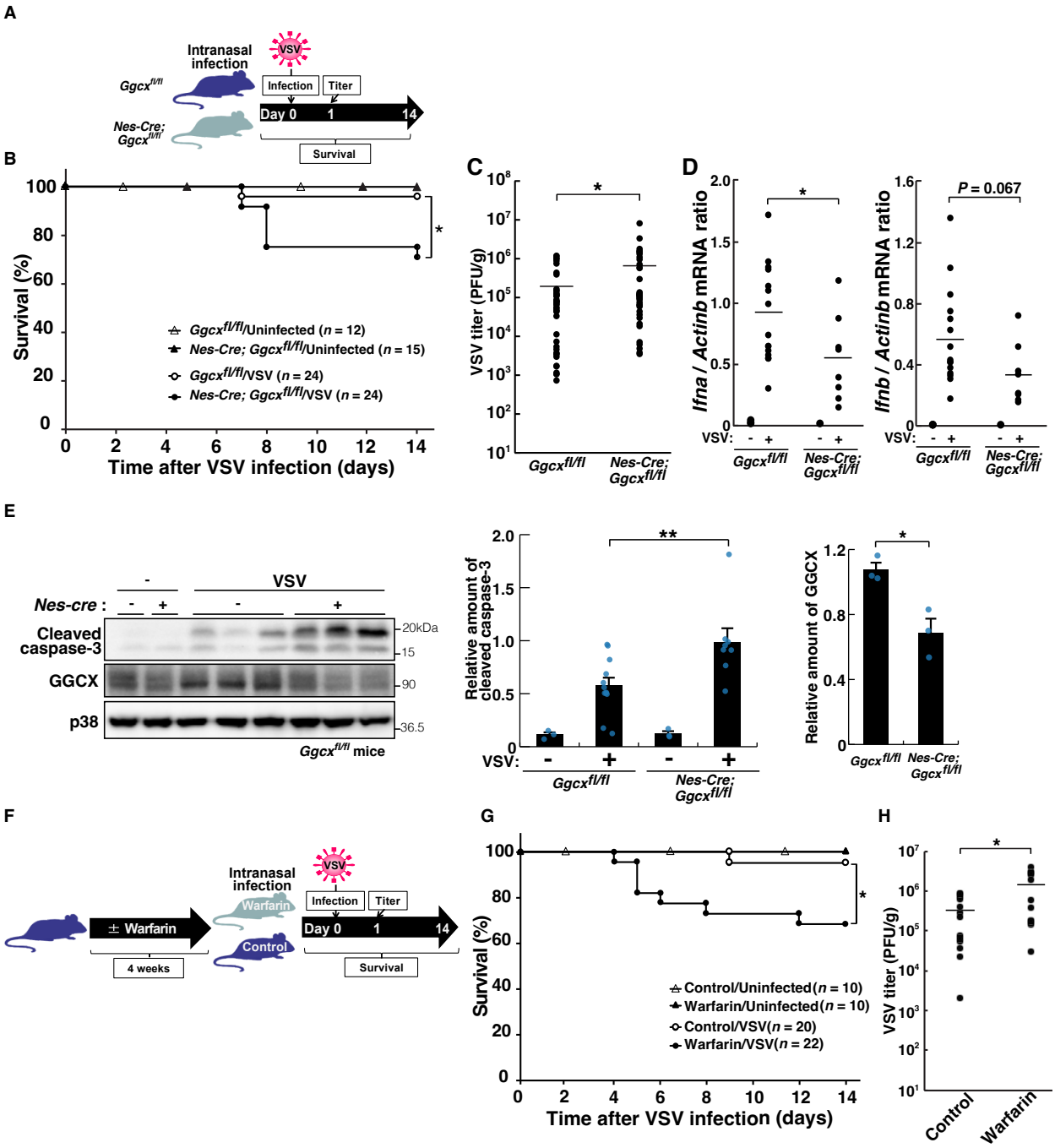
A
Intranasal infection
VSV
Infection
Titer
Day 0
1
14
Survival
Ggcx fl/fl
Nes-Cre; Ggcx fl/fl
B
Survival (%)
Time after VSV infection (days)
Ggcx fl/fl/Uninfected (n = 12)
Nes-Cre; Ggcx fl/fl/Uninfected (n = 15)
Ggcx fl/fl/VSV (n = 24)
Nes-Cre; Ggcx fl/fl/VSV (n = 24)
C
VSV titer (PFU/g)
D
Ifna / Actinb mRNA ratio
Ifnb / Actinb mRNA ratio
P = 0.067
VSV:
E
Nes-cre :
Cleaved caspase-3
GGCX
p38
20kDa
15
90
36.5
Ggcx fl/fl mice
Relative amount of cleaved caspase-3
Relative amount of GGCX
F
± Warfarin
4 weeks
Warfarin
Control
G
Control/Uninfected (n = 10)
Warfarin/Uninfected (n = 10)
Control/VSV (n = 20)
Warfarin/VSV (n = 22)
H
Control
Warfarin

5

Science
AAAS

Supplementary Materials for

Membrane topology inversion of GGCX mediates cytoplasmic carboxylation for antiviral defense

Tomohiko Okazaki*, Keiji Nozaki, Nao Morimoto, Yuta Otobe, Riho Saito, Shuntaro Abe, Miyuki Okajima, Hikari Yoshitane, Tomohisa Hatta, Shun-ichiro Iemura, Tohru Natsume, Hidetaka Kosako, Miwako Yamasaki, Satoshi Inoue, Takashi Kondo, Haruhiko Koseki & Yukiko Gotoh

Corresponding author: okazaki@igm.hokudai.ac.jp

The PDF file includes:

Materials and Methods
Figs. S1 to S67
References (34 - 52)

Other Supplementary Material for this manuscript includes the following:

Table S1
MDAR Reproducibility Checklist

Materials and Methods

Plasmids and reagents

The pEF BOS plasmids encoding Flag-hMAVS, Flag-hRIG-I N, and Flag-hMDA5-N were provided by T. Fujita (Kyoto University). The plasmid pAcGFP1-N1 encoding RTN4a was provided by Y. Okada (University of Tokyo). The mTBK1 cDNA was provided by T. Taniguchi (Institute of Industrial Science, University of Tokyo). The full-length mNG2(11)1−10 cDNA was provided by B. Huang (RRID: Addgene_82610) and was subcloned into pcDNA3-NES-Flag or into pCS4-HA together with the coding sequences for the ER retention signal KDEL and the signal peptide derived from human heat shock protein family A member 5 (HSPA5) (*34*). The full-length hMAVS cDNA was subcloned into the *Bgl*II site of pCS4-Myc and the *Bam*HI site of pcDNA3-His_{10}-Flag. The full-length mMAVS cDNA was provided by T. Kubota (National Institute of Infectious Diseases, Japan) and subcloned into the *Bam*HI site of pcDNA3-His_{10}-Flag and the pMXs-IG vector provided by T. Kitamura (Institute of Medical Sciences, University of Tokyo). The full-length mGGCX and hTOMM40 cDNAs were subcloned into the *Bgl*II site of pCS4-Myc and pCS4-Myc-$mNG2_{11}$. The cDNA for the conserved recognition sequence (CRS) and Gla domains of mGAS6 (5'-CTGTTGCGGGCGCGTGAGGCGGCGCAGTTTCTGCGGCCCAGGCAGCGCCGCGCCTACCAAGTCTTCGAGGAGGCCAAGCAGGGCCACCTGGAACGGGAGTGCGTGGAGGAGGTGTGCAGCAAAGAGGAGGCCAGAGAGGTGTTCGAGAACGACCCCGAGACGGAGTATTTCTATCCACGATATCAAGAG-3') (*35*), as well as the nuclear export signal (NES) sequence of MAP2K1 (5'-GCTCTTCAAAAGAAGCTCGAAGAACTTGAGCTTGATGAA-3')(*36*) were subcloned into the *Bam*H1 and *Eco*R1 sites of pcDNA3. The p38-AGF cDNA was subcloned into the BamHI site of pcDNA3. Mutants of hMAVS and mMAVS were constructed using a QuikChange site-directed mutagenesis kit (Agilent). A reporter gene construct harboring the *Renilla* luciferase sequence downstream of the murine *Ifnb1* promoter (p125-RLuc) was generated from p125-Luc (*37*) provided by T. Fujita. Poly(I:C) was obtained from GE Healthcare. Diet lacking VK was from Oriental Yeast. The antibiotic cefotiam hydrochloride (pansporin T) was from Takeda. Warfarin, VK1, and staurosporine were from Sigma-Aldrich. Anisomycin was from Merck Millipore. Con A-HRP was from EY Laboratories. Endo H was from New England BioLabs. Cycloheximide was from Wako.

RNA interference

Short hairpin RNA (shRNA) vectors were constructed and introduced into cells by transfection as described previously (*38*). The targeting sequences were 5'-GGGTGCTCAGGTAGTGGTT-3' for GFP (control) and 5'-GCAAGAACAAGTTTCAGTA-3' for hTOMM40. A Stealth RNA interference (RNAi) system (Thermo Fisher Scientific) was employed for depletion of GGCX in HeLa S3 cells. The cells were transfected with siRNA oligonucleotides for 4 days using Lipofectamine RNAiMAX reagent (Thermo Fisher Scientific). The GGCX siRNA sequences for 293T were 5'-AUUUCCUGUAACUUGGCCCUCCAGG-3' and 5'-CCUGGAGGGCCAAGUUACAGGAAAU-3', and for HeLa S3 they were 5'-UUUGAAGGGACUGAAGAGCCAGUGC-3' and 5'-GCACUGGCUCUUCAGUCCCUUCAAA-3'. The Med GC #1 siRNA served as a negative control.

RT-qPCR

Total RNA was isolated from cells and mouse brain using RNAiso Plus reagent (Takara), and portions of the RNA (1 μg) were subjected to reverse transcription (RT) with ReverTra Ace qPCR RT Master Mix and gDNA Remover (Toyobo). The resulting cDNA was subjected to quantitative PCR (qPCR) analysis using a KAPA SYBR Fast qPCR Kit (Kapa Biosystems) and a LightCycler instrument (Roche). The abundance of target mRNAs was normalized against glyceraldehyde-3-phosphate dehydrogenase (GAPDH) mRNA or β-actin mRNA, and gene expression levels were quantified using the standard curve method. The abundance of spliced X-box binding protein 1 (sXBP1) mRNA was normalized against total XBP1 mRNA. Sense and antisense primers, respectively, were as follows: mouse *Gapdh*, 5'-TGGGTGTGAACCACGAG-3' and 5'-AAGTTGTCATGGATGACCTT-3'; mouse *Actb*, 5'-AATAGTCATTCCAAGTATCCATGAAA-3' and 5'-GCGACCATCCTCCTCTTAG-3'; mouse *Ifna1*, 5'-CCTGTGTGATGCAGGAACC-3' and 5'-TCACCTCCCAGGCACAGA-3'; mouse *Ifnb1*, 5'-TCCACCAGCAGACAGTGTT-3' and 5'-CTTTGCACCCTCCAGTAATAGC-3'; human *GAPDH*, 5'-ACTCCTCCACCTTTGACGCT-3' and 5'-TCCTCTTGTGCTCTTGCTGG-3'; human *IFNB1*, 5'-CTGGCTGGAATGAGACTATTGTT-3' and 5'-CTTCAGTTTCGGAGGTAACCTG-3'; human *OAS1*, 5'-CCATGCCATTGACATCATCT-3' and 5'- CCTGAGGAGCCACCCTTTA-3'; human *MAVS*, 5'-AACACAGTGGCCCTGAAA-3' and 5'-CTGGATTGGTGAGCGCATTA-3'; human s*XBP1*, 5'-TGCTGAGTCCGCAGCAGGTG-3' and 5'-GCTGGCAGGCTCTGGGGAAG-3'; human total *XBP1*, 5'-AAACAGAGTAGCTCAGACTGC-3' and 5'-TCCTTCTGGGTAGACCTCTGGGAG-3'; human *BiP*, 5'-ACTCCTGCGTCGGCGTGTTC-3' and 5'-GGCGACATAGGACGGCGTGA-3'.

Viral infection

Cells were infected with VSV as described previously (*17*). Mice were infected with VSV via the intranasal route as described previously (*39*).

Mice

Mice homozygous for a floxed allele of *Ggcx* (*Ggcx*$^{fl/fl}$ mice) were described previously (*7*). MAVS knockout (KO; *Mavs*$^{-/-}$) mice (*40*) were obtained from S. Akira and T. Kawai (Osaka University), *Nes-Cre* mice (*41*) were from R. Kageyama (Kyoto University), and *Lyz2-Cre* mice were from The Jackson Laboratory. C57BL/6J mice were used for all experiments unless otherwise noted. Both male and female mice (6–12 weeks old) were used. Euthanasia was performed through isoflurane overdose followed by cervical dislocation. All mice were maintained and handled according to protocols approved by the Animal Care and Use Committee of the University of Tokyo and Hokkaido University.

Generation of His_{10}-MAVS knock-in (KI) mice

The His_{10}-MAVS KI mouse line was generated using CRISPR technology. Both crRNA and tracrRNA (1072534) were obtained from Integrated DNA Technologies (IDT), mixed at a concentration of 200 μM each, annealed at 95°C, then cooled to room temperature. The RNA complex (1.2 μl) was mixed with 1.7 μl of Cas9 protein (1081059; IDT) at 10 mg/ml and 2.1 μl of phosphate-buffered saline (PBS), then incubated for 10 min at room temperature. Next, ssODN (Eurofins) was added at a final concentration of 400 μg/ml, and the mixture was diluted with Opti-MEM I (Thermo Fisher Scientific) to a volume of 75 μl. C57BL/6N fertilized mouse eggs were aligned (length 1 cm) with a 1 mm gap in the presence of 5 μl of RNA-protein mixture

for electroporation (GEB15; BEX) at 30 V for five cycles of 3 ms on and 97 ms off (*42*). Embryos were cultured overnight in M16 medium at 37°C until the two-cell stage, then transferred to the oviducts of ICR pseudopregnant dams. The ssODN and crRNA sequences were as follows: targeting ssODN (mm10 chr2:131,238,732–131,238,793 + His_{10} + mm10 chr2:131,238,797–131,238,861), CCAGTCCATCTCAGTCCATCCCACCCTGCCAGGGTCCGAGTCACTCCAGAAGCTGAG CAGCCATGCATCATCATCATCATCATCATCATCATACATTTGCTGAGGACAAGA CCTATAAGTATATCCGAGACAACCACAGCAAGTTTTGCTGTGTTGA (with the His_{10} coding sequence underlined); wild-type (WT) corresponding ssODN (mm10 chr2:131,238,732–131,238,861), CCAGTCCATCTCAGTCCATCCCACCCTGCCAGGGTCCGAGTCACTCCAGAAGCTGAG CAGCCATGACATTTGCTGAGGACAAGACCTATAAGTATATCCGAGACAACCACAGC AAGTTTTGCTGTGTTGA; crRNA Ips1_type_s1, 5'-GCCAAGATTCTAGAAGCTGAGAAAG-3'; crRNA Ips1_type_r1, 5'-CTCACCTGGTCACTAGCTGTG-3'. Oligonucleotide primers 5'-CCGAGTCACTCCAGAAGCTGAGCAGCCATG-3' and 5'-CTCGCTCACCTGGTCACTAGCTG-3' were used for genotyping by PCR, and yielded PCR products of 153 bp for the WT allele and 183 bp for the His_{10} KI allele.

Generation of MAVS 3A KI mice

The 3MV mouse line was established by two steps of CRISPR mutant generation using the same procedure as that employed for the His_{10}-MAVS KI mouse line. The heterozygote mice generated by the first step electroporation with crMAVS_1 (AGAGTCCCCAGAGTGTGTCCCGG) and donorMAVS_1 (GGCCACCTGGCCTAAGGAGGCTGTCTGTGCTGTCTTCCAGGATCGACTGCGGGCTTC CTACAGGCAGATCGGGAACCGGGCCACGCTCTGGGGACTCTTCAATAATCTCCAGC GCCGGCCTGGTTGGGTAGCGGTGTTTATAAGAGCTCTCCAAATTTGCGCGCT) were used as recipient for the second step egg electroporation with crMAVS_2 (ATGAAGACCTCCACCCAGCCAGG) and donorMAVS_2 (GACTGCGGGCTTCCTACAGGCAGATCGGGAACCGGGCCACGCTCTGGGGACTCTTC AATAATCTCCAGCGCCGGCCTGGTTGGGTAGCGGTGTTTATAAGAGCTCTCCAAATT TGCGCGCTGCCTGGGCTGGCTGATCAAGTGACTCGAGTTTATCAGAGCTACCTGCCT CCGGGTGAGCATCCTGCCCTAGCCTTTTTC). Oligonucleotide primers 5'-GTACTTGGGCTACCATCGTGG -3' and 5'- AAGGCAGAAGGTCCAAGGGTG -3' were used for genotyping by PCR. We found that 3A MAVS knock-in (KI) mice were more susceptible to infection than control (WT) mice. However, since MAVS 3A KI mice somehow reduced the expression level of this mutant MAVS, we were unable to precisely assess the in vivo role of these carboxylation sites (Fig. S25A-C).

Generation of GGCX KO cells

GGCX KO 293T and N2a cells were generated as previously described (*43*). For construction of the CRISPR vector for human *GGCX* or mouse *Ggcx* deletion, pairs of oligonucleotides encoding the guide RNA (gRNA) were designed, annealed, and ligated into the px458 vector (*44*). The sequences used were as follows: human *GGCX*, 5'-CACCGAGAGCAATGGCGGTGTCTGC-3' and 5'-AAACGCAGACACCGCCATTGCTCTC-

3'; mouse *Ggcx*, 5'-CACCGTGTGCACCGCGGCTCCGCAC-3' and 5'-AAACGTGCGGAGCCGCGGTGCACAC-3'.

Tail bleeding assay

The mouse tail bleeding assay was performed as previously described (*45*).

Antibodies

Antibodies against Myc (9E10, sc-40), hemagglutinin (HA) epitope (Y11, sc-805), TOMM40 (H300, sc-11414 or D-2, sc-365467), MAVS (C-1, sc-365333), to IRF-3 (SL-12, sc-33641), and p38 mitogen-activated protein kinase (MAPK) (C-20, sc-535) were obtained from Santa Cruz Biotechnology. Antibodies against PARP (#9542), cleaved PARP (human-specific) (#9541), cleaved caspase-3 (5A1E, #9664), phospho-IRF3 (#4947), and MAVS (rodent-specific) (#4983) were from Cell Signaling Technology. Antibodies against Flag (M2, F3165) were from Sigma-Aldrich. Antibodies against MAVS (ab25084) and PLK1 were from Abcam. Antibodies against GGCX (16209-1-AP) were from Proteintech. Antibodies against KDEL (10C3, ADI-SPA-827-F) were from Enzo Life Sciences. Antibodies against GAPDH (MAB374) were from Merck Millipore. Antibodies against HA(3F10, 11867423001) were from Roche. Antibodies against pan-Gla (M3B, 3570) were from American Diagnostica. Rabbit antibodies against the Gla80 form of mMAVS (anti-Gla80) were generated at Eurofins by injection of a peptide corresponding to an N-terminal sequence of mMAVS (CFIRALQICGla^{80}LPGL; Sigma-Aldrich) and purified using an affinity column containing the corresponding peptide.

Cell lines and transfection

HeLa S3 cells, HEK293T (293T) cells, Neuro2a (N2a) cells, and mouse embryonic fibroblasts (MEFs) were maintained in Dulbecco's modified Eagle's medium supplemented with 10% fetal bovine serum. Transfection with protein expression vectors was performed using Genejuice transfection reagent (Merck Millipore) in 293T cells and Lipofectamine 2000 (Thermo Fisher Scientific) in HeLa S3 cells. For cell stimulation, poly(I:C) was mixed with Lipofectamine 2000 and added to cells at a final concentration of 0.25 or 2.5 μg/ml.

Retrovirus-mediated expression of mMAVS mutants

Plat-E cells (*46*) were transfected for 3 days with pMXs-IG containing the gene sequence for green fluorescent protein (GFP) separated by an internal ribosome entry site from WT or 3A (D53A, E70A, E80A) forms of mMAVS. Culture supernatants were collected for isolation of retroviruses. MAVS KO MEFs were infected with MAVS retroviruses or a control virus, and cells were sorted using a FACSAria flow cytometer (BD Biosciences) to obtain those positive for GFP.

Immunoprecipitation (IP) and immunoblot analysis

IP and immunoblot analysis were performed as previously described (*47*).

Subcellular fractionation

293T cells (1×10^5 to 3×10^5) were washed with ice-cold PBS, isolated by centrifugation at 500 × *g* for 2 min at 4°C, and resuspended in 50 μl of KHM buffer (20 mM HEPES-KOH pH 7.5, 250 mM sucrose, 50 mM KCl, 2.5 mM $MgCl_2$, 1 mM Na_3VO_4, 1 mM dithiothreitol (DTT), 1 mg/ml aprotinin) supplemented with digitonin (Wako) at 100 μg/ml. The cell suspension was

incubated on ice for 10 min then centrifuged at 2000 × *g* for 10 min at 4°C. The supernatant was collected as the cytosol fraction. The pellet was washed twice with KHM buffer, resuspended in KHM buffer containing proteinase K (Nacalai) at 0.3 μg/ml, incubated at 37°C for 1 h, and isolated again by centrifugation. The new pellet was resuspended in KHM buffer supplemented with 5 mM phenylmethylsulfonyl fluoride, the suspension was centrifuged at 2000 × *g* for 2 min at 4°C, and the resulting pellet was resuspended in 50 μl of KHM buffer supplemented with 0.05% Nonidet P-40. The suspension was incubated on ice for 30 min then centrifuged at 7000 × *g* for 10 min at 4°C to remove nuclei and cell debris. The resulting supernatant was collected as the luminal and membrane-bound organelle fraction.

Immunocytofluorescence analysis

293T cells that had been transiently transfected with plasmids encoding the indicated proteins for 20 h on coverslips were fixed with 2% paraformaldehyde at 37°C for 15 min, washed with PBS, and permeabilized for 10 min at room temperature with 0.2% Triton X-100 in PBS. They were then washed twice with PBS before incubation at room temperature, first for 1 h in blocking solution (2% bovine serum albumin, 2% fetal bovine serum, 0.03% sodium azide in PBS) then for 2 h in blocking solution containing primary antibodies. After washing with PBS, cells were incubated for 2 h at room temperature in blocking solution containing appropriate Alexa Fluor 488-, Alexa Fluor 594-, or Alexa Fluor 633-conjugated secondary antibodies (1:1000 dilution; Thermo Fisher Scientific). Images were acquired with an LSM880 laser confocal microscope (Zeiss) and processed using ZEN (Zeiss) and ImageJ (National Institutes of Health) software.

Image analysis

All image analysis was performed with ImageJ software. Immunofluorescence images from split mNG2 assays were quantified at three randomly selected sample sites per coverslip, with three biological replicates. The region of interest (ROI) was manually generated based on the Myc signal, and mNG2 and Myc intensity was quantified in each ROI. The intensity of mNG2 was normalized against that of Myc. Images were processed with a Gaussian filter (sigma = 0.75) to eliminate the noise independent of the mNG2 signal.

Purification of His_{10}-tagged MAVS under denaturing conditions

His_{10}-Flag- and His_{10}-tagged proteins were purified as described previously (*48*) with some modifications. Transfected 293T cells (1.5×10^6/ml) in a 100-mm dish were harvested in ice-cold PBS and lysed in 1 ml of a solution containing 6 M guanidine-HCl, 10 μM $CaCl_2$, 0.1 M sodium phosphate buffer (pH 8.0), and 5 mM imidazole. The lysate was subjected to ultrasonic treatment to reduce its viscosity, mixed with 10 μl of Talon Co^{2+} resin (Clontech), and incubated for 1 h at 4°C with rotation. The resin was then washed twice with 500 μl of Talon wash buffer (300 mM NaCl, 50 mM sodium phosphate pH 8.0, 5 mM imidazole) before resuspending in 50 μl of 1× Laemmli SDS sample buffer. In the case of mouse liver, the tissue was lysed in the same 6 M guanidine-HCl solution and the Co^{2+} resin was washed with Talon wash buffer containing 150 mM imidazole.

Reporter gene analysis

293T cells seeded in 48-well plates were transiently transfected for 24 h with 2 ng of *Renilla* luciferase reporter plasmid carrying the mouse *Ifnb1* promoter, 100 ng or 500 ng of hMAVS expression or corresponding control plasmid, and 20 ng of pGL3-control (Promega) encoding

firefly luciferase as an internal control. Cell lysates were then assayed for luciferase activity by dual-luciferase reporter assay (Promega), and the activity of *Renilla* luciferase was normalized against that of firefly luciferase.

Proteomics analysis

Mass spectrometric analysis and identification of post-translational modifications for Fig. S1 were performed as previously described, except that Finnigan LTQ mass spectrometry (Thermo Scientific) was used (*49*).

Detection of carboxylation of His_{10}-Flag-tagged hMAVS ΔC for Fig. S2 was performed as described previously(*50, 51*) with some modifications. Cell pellets expressing His_{10}-Flag-tagged MAVS ΔC were lysed with SDS buffer (100 mM NH_4HCO_3, 2% SDS) and heated at 95°C for 10 min. Following centrifugation (4°C, 21,600 xg, 10 min), the lysate was diluted with 1.6 volumes of Denature buffer (100 mM NH_4HCO_3, 137 mM NaCl, 1 mM ethylenediaminetetraacetic acid, 5% glycerol, 0.05% Lubrol PX, 1% Triton X-100, 0.1% SDS, 1 mM DTT, 1 mM Phenylmethylsulfonyl fluoride, 4 μg/μL aprotinin, 4 μg/μL leupeptin). Anti-Flag M2 Affinity Gel (SIGMA) was added to the sample and was rotated at 4°C for 2 h. After flashing it, the precipitate was washed once with Urea wash buffer (100 mM Hepes-NaOH [pH 7.8], 200 mM NaCl, 1% Tx-100, 2 M Urea), once with ConA wash buffer (100 mM Hepes-NaOH [pH 7.8], 500 mM NaCl, 1% Tx-100), and once with wash buffer B (100 mM NH_4HCO_3, 180 mM NaCl). Elution buffer (100 mM NH_4HCO_3, 137 mM NaCl, 150 ng/μl Flag peptide, 12 mM sodium deoxycholate) was added to the precipitate, and was agitated at room temperature for 15 min. After flashing it, the eluate including purified His_{10}-Flag-tagged MAVS proteins was collected. The eluate was reduced with 10 mM DTT at 60 °C for 30 min, alkylated with 22 mM iodoacetamide at 37 °C for 30 min in the dark, and digested with 0.4 μg of trypsin (Sigma) at 37 °C for 18 h in the dark. After removing the detergents by PTS method, the peptides were desalted using Mono-Spin C18 column (GL Sciences), and the dried peptides were dissolved in distilled water containing 2% acetonitrile and 0.1% TFA.

The LC-MS/MS analyses were performed using a MS spectrometer (Orbitrap Astral; Thermo Fisher Scientific) equipped with a nano ultra-HPLC system (Vanquish Neo; Thermo Fisher Scientific). The peptides were loaded to a capillary column (Aurora Ultimate 25×75 C18 UHPLC column; IonOptics). The column was heated to 55 °C with the Column Oven PRSO-V2 (Sonation Lab Solutions) and the flow rate was set to 650 nL/min and turned to 300 nL/min at the start of the active gradient. Mobile phase A and B were 0.1% formic acid in water (Kanto Kagaku) and 0.1% formic acid/100% acetonitrile (Kanto Kagaku), respectively. The loaded peptides were separated by the following gradient: 0% to 2% B in 0.5 min, 2% to 4.8% B in 0.4 min, 4.8% to 20.0% B in 14 min, 20.0% to 35.0% B in 30.4 min, 35% to 76% B in 11.2 min, 76% to 99% B in 0.1 min and 99% B for 3.4 min. The column was washed for 5 min at 100% B and 650 nL/min, followed by fast equilibration on the Vanquish Neo LC with an upper-pressure limit of 1500 bar. For the DDA experiments, the Orbitrap Astral mass spectrometer was operated with a fixed cycle time of 0.3 s and with a full scan range of 375–2000 m/z at a resolution of 120,000 (positive ion mode). The automatic gain control (AGC) was set to 500%. Precursor ion selection width was kept at 2-Th and peptide fragmentation was achieved by HCD (Normalized Collision Energy 27%). Fragment ion scans were recorded at a resolution of 80,000 and maximum fill time of 20 ms. The raw spectra were extracted using Proteome Discoverer 3.1 (Thermo Fisher Scientific) and searched against the *homo sapiens* FASTA with the following settings: “cleavage” was set to trypsin. “missed cleavage” was allowed up to 2. “mass

tolerances" were set to 10 ppm and 0.02 Da. As for protein modifications, we set carbamidomethylation (+57.021 Da) at Cys as static (fixed) modifications for peptide, oxidation (+15.995 Da) at Met and carboxylation (+44.010 Da) at Glu/Asp as dynamic (non-fixed) modifications for peptide.
Liquid chromatography and tandem mass spectrometry (LC-MS/MS) analysis of MAVS interactors was also performed as previously described (*52*). Raw data were directly analysed against the SwissProt database (Homo sapiens, TaxID=9606_and_subtaxonomies, 42346 entry) using Skyline with the following parameter settings: (a) Lys-C was used as the cleavage enzyme, and up to two missed cleavage were allowed.; (b) mass tolerance for MS1 and MS2 was set to 20 ppm; (c) oxidation of methionine as a variable modification; (d) precursor charge: 2,3.For the Volcano plot shown in Figure 4A, ion intensities of each protein were normalized against the total ion intensity of each sample and fold changes were calculated from an average of n = 4 biologically independent experiments. *P* values were calculated using the unpaired two-tailed Student's t test.

Statistical analysis

Quantitative data are presented as means ± standard deviation (SD) or ± standard error of the mean (SEM) unless indicated otherwise. They were compared with the one sample *t* test or unpaired Student's *t* test, one-way analysis of variance (ANOVA), and Dunnett's post hoc test, Dunnett's multiple comparison test, Kruskal-Wallis test followed by Dunn's multiple-comparison test, Mann-Whitney *U* test, or log-rank test. A P value < 0.05 was considered statistically significant.

Use of AI Tools for Language Editing

ChatGPT-4o (OpenAI) was used solely to assist with language editing during the preparation of the manuscript. The following prompts were used:
- "Could you provide a possible revision of the following paragraph to improve clarity and make it more concise, while preserving the scientific meaning?"
- "How might this sentence be rewritten in a more formal academic tone?"
- "Please suggest a smoother way to connect these two sentences in scientific English."

Fig. S1.

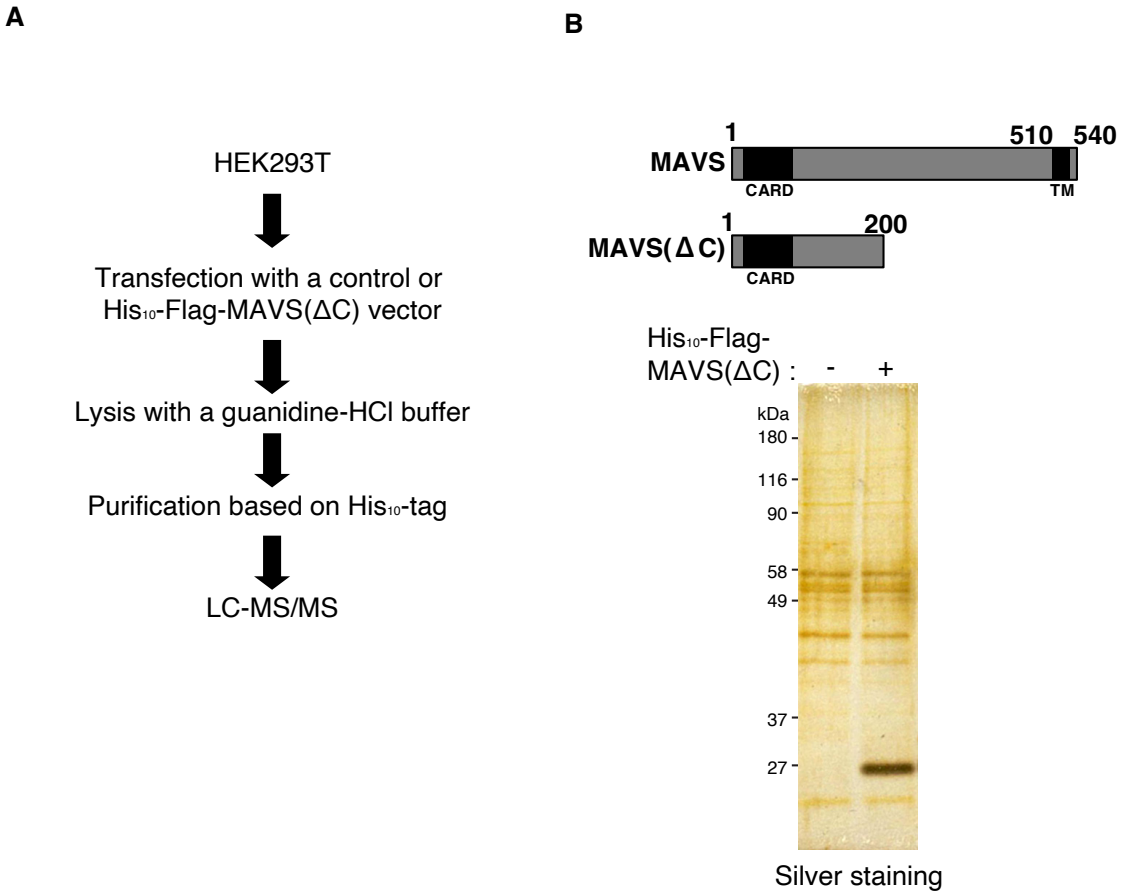

C

Site	Peptide sequence	Position	Score	Significance
D53	R.**D**(CO_2)TLWHLFNTLQR.R	53-64	304	97.5
E70	R.RPGWV**E**(CO_2)YFIAALR.G	65-77	442	99.4
E80, D83	R.GC**E**(CO_2)LV**D**(CO_2)LADEVASVYSYQPR.T	78-97	186	90.2

Fig. S1. MAVS is carboxylated in cells. A, Scheme for purification and analysis of His_{10}-Flag-tagged hMAVS(ΔC) from transfected 293T cells. **B**, 293T cells transiently transfected with an expression plasmid for His_{10}-Flag-hMAVS(ΔC) or with the corresponding empty vector for 20 h were lysed with denaturing buffer containing 6 M guanidine-HCl, and the His_{10}-Flag-tagged protein was isolated using Co^{2+} resin, subjected to SDS-polyacrylamide gel electrophoresis (PAGE), and stained with silver. **C**, The isolated His_{10}-Flag-hMAVS(ΔC) protein was analysed by LC-MS/MS, and the sequences of identified carboxylated peptides assigned by MODIRO v1.1 are shown.

Fig. S2.

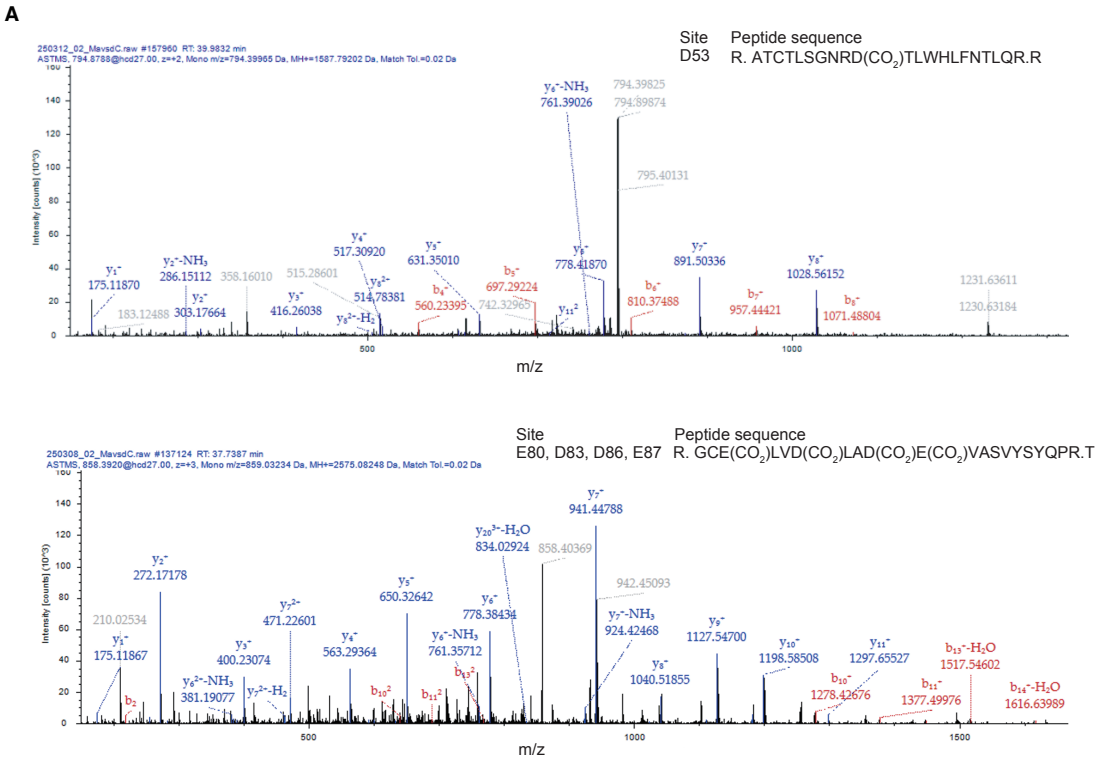

Fig. S2. The MS/MS spectrum of the carboxyl-peptide of the MAVS protein. A, His_{10}-Flag-hMAVS(ΔC) proteins was purified by anti-Flag antibody and analyzed by Orbitrap Astral. The sequences of identified carboxylated peptides were assigned by Proteome Discoverer3.1. Results are representative of two independent experiments.

Fig. S3.

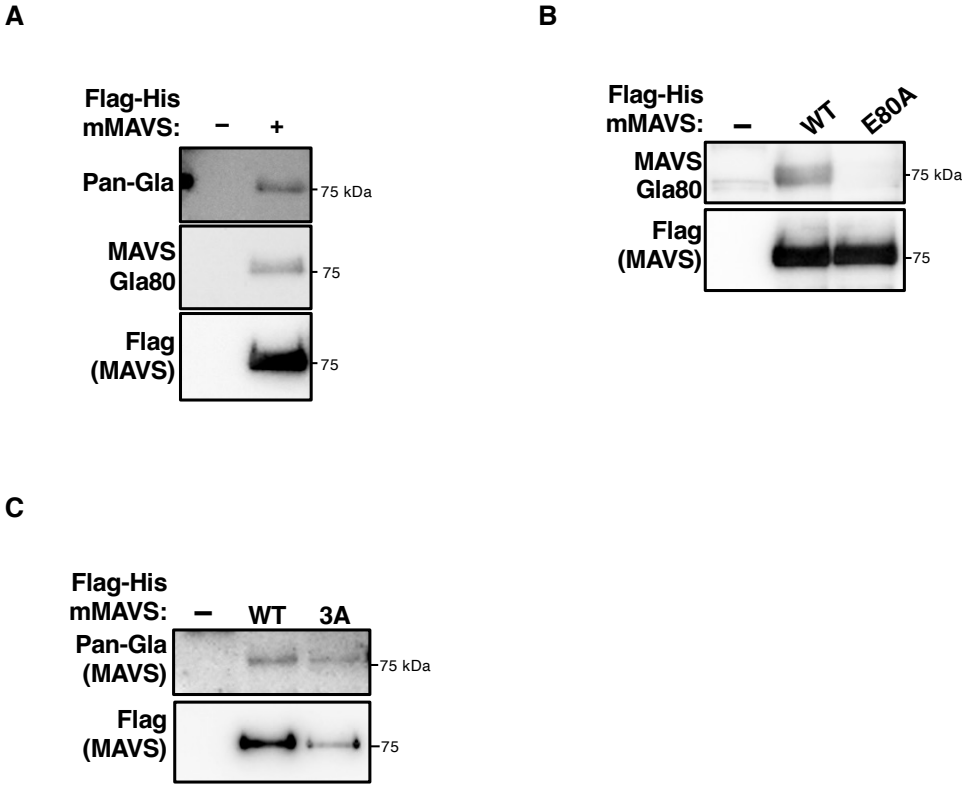

Fig. S3. MAVS is carboxylated in cells. A, 293T cells were transiently transfected with expression vectors for His_{10}-Flag-tagged mMAVS for 20 h in the presence of 20 μM vitamin K1 (VK1), then lysed in the absence of ethylene glycol tetraacetic acid (EGTA) and DTT. His_{10}-tagged proteins were then isolated using Co^{2+} resin and subjected to immunoblot analysis with antibodies against pan-Gla, Flag, and Glu^{80}-carboxylated (Gla80) form of mMAVS. **B,** 293T cells were transiently transfected with expression vector for His_{10}-Flag-tagged mMAVS or mMAVS(E80A) for 20 h in the presence of 20 μM VK1, then lysed in the presence of 6 M guanidine-HCl. The His_{10}-tagged proteins were then isolated using Co^{2+} resin and subjected to immunoblot analysis with antibodies against Flag and Gla80. **C,** 293T cells were transiently transfected with expression vector for His_{10}-Flag-tagged mMAVS or mMAVS(3A) for 20 h in the presence of 20 μM VK1, then lysed in the presence of 6 M guanidine-HCl. His_{10}-tagged proteins were isolated using Co^{2+} resin and subjected to immunoblot analysis with antibodies against Flag and pan-Gla. Results are representative of at least three independent experiments. Note that E70A/E80A/D83A (3A) mutant of mMAVS expressed in 293T cells was still recognized by pan-Gla antibodies, suggesting that MAVS is carboxylated also at sites other than these residues in the CARD domain.

Fig. S4.

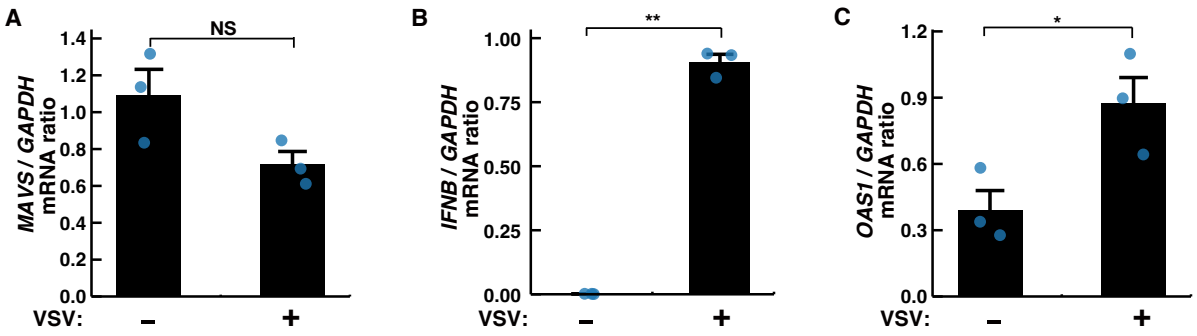

Fig. S4. VSV infection does not increase MAVS mRNA levels. A–C, 293T cells were infected for 6 h with VSV at an MOI of 1, then assayed for *MAVS* mRNA (A), *IFNB* mRNA (B), and *OAS1* mRNA (C) by RT-qPCR. Results are means ± SEM from three independent experiments. Statistical analyses were performed using Student's *t* test (**P* < 0.05, ***P* < 0.01. NS, not significant).

Fig. S5.

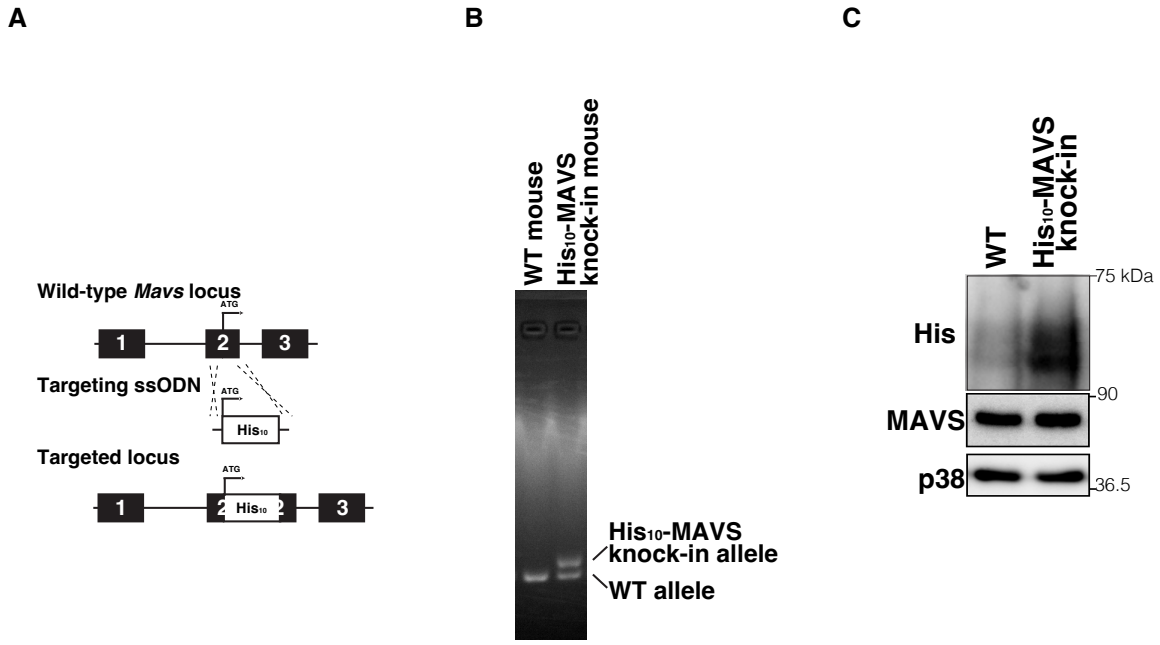

Fig. S5. Generation of a His_{10}-MAVS knock-in mouse. A, Scheme showing the generation of His_{10}-MAVS knock-in (KI) mice. Numbered boxes represent exons. ssODN, single-stranded oligodeoxynucleotide. **B**, Genomic DNA isolated from the tail of 10-day-old WT or heterozygous His_{10}-MAVS KI mice was subjected to polymerase chain reaction (PCR) analysis with primers that recognize the WT and knock-in alleles of the MAVS gene. **C**, Immunoblot analysis of the liver of 2-month-old WT or heterozygous His_{10}-MAVS KI mice with antibodies to His, to mMAVS, and to p38 MAPK (loading control). The His_{10}-MAVS protein was expressed at a level similar to that of endogenous MAVS in WT mice. Similar results were obtained in two independent experiments.

Fig. S6.

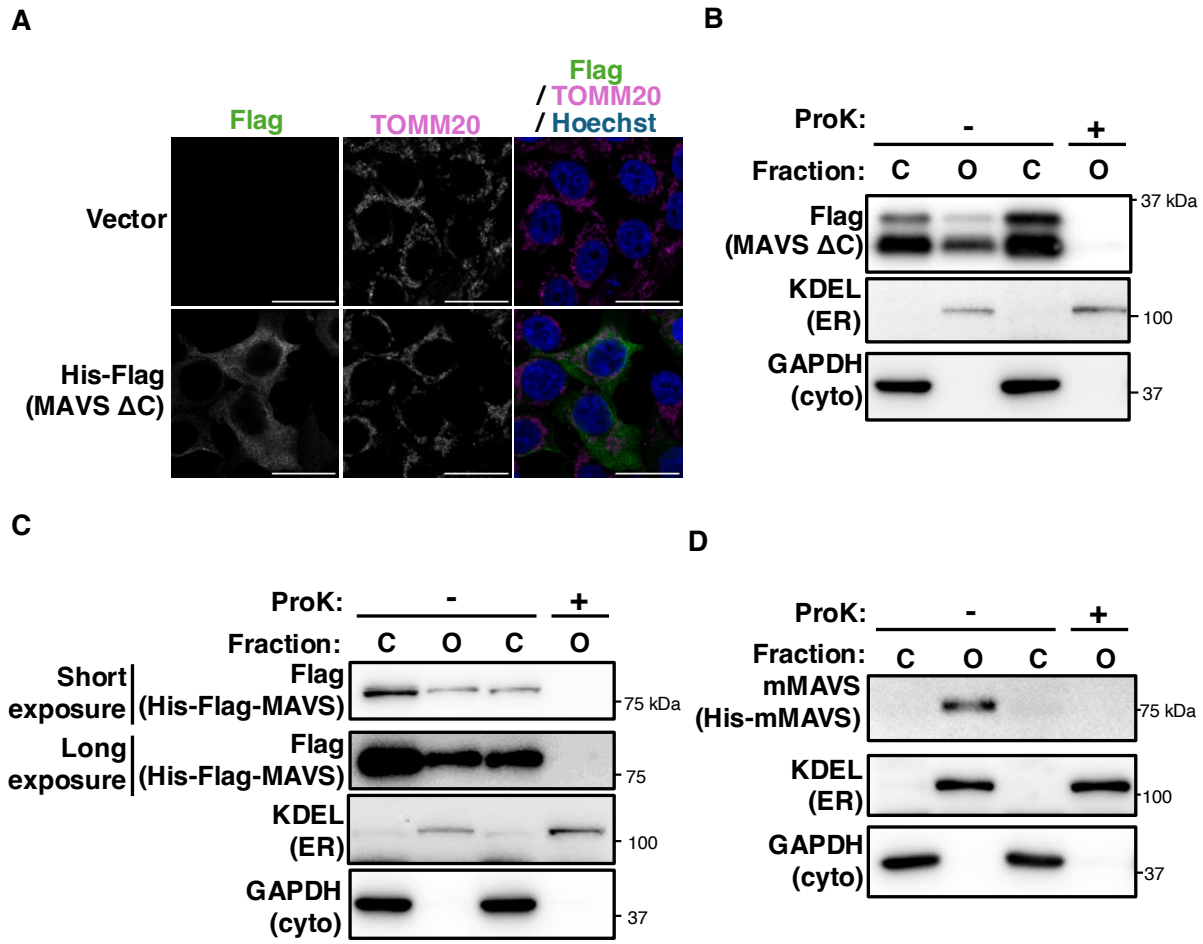

Fig. S6. MAVS ΔC and full-length MAVS are not mistargeted to the ER lumen. A, 293T cells were transiently transfected with expression vectors for His-Flag-MAVS ΔC (or the corresponding empty vector) for 20 h. The cells were fixed and subjected to immunofluorescence staining with antibodies against Flag or TOMM20, and counterstained with Hoechst. Scale bars = 20 μm. Results are representative of at least three independent experiments. **B**, 293T cells were transiently transfected with expression vectors for His-Flag-MAVS ΔC for 20 h, lysed, and subjected to subcellular fractionation into cytosol (C) and organelle-bound (O) fractions, followed by immunoblot analysis with antibodies against Flag, KDEL (ER marker), and GAPDH (cytosolic marker). An O fraction was resuspended in KHM buffer and treated with or without proteinase K (proK) for 1h. **C**, 293T cells were transiently transfected with expression vectors for His-Flag-full-length MAVS for 20 h, lysed, and subjected to subcellular fractionation into cytosol (C) and organelle-bound (O) fractions followed by immunoblot analysis with antibodies against Flag, KDEL (ER marker), and GAPDH (cytosolic marker). An O fraction was resuspended in KHM buffer with or without proK. **D,** His-KI mouse-derived MEFs were subjected to subcellular fractionation into cytosol (C) and organelle-bound (O) fractions followed by immunoblot analysis with antibodies against mouse MAVS, KDEL (ER marker), and GAPDH (cytosolic marker). An O fraction was resuspended in KHM buffer and treated with or without proK for 1h. Results are representative of at least three independent experiments.

Fig. S7.

A

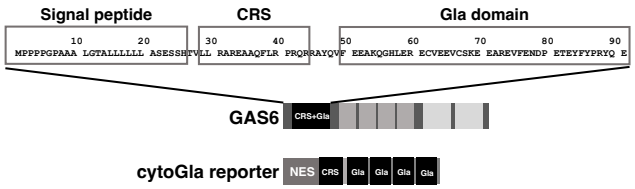

Fig. S7. Domain structures of mouse GAS6 and the reporter designed for detection of cytoplasmic protein carboxylation (cytoGla). A, The reporter consists of four tandemly repeated carboxylation (Gla) domains and a conserved recognition sequence (CRS) for GGCX derived from mouse GAS6, as well as a nuclear export signal (NES) of MAP2K1.

Fig. S8.

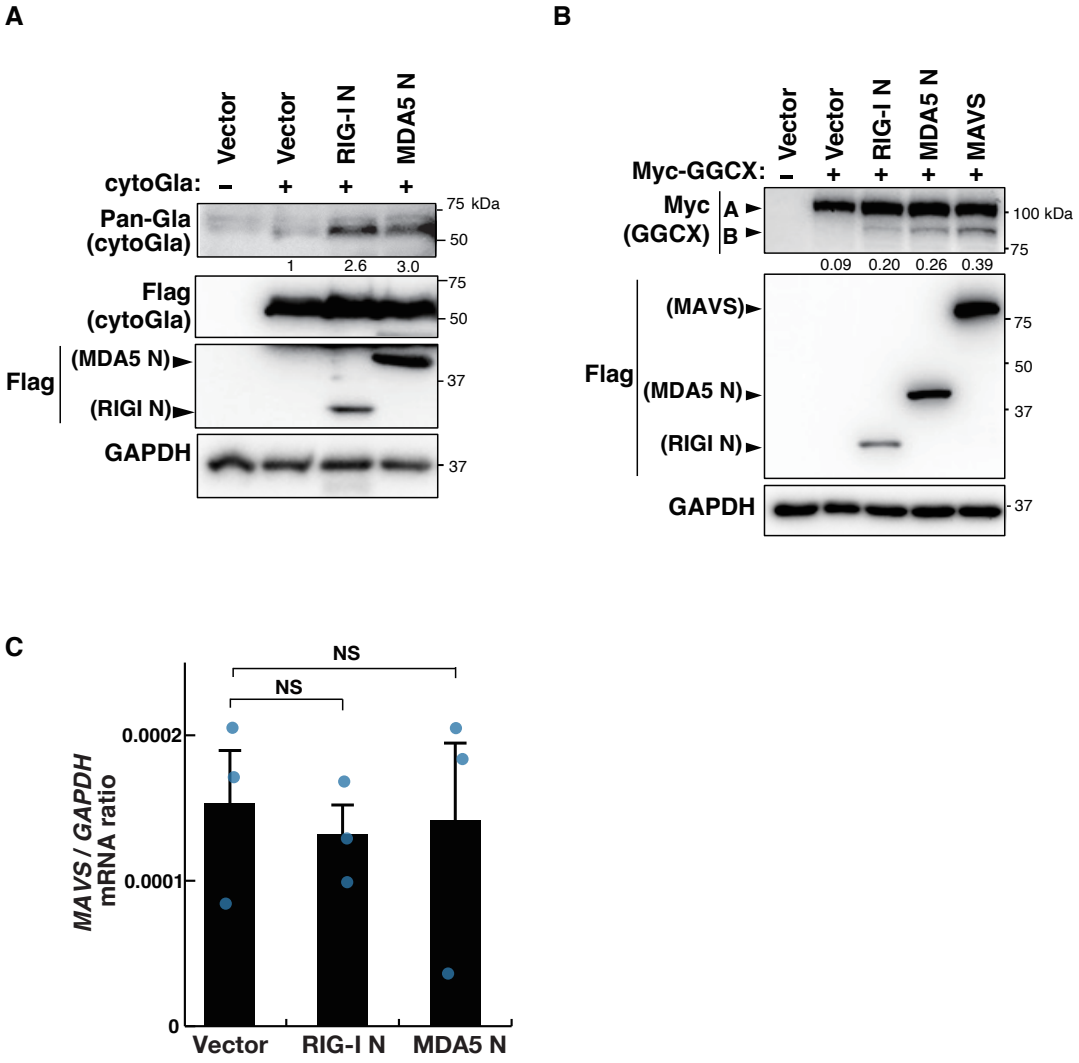

Fig. S8. Expression of constitutively active RIG-I and MDA5 forms induce GGCX B and carboxylation of cytoGla. A, 293T cells maintained in the presence of VK1 were transiently transfected with expression vectors for Flag-cytoGla and Flag-RIG-I N, or Flag-MDA5 N for 20 h, lysed, and subjected to immunoblot analysis with antibodies against pan-Gla, Flag, and GAPDH. The signal intensities of pan-Gla relative to Flag were quantified and shown below the gels (normalized to lane 2). Results are representative of three independent experiments. **B,** 293T cells were transiently transfected with expression vectors for Myc-mGGCX and Flag-hMAVS, Flag-RIG-I N, or Flag-MDA5 N for 20 h, lysed, and subjected to immunoblot analysis with antibodies against Myc, Flag, and GAPDH. The signal intensities of GGCX (B) relative to GGCX (A) were quantified and shown below the gels. Results are representative of three independent experiments. **C,** 293T cells were transiently transfected with plasmids carrying RIG-I N or MDA5 N for 20 h, then assayed for *MAVS* mRNA by RT-qPCR. Results are means ± SEM from three independent experiments. Statistical analyses were performed using one-way ANOVA and Dunnett's post hoc test versus controls (NS, not significant).

Fig. S9.

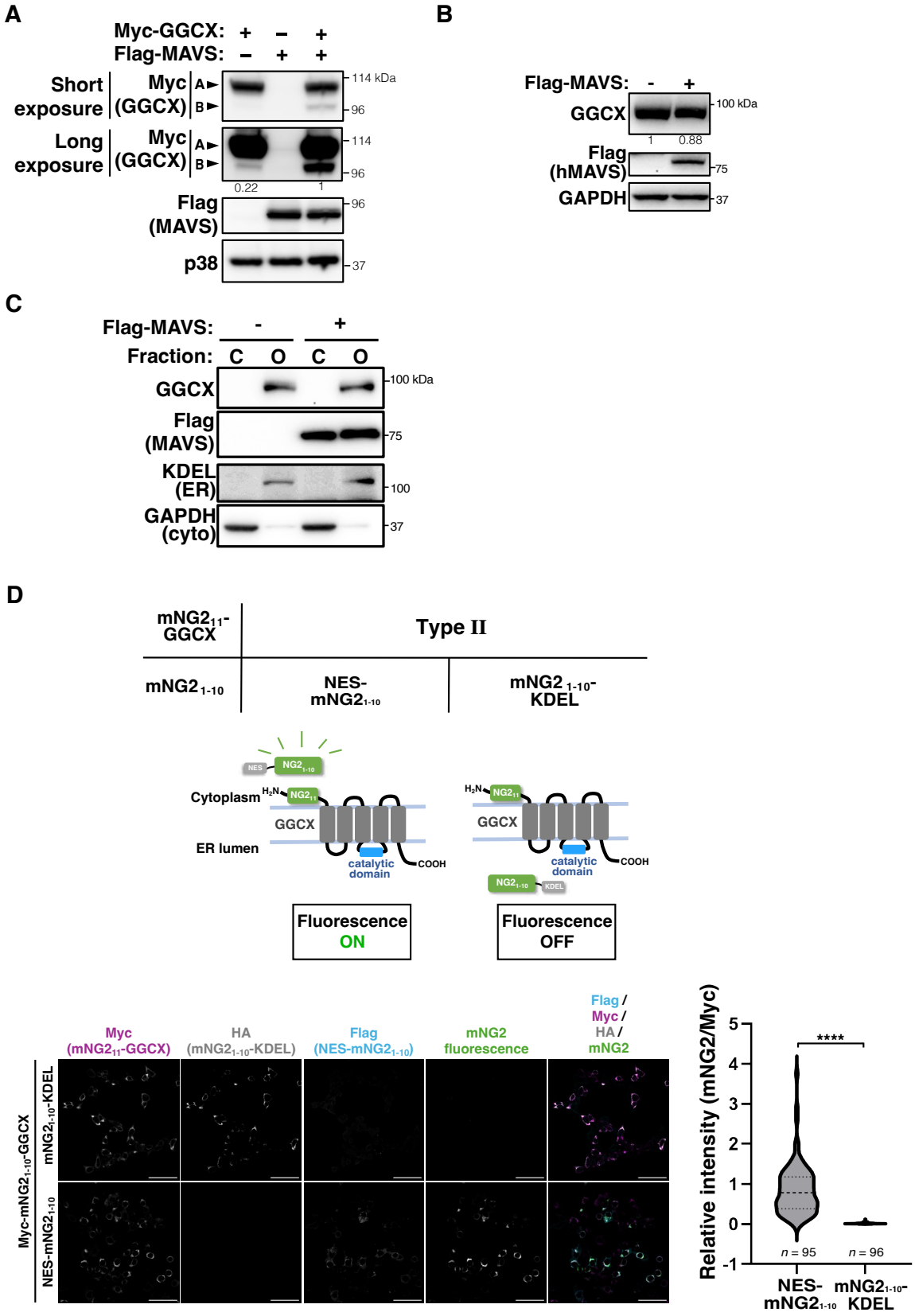
A
Myc-GGCX: + – +
Flag-MAVS: – + +
Short exposure
Long exposure
Myc (GGCX)
A
B
114 kDa
96
114
96
0.22
1
Flag (MAVS)
96
p38
37
B
Flag-MAVS: - +
GGCX
100 kDa
1
0.88
Flag (hMAVS)
75
GAPDH
37
C
Flag-MAVS: - +
Fraction: C O C O
GGCX
100 kDa
Flag (MAVS)
75
KDEL (ER)
100
GAPDH (cyto)
37
D
mNG2 11-GGCX
Type II
mNG2 1-10
NES-mNG2 1-10
mNG2 1-10-KDEL
Cytoplasm
ER lumen
GGCX
catalytic domain
COOH
Fluorescence ON
Fluorescence OFF
Myc (mNG2 11-GGCX)
HA (mNG2 1-10-KDEL)
Flag (NES-mNG2 1-10)
mNG2 fluorescence
Flag / Myc / HA / mNG2
Myc-mNG2 1-10-GGCX
mNG2 1-10-KDEL
NES-mNG2 1-10
Relative intensity (mNG2/Myc)
****
n = 95
n = 96
NES-mNG2 1-10
mNG2 1-10-KDEL

Fig. S9. Membrane topology of GGCX and association between MAVS and GGCX. A, 293T cells were transiently transfected with expression vectors for Myc-mGGCX and Flag-hMAVS for 20 h, lysed, and subjected to immunoblot analysis with antibodies against Myc, Flag, and p38 MAPK. The signal intensities of GGCX (B) relative to GGCX (A) were quantified and shown below the gels (normalized to lane 3). Results are representative of three independent experiments. **B**, 293T cells were transiently transfected with expression vectors for Flag-hMAVS for 20 h, lysed, and subjected to immunoblot analysis with antibodies against GGCX, Flag, and GAPDH. The signal intensities of GGCX relative to GAPDH were quantified and shown below the gels (normalized to lane 1). Results are representative of three independent experiments. **C,** 293T cells were transiently transfected with expression vectors for Flag-hMAVS for 20 h, lysed, and subjected to subcellular fractionation into cytosol (C) and organelle-bound (O) fractions, followed by immunoblot analysis with antibodies against GGCX, Flag, KDEL (ER marker), and GAPDH (cytosolic marker). An O fraction was resuspended in KHM buffer without proK. Results are representative of three independent experiments. **D,** 293T cells were transiently transfected for 20 h with expression vectors for mGGCX tagged at its N-terminus with Myc-$mNG2_{11}$, Flag-tagged NES-$mNG2_{1–10}$ (cytosolic), and HA-tagged $mNG2_{1–10}$-KDEL (ER lumen). Nuclear export signal (NES) is derived from MAP2K1. Cells were then fixed and subjected to immunofluorescence staining with antibodies against Myc, Flag, and HA. Cells expressing NES-$mNG2_{1–10}$ and $mNG2_{11}$-GGCX displayed a high mNG2 fluorescence intensity. Representative images (scale bars = 50 μm) are shown together with a violin plot for the relative mNG2/Myc fluorescence intensity ratio determined for the indicated numbers of cells examined in three independent experiments. Statistical analyses were performed using Kruskal-Wallis test followed by Dunn's multiple-comparison test (****$P < 0.0001$).

Fig. S10.

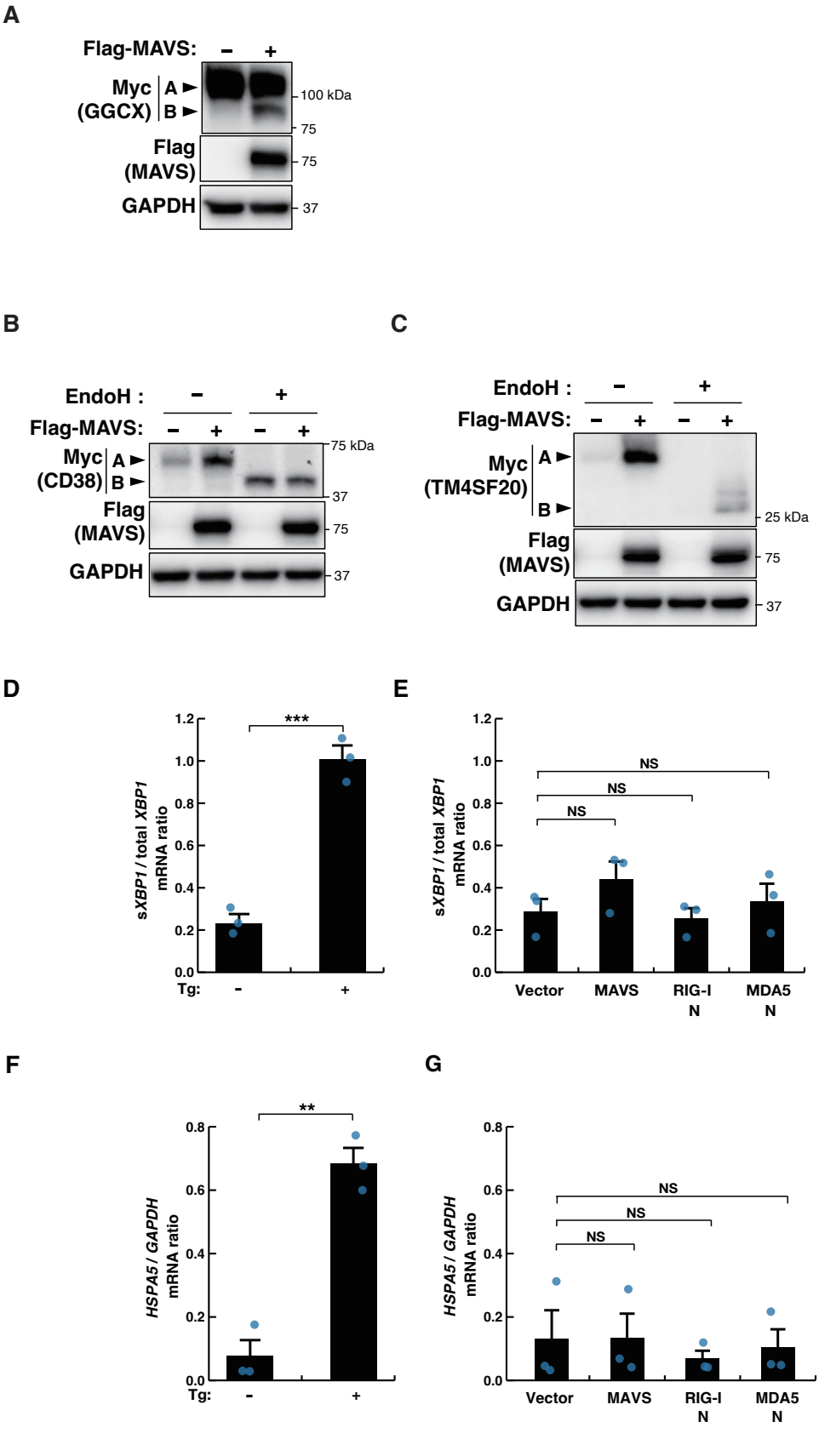
A
Flag-MAVS: – +
Myc (GGCX) A ► B ►
100 kDa
75
Flag (MAVS)
75
GAPDH
37
B
EndoH : – +
Flag-MAVS: – + – +
Myc (CD38) A ► B ►
75 kDa
37
Flag (MAVS)
75
GAPDH
37
C
EndoH : – +
Flag-MAVS: – + – +
Myc (TM4SF20) A ► B ►
25 kDa
Flag (MAVS)
75
GAPDH
37
D
sXBP1 / total XBP1 mRNA ratio
***
Tg: - +
E
sXBP1 / total XBP1 mRNA ratio
NS
NS
NS
Vector
MAVS
RIG-I N
MDA5 N
F
HSPA5 / GAPDH mRNA ratio
**
Tg: - +
G
HSPA5 / GAPDH mRNA ratio
NS
NS
NS
Vector
MAVS
RIG-I N
MDA5 N

Fig. S10. MAVS overexpression does not induce ER stress markers or alter glycosylation of CD38 and TM4SF20. A–C, 293T cells were transiently transfected with expression vectors for Flag-hMAVS and Myc-GGCX (A), Myc-CD38 (B), or Myc-TM4SF20 (C) for 20 h, lysed, and subjected to Endoglycosidase H (Endo H) treatment for 5 h (B, C) followed by immunoblot analysis with antibodies against Myc, Flag, and GAPDH. Results are representative of three independent experiments. **D–G,** 293T cells were treated with 250 nM thapsigargin (Tg) for 6 h (D, F), or transiently transfected with plasmids for MAVS, RIG-I N, or MDA5 N for 20 h (E, G), then assayed for spliced XBP1 mRNA, total XBP1 mRNA (D, E), and Binding immunoglobulin protein (BiP) mRNA (F, G) by RT-qPCR. The y-axis scale is the same between (D) and (E), and between (F) and (G). Results are means ± SEM from three independent experiments. Statistical analyses in (D, F) were performed using Student's *t* test (***P* < 0.01, ****P* < 0.001), and (E, G) were performed using one-way ANOVA and Dunnett's post hoc test versus Vector control (NS, not significant).

Fig. S11.

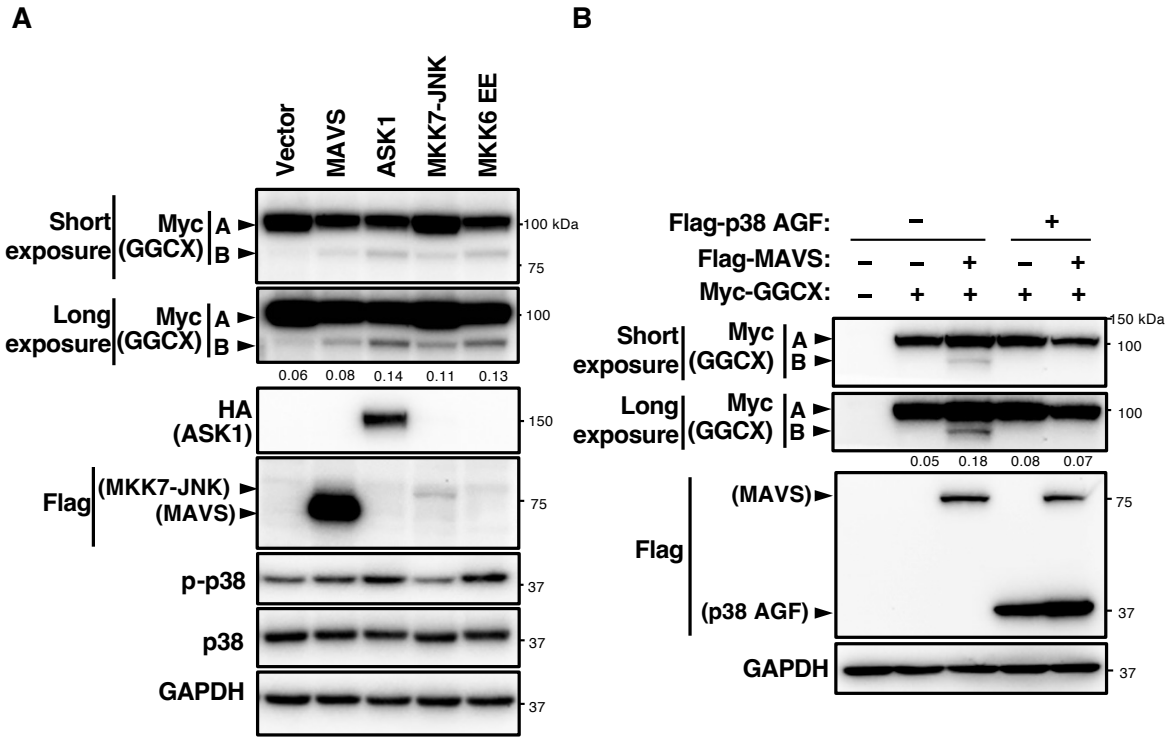

Fig. S11. p38 MAPK activation induces GGCX B. A, 293T cells were transiently transfected with expression vectors for Myc-mGGCX and Flag-hMAVS**,** HA-ASK1, Flag-MKK7-JNK, or constitutively active MKK6 EE for 20 h, lysed, and subjected to immunoblot analysis with antibodies against Myc, Flag, HA, p-p38, p38, and GAPDH. The signal intensities of GGCX (B) relative to GGCX (A) were quantified and shown below the gels. Results are representative of three independent experiments. **B**, 293T cells were transiently transfected with expression vectors for Myc-mGGCX, Flag-hMAVS, and a dominant negative p38 AGF for 20 h, lysed, and subjected to immunoblot analysis with antibodies against Myc, Flag, and GAPDH. The signal intensities of GGCX (B) relative to GGCX (A) were quantified and shown below the gels. Results are representative of three independent experiments.

Fig. S12.

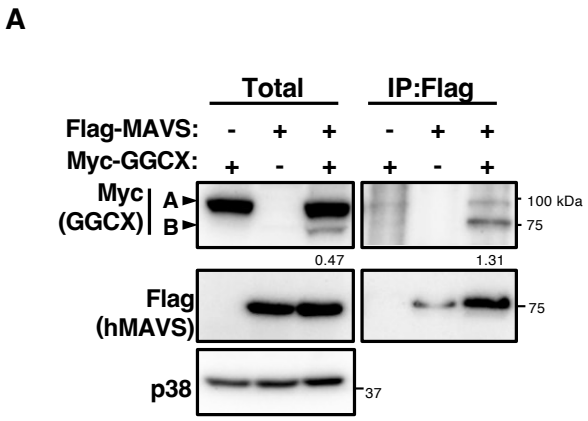

Fig. S12. MAVS selectively interacts with non-glycosylated GGCX B. A, 293T cells transiently transfected for 20 h with expression plasmids for Flag-hMAVS and Myc-GGCX were subjected to IP with antibodies against Flag, and the resulting precipitates as well as the original cell lysates (Total) were subjected to immunoblot analysis with antibodies against Myc, Flag, and p38. The signal intensities of GGCX (B) relative to GGCX (A) were quantified and shown below the gels. Results are representative of three independent experiments.

Fig. S13.

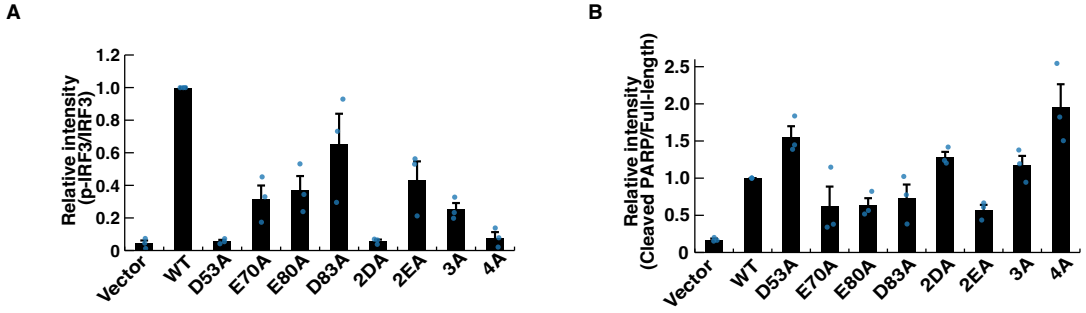

Fig. S13. Effects of carboxylation site mutations on MAVS-mediated activation of IRF-3 and caspase. A,B, The signal intensities shown in Fig. 3B for p-IRF3 relative to IRF3 (A) and cleaved PARP relative to full-length PARP (B) were quantified and plotted (normalized to lane 2). Results are means ± SEM from three independent experiments.

Fig. S14.

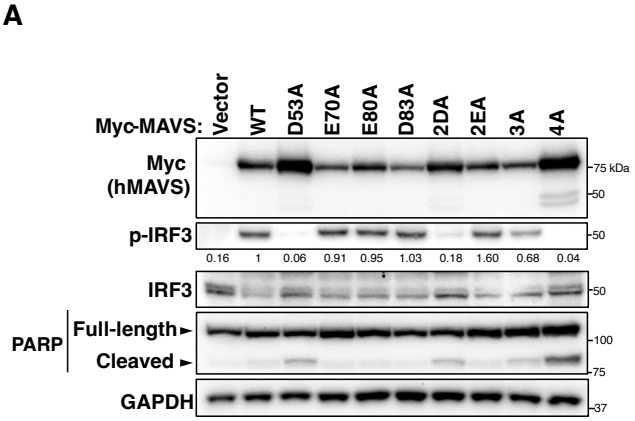

Fig. S14. Effects of pan-caspase inhibitor zVAD on MAVS-induced activation of IRF-3. A, 293T cells transiently transfected for 20 h with expression plasmids for Myc-tagged WT or mutant forms of hMAVS in the presence of 50 μM zVAD-FMK were lysed and subjected to immunoblot analysis with antibodies against Myc, p-IRF3, IRF-3, PARP, and GAPDH. The signal intensities of p-IRF3 relative to IRF3 were quantified and shown below the gels (normalized to lane 2). Results are representative of three independent experiments.

Fig. S15.

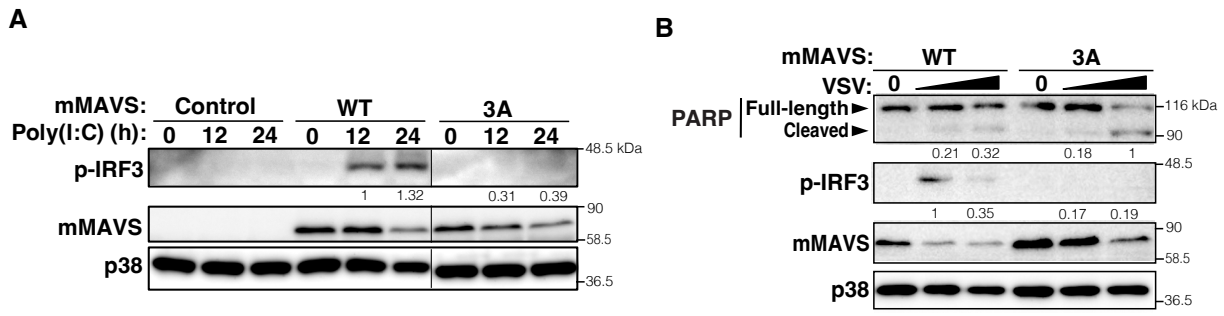

Fig. S15. Mutation of MAVS carboxylation sites inhibits IRF3 activation but promotes caspase activation. A,**B**, MEFs isolated from MAVS KO mice were infected with retroviruses encoding WT or 3A (D53A, E70A, E80A) mutant forms of mMAVS. Cells were then transfected with 0.25 μg/ml poly(I:C) for the indicated times (**A**) or infected with VSV for 12 h (**B**), then subjected to immunoblot analysis with antibodies against p-IRF3, mMAVS, PARP, and p38 MAPK. The signal intensities of p-IRF3 relative to p38 (normalized to lane 5) (**A**), those of cleaved PARP relative to full-length PARP (normalized to lane 6) or those of p-IRF3 relative to p38 (normalized to lane 2) (**B**), were quantified and shown below the gels. Results are representative of three independent experiments.

Fig. S16.

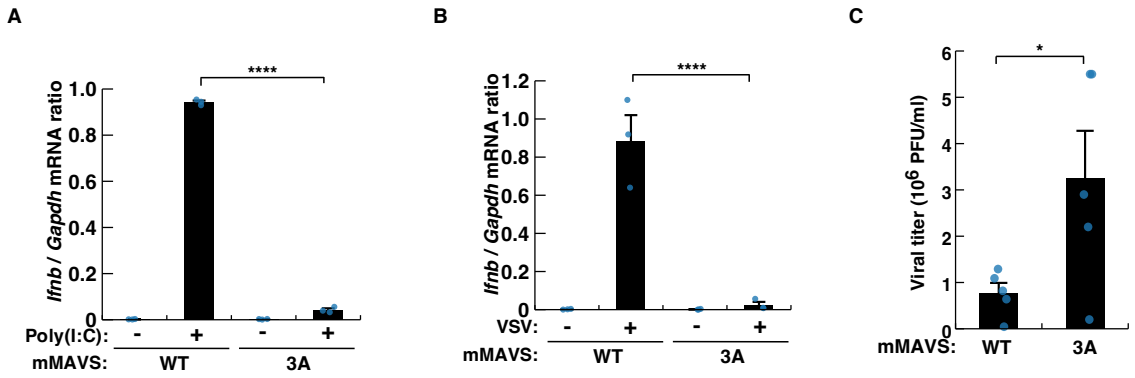

Fig. S16. Effects of MAVS 3A mutation on IFN-β induction and viral replication in the presence of zVAD. A,**B**, MEFs isolated from MAVS KO mice were infected with retroviruses encoding either WT or 3A (D53A, E70A, E80A) mutant forms of mMAVS, transfected with 0.25 μg/ml) for 6h (**A**), or infected for 12 h with VSV at an MOI of 1 (B) in the presence of 50 μM zVAD-FMK, and assayed for *Ifnb1* mRNA by RT-qPCR. Results are means ± SEM from three independent experiments. **C**, MAVS KO MEFs expressing WT or 3A mutant forms of mMAVS were infected for 24 h with VSV at an MOI of 0.3, washed, incubated for 24 h in fresh medium in the presence of 50 μM zVAD, then collected for assay of VSV titer based on plaque-forming units (PFU) by standard plaque assay. Results are means ± SEM from five independent experiments. Statistical analyses in (A-C) were performed using unpaired Student's *t* test (**P* < 0.05, *****P* < 0.001).

Fig. S17.

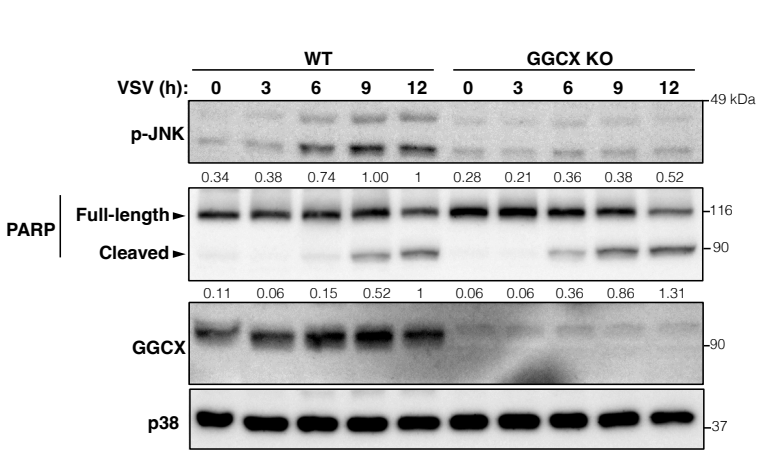

Fig. S17. Depletion of GGCX in neuronal cell line N2a attenuated interferon-inducing signaling but enhanced caspase activation in response to VSV infection. A, WT or GGCX KO Neuro2a cells were infected with VSV at an MOI of 0.3 for the indicated times and analysed by immunoblot using antibodies against PARP, GGCX, p38 MAPK, and p-JNK as an indicator of activation of interferon-inducing signaling. Results are representative of two independent experiments. The signal intensities of p-JNK relative to p38 and cleaved PARP relative to full-length PARP were quantified and shown below the gels (normalized to lane 5).

Fig. S18.

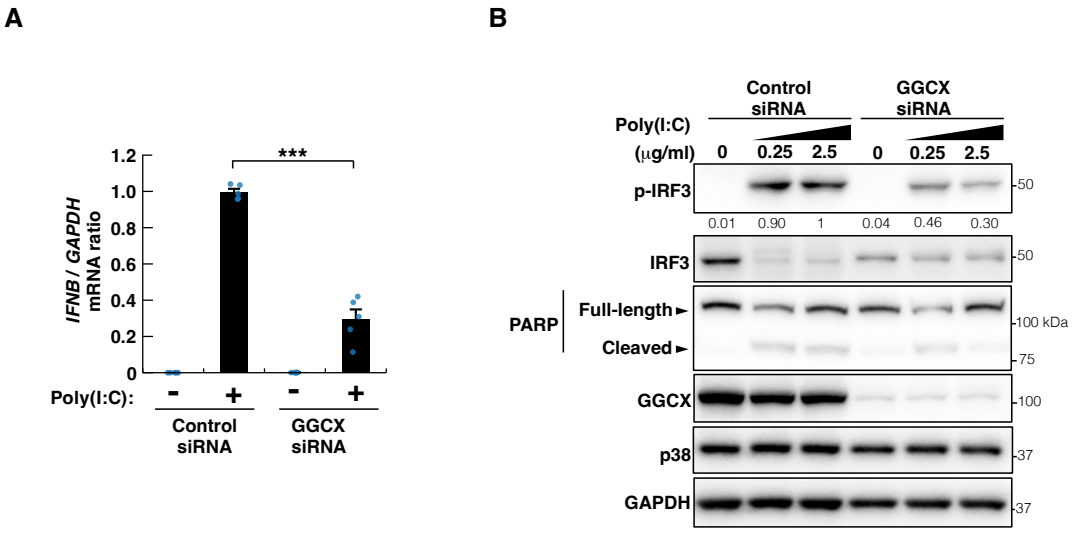

Fig. S18. The effects of GGCX RNAi on IFN-β induction in the presence of zVAD. A, **B**, HeLa S3 cells were transfected first with GGCX or control siRNAs for 4 days, then with poly(I:C) at 0.25 μg/ml (**A**) or 0.25 or 2.5 μg/ml (**B**) for 6 h in the presence of 50 μM zVAD-FMK. Cells were then subjected to RT-qPCR analysis of *IFNB1* mRNA (**A**) or to immunoblot analysis with antibodies against p-IRF3, IRF-3, PARP, GGCX, p38, and GAPDH. (**B**). Results in **A** are means ± SEM from five independent experiments, and those in **B** are representative of three independent experiments. Statistical analyses in (A) was performed using unpaired Student's *t* test (***$P < 0.005$). The signal intensities of p-IRF3 relative to IRF-3 were quantified and shown below the gels (normalized to lane 3).

Fig. S19.

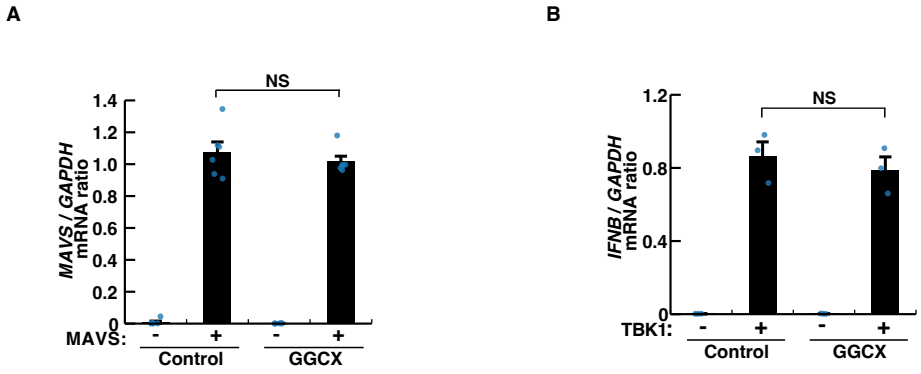

Fig. S19. GGCX overexpression promotes MAVS-induced but not TBK1-induced IFN-β gene expression. 293T cells were transiently transfected with expression plasmids for Myc-mGGCX and either Flag-hMAVS (**A**) or Flag-mTBK1 (**B**) for 20 h, then assayed for *MAVS* mRNA (**A**) or *IFNB1* mRNA (**B**) by RT-qPCR. Results are means ± SEM from five (A) or three (B) independent experiments. Statistical analyses in (A, B) were performed using unpaired Student's *t* test (NS< not significant).

Fig. S20

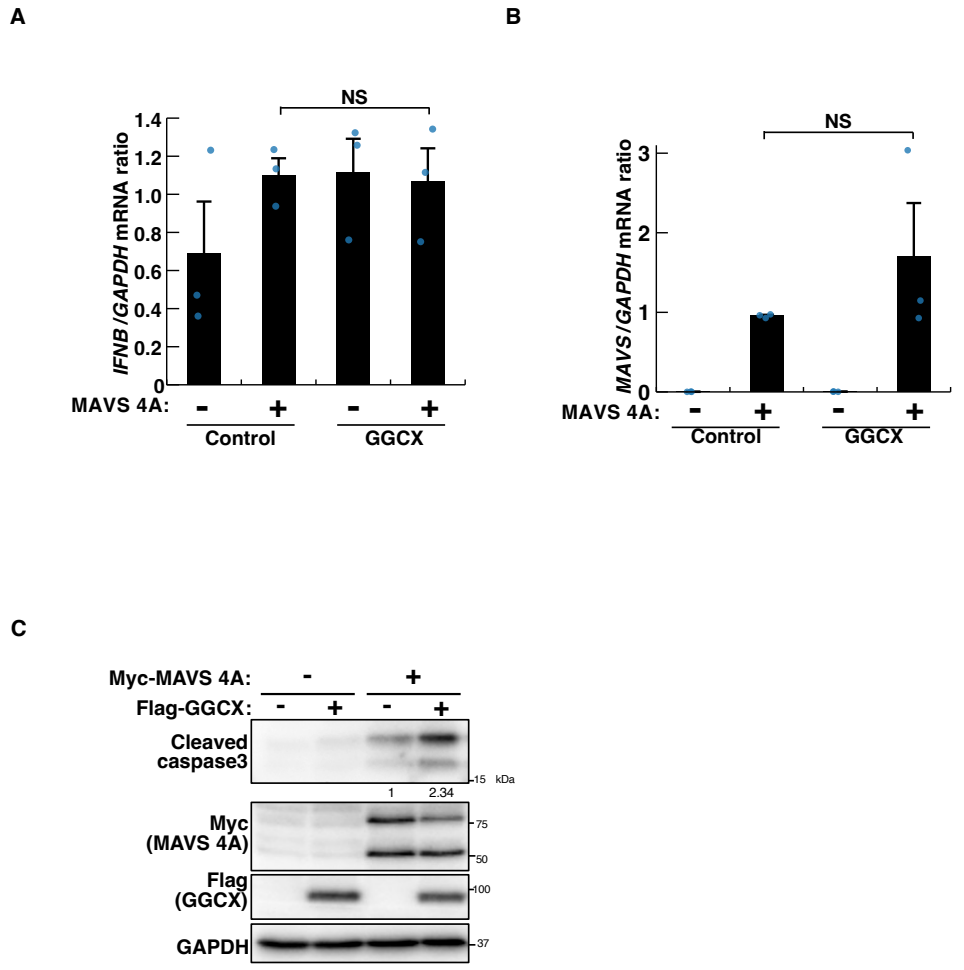

Fig. S20. GGCX overexpression does not overtly affect MAVS 4A-induced antiviral responses. A–C, 293T cells were transiently transfected with expression plasmids for Flag-mGGCX and myc-MAVS 4A for 20 h in the presence of 20 μM VK1, then assayed for *IFNB1* mRNA (**A**) or *MAVS* mRNA (**B**) by RT-qPCR or subjected to immunoblot analysis with antibodies against cleaved caspase-3, Flag, Myc, and GAPDH (**C**). Results in **A**, **B** are means ± SEM from three independent experiments and those in **C** are representative of three independent experiments. Statistical analyses in (A, B) were performed using unpaired Student's *t* test (NS, not significant). The signal intensities of cleaved caspase-3 relative to GAPDH were quantified and shown below the gels (normalized to lane 3).

Fig. S21.

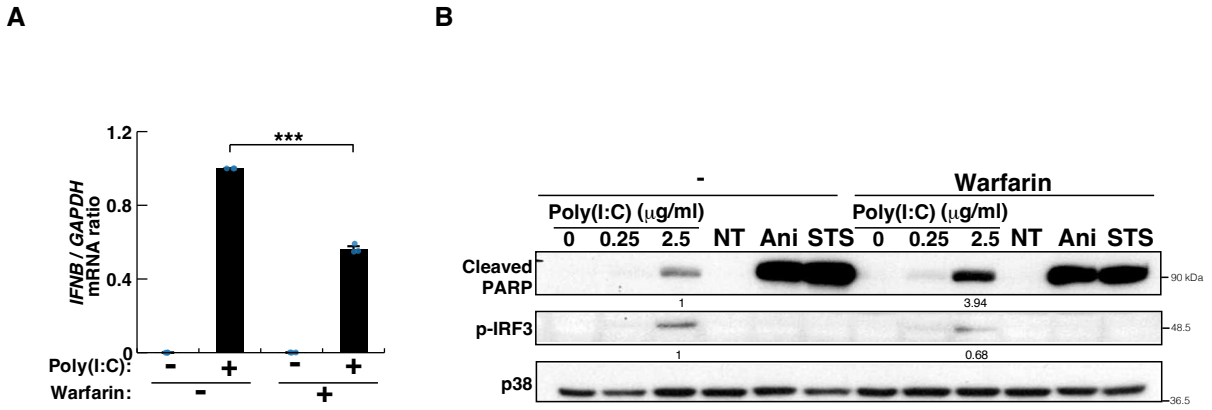

Fig. S21. Warfarin inhibits poly(I:C)-induced IFN-β induction but promotes caspase activation. HeLa S3 cells were incubated in the absence or presence of 100 μM warfarin for 48 h, transfected with poly(I:C) at 2.5 μg/ml (**A**) or 0.25 or 2.5 μg/ml (**B**) for 6 h in the continued absence or presence of warfarin, then either assayed for *IFNB1* mRNA by RT-qPCR (**A**) or subjected to immunoblot analysis with antibodies against cleaved PARP, p-IRF3, and p38 MAPK (**B**). As additional controls, instead of transfection with poly(I:C), cells were either not treated (NT) or were exposed for 6 h to anisomycin (Ani) at 10 μg/ml or to 1 μM staurosporine (STS) (**B**). Treatment with warfarin had no effect on caspase activation elicited by either of these latter two proapoptotic agents. Results in **A** are means ± SEM from three independent experiments, and those in **B** are representative of three independent experiments. Statistical analysis in (A) was performed using one sample *t* test (***$P < 0.005$). The signal intensities for p-IRF3 relative to p38 and cleaved PARP relative to p38 were quantified and shown below the gels (normalized to lane 3).

Fig. S22.

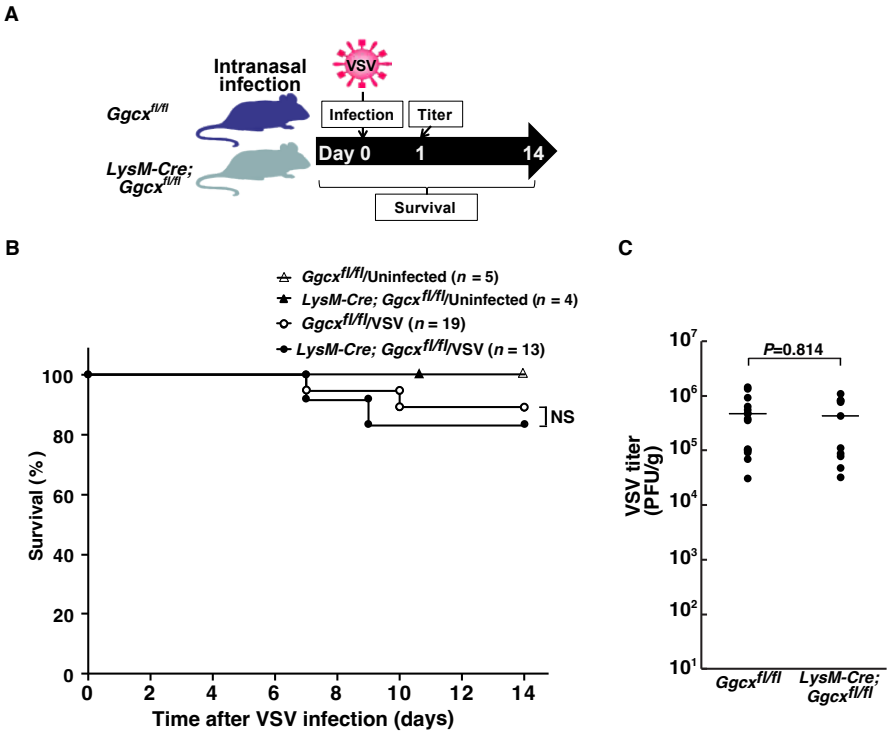

Fig. S22. Myeloid cell linage-specific ablation of GGCX has no significant effect on viral infection *in vivo*. **A**, Experiments shown in Figure 5**A–C** were repeated for mice with myeloid cell lineage-specific ablation of GGCX (*LyzM-Cre;Ggcx*$^{fl/fl}$ mice) and control (*Ggcx*$^{fl/fl}$) mice. Results are for the indicated numbers of animals from four independent experiments in **B** and for 10 (*LyzM-Cre;Ggcx*$^{fl/fl}$) and 15 (*Ggcx*$^{fl/fl}$) mice, respectively, from four independent experiments in **C**. No significant difference was apparent between the two survival curves of mice after VSV infection (log-rank test). For viral titer, the *P* value was determined with the unpaired Student's *t* test.

Fig. S23.

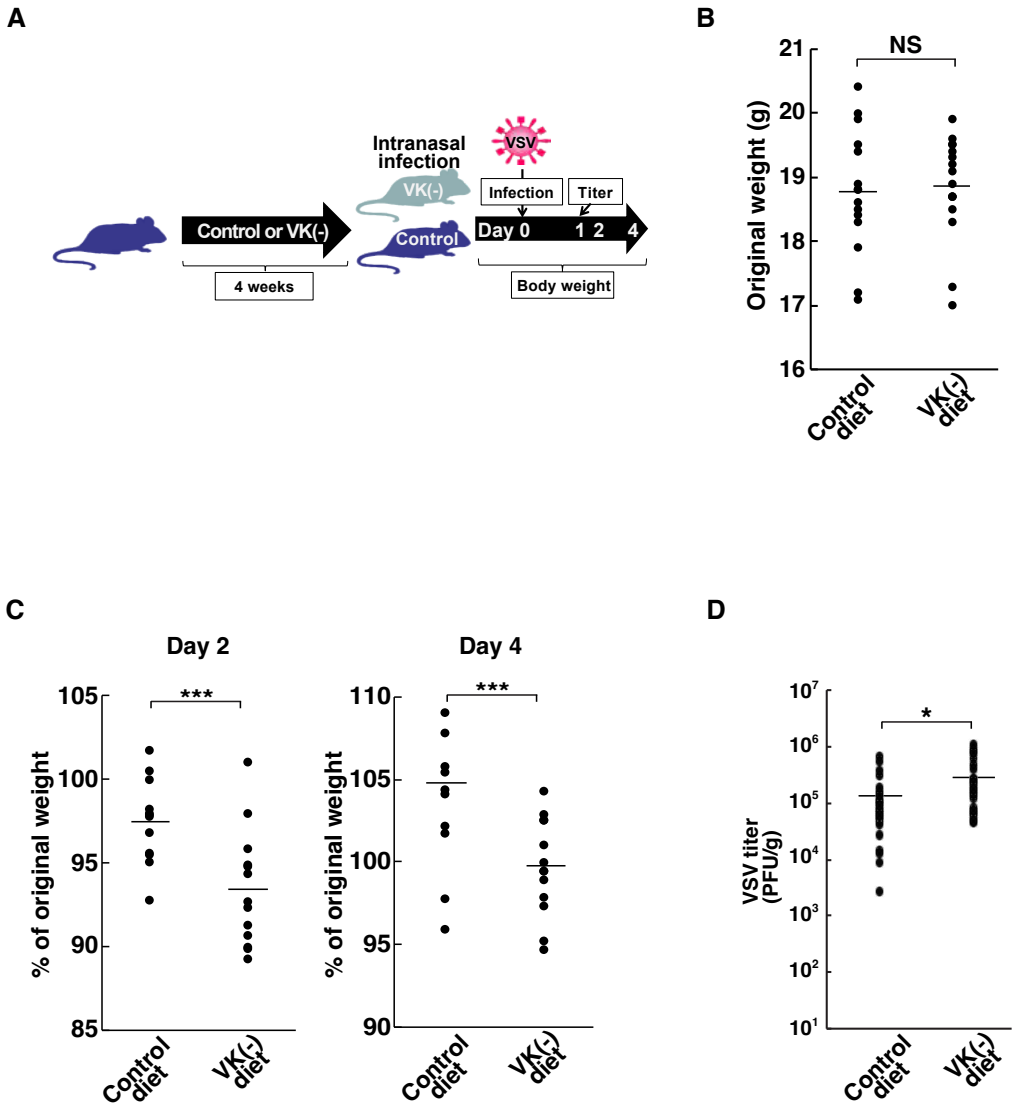

Fig. S23. VK protects against viral infection *in vivo*. Age- and sex-matched WT mice fed a normal or VK-deficient diet and provided with cefotiam hydrochloride (15 mg/l) in drinking water for 4 weeks were infected intranasally with VSV (1×10^7 PFU) (**A**). Bodyweight of mice was measured 1 day before infection (**B**) and 2 and 4 days after infection (**C**). Results are shown for 12 and 13 mice fed the control or VK-deficient diet, respectively. The viral titer in the brain at 1 day after infection was also determined (**D**); results are for 26 and 27 mice fed the control or VK-deficient diet, respectively, from three independent experiments. Statistical analyses in (B-D) were performed using unpaired Student's *t* test (*$P < 0.05$, ***$P < 0.005$, NS< not significant).

Fig. S24.

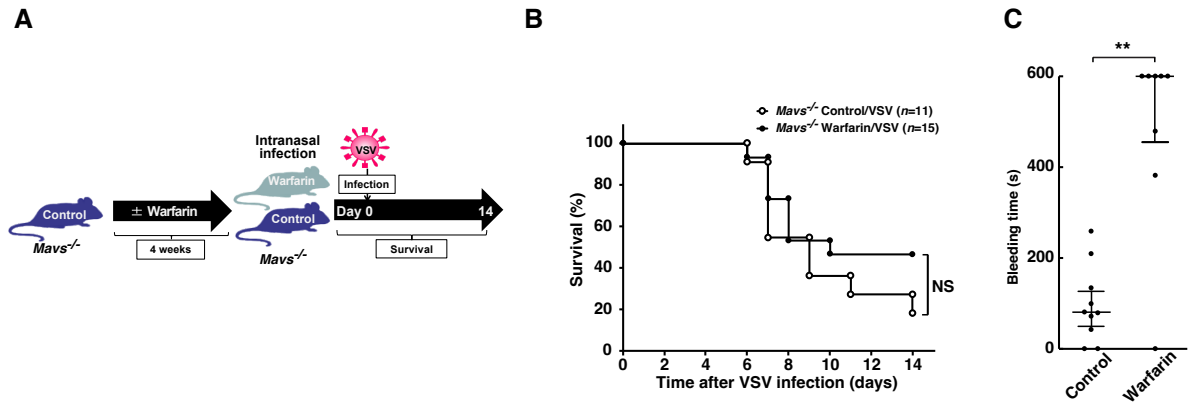

Fig. S24. Warfarin does not exacerbate viral infection in MAVS KO mice. Age- and sex-matched MAVS KO mouse littermates were treated with warfarin (0.96 mg/l) or vehicle (ethanol) in drinking water for 4 weeks, after which female mice were infected intranasally with VSV (**A**) then monitored for survival daily for 14 days (n = 15 and 11 mice for warfarin and vehicle, respectively, from three independent experiments) (**B**). Bleeding time in male mice was also monitored by tail bleeding assay to confirm the effectiveness of warfarin with regard to inhibition of GGCX-dependent coagulation activity (**C**). Results for individual mice as well as the median and interquartile range are shown (n = 8 and 10 mice for warfarin and vehicle, respectively, from three independent experiments). Statistical analyses in (B) were performed using log-rank test (NS, not significant), and (C) were performed using Mann-Whitney U test (**$P < 0.01$).

Fig. S25.

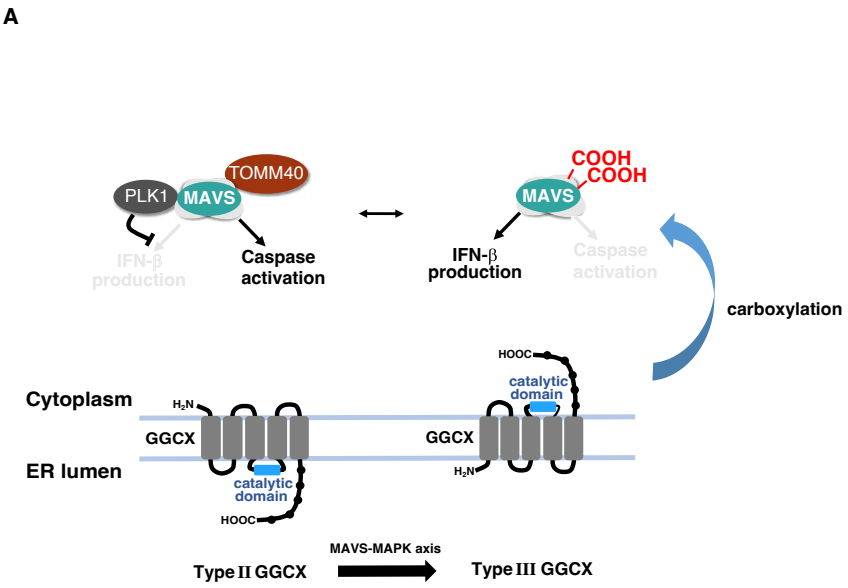

Fig. S25. Schematic overview of GGCX topology inversion and MAVS carboxylation. See the main text for details.

Fig. S26.

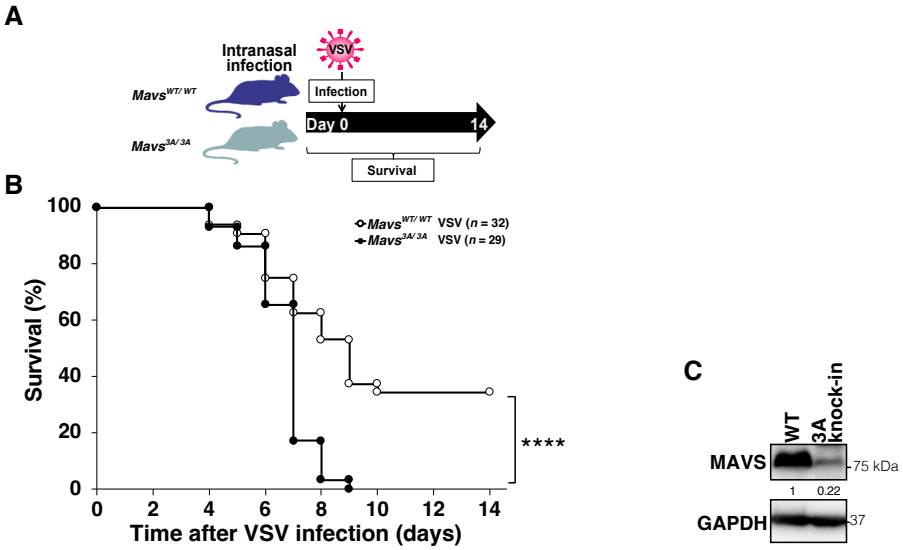

Fig. S26. The susceptibility of MAVS 3A knock-in mice to VSV infection. A,**B**, Age-matched mice with MAVS 3A mutation (*MAVS*$^{3A/3A}$ mice) and control (*MAVS*$^{WT/WT}$) mice were infected intranasally with VSV (1×10^4 PFU) (**A**) and monitored for survival daily for 14 days, with data being shown for the indicated numbers of animals from three independent experiments (**B**). ****$P < 0.0001$ (log-rank test). **C,** The olfactory bulb of mice was subjected to immunoblot analysis with antibodies to MAVS and to GAPDH. Similar results were obtained from three independent mice**.** The signal intensities for MAVS relative to GAPDH were quantified and shown below the gels (normalized to lane 1).

Fig. S27.

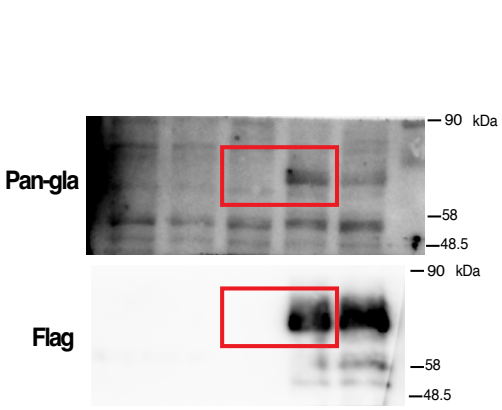

Fig. S27.
A. These are uncropped blots corresponding to Fig. 1B.

Fig. S28.

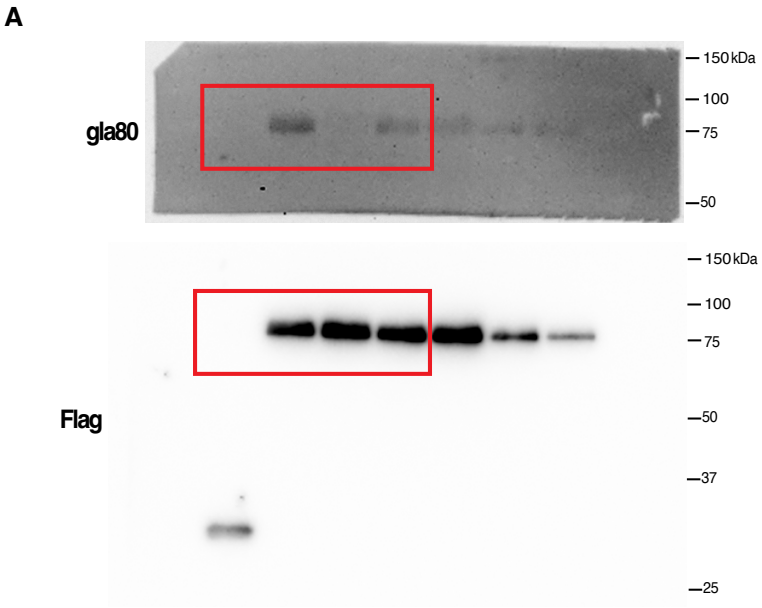

Fig. S28.
A. These are uncropped blots corresponding to Fig. 1C.

Fig. S29.

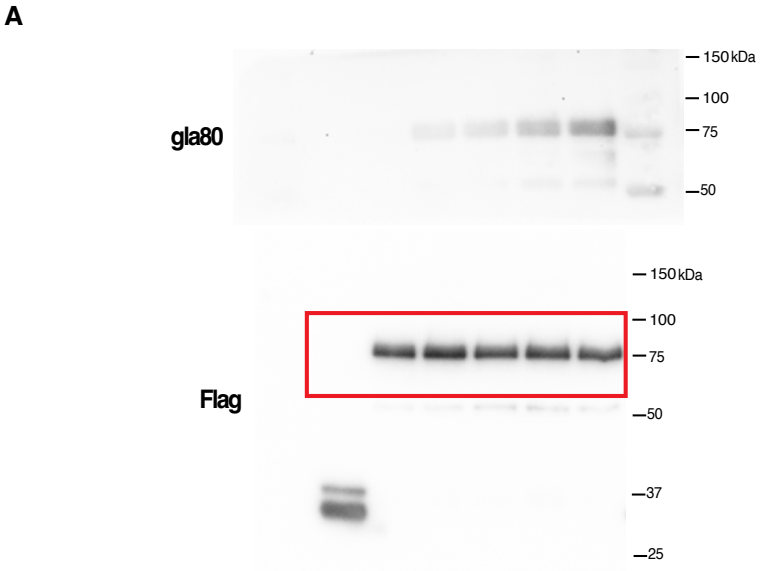

Fig. S29.
A. These are uncropped blots corresponding to Fig. 1D.

Fig. S30.

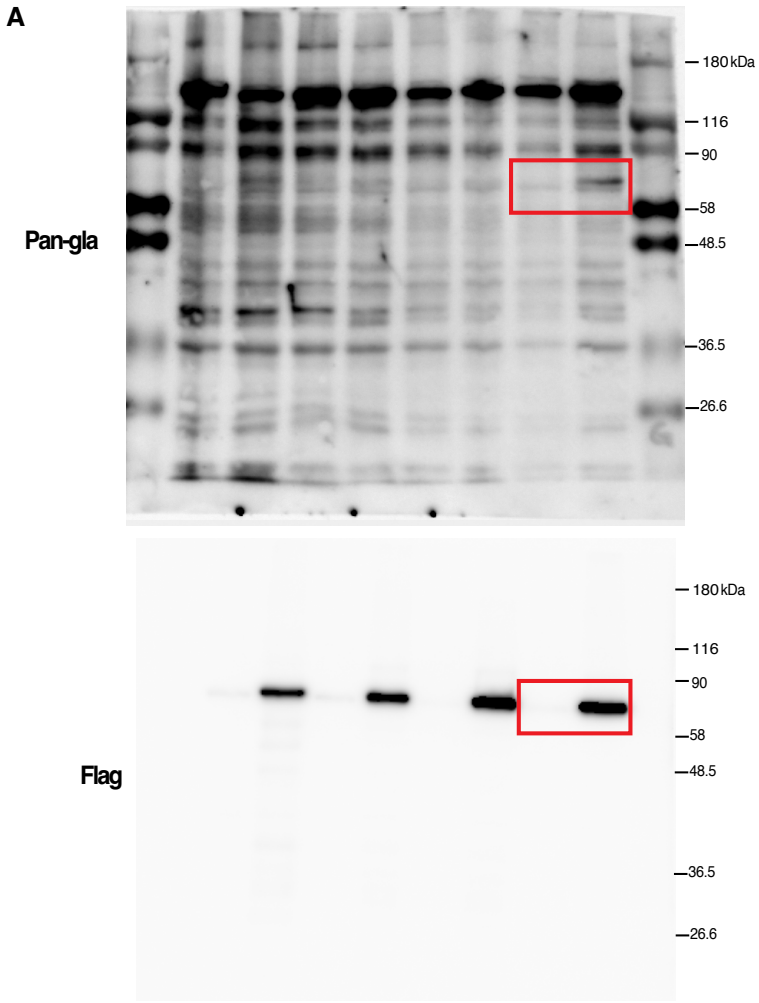

Fig. S30.
A. These are uncropped blots corresponding to Fig. 1E.

Fig. S31.

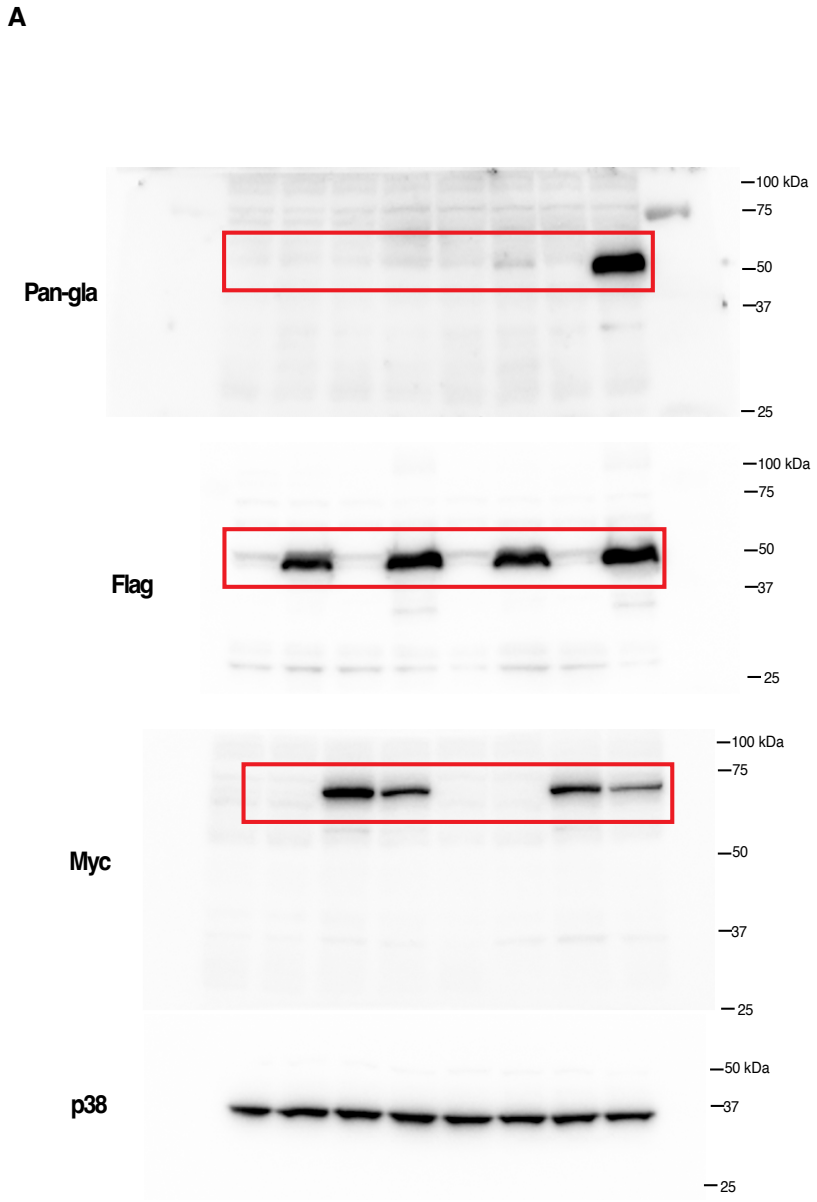

Fig. S31.
A. These are uncropped blots corresponding to Fig. 1F.

Fig. S32.

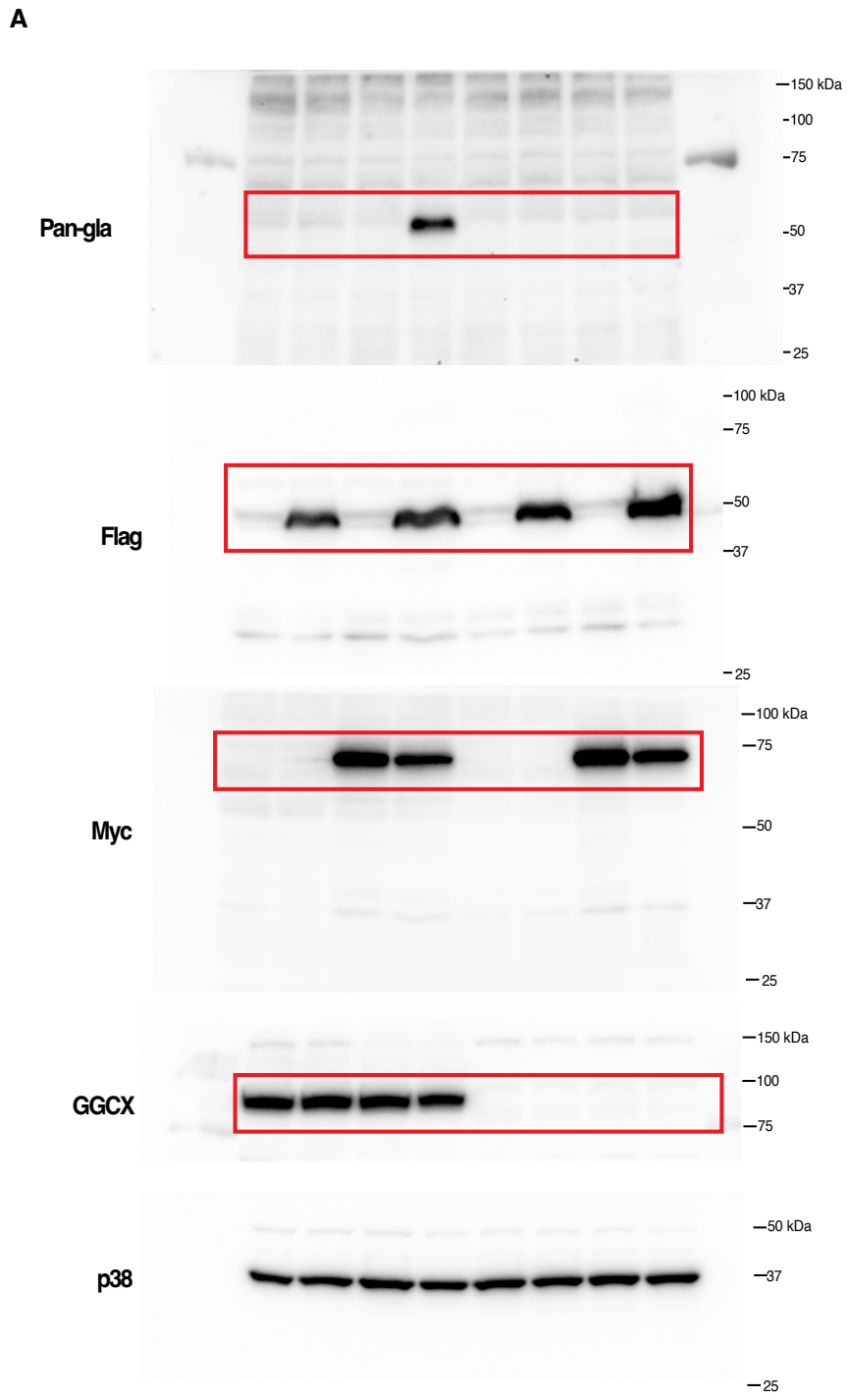

Fig. S32.
A. These are uncropped blots corresponding to Fig. 1G.

Fig. S33.

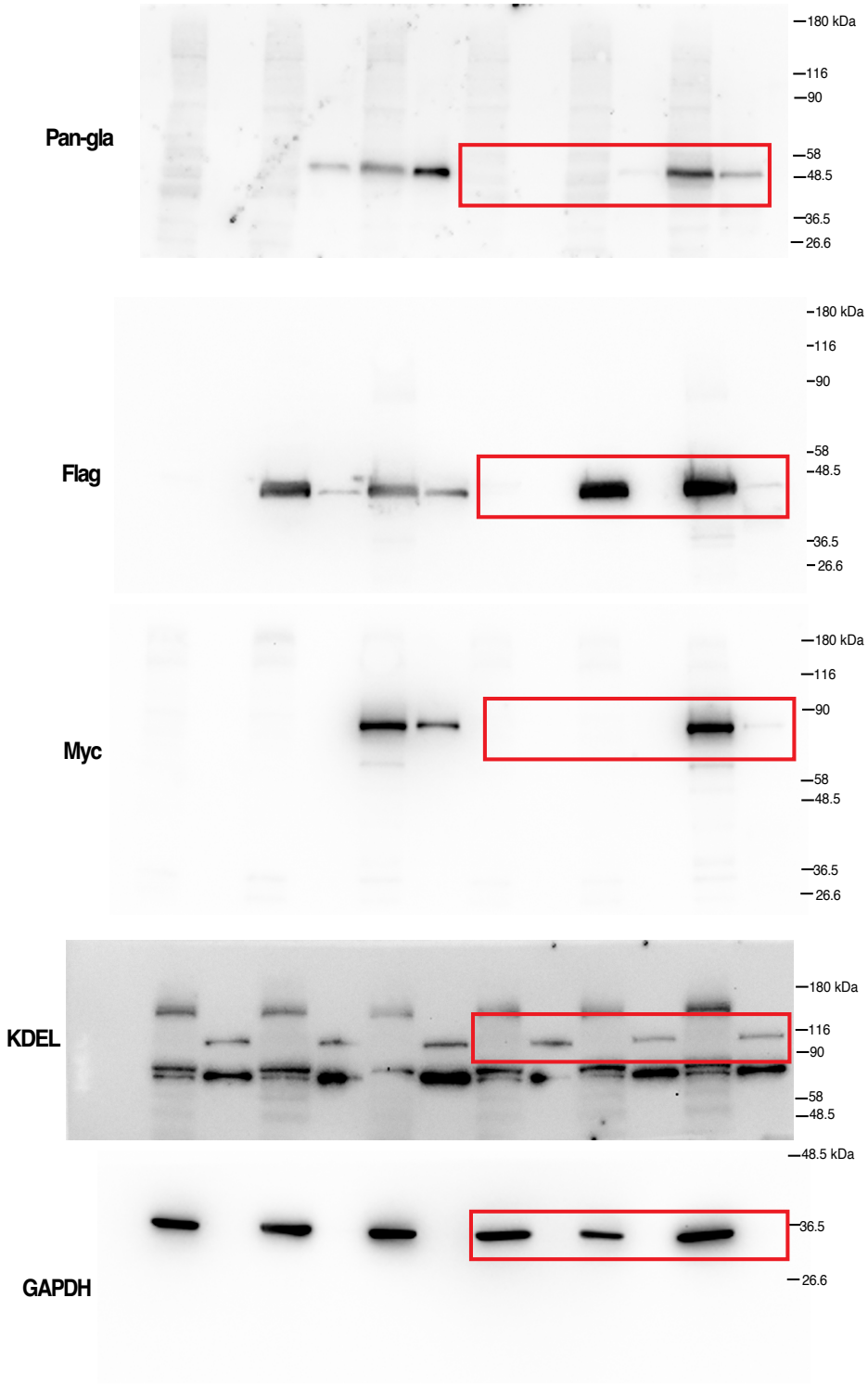

Fig. S33.
A. These are uncropped blots corresponding to Fig. 1H.

Fig. S34.

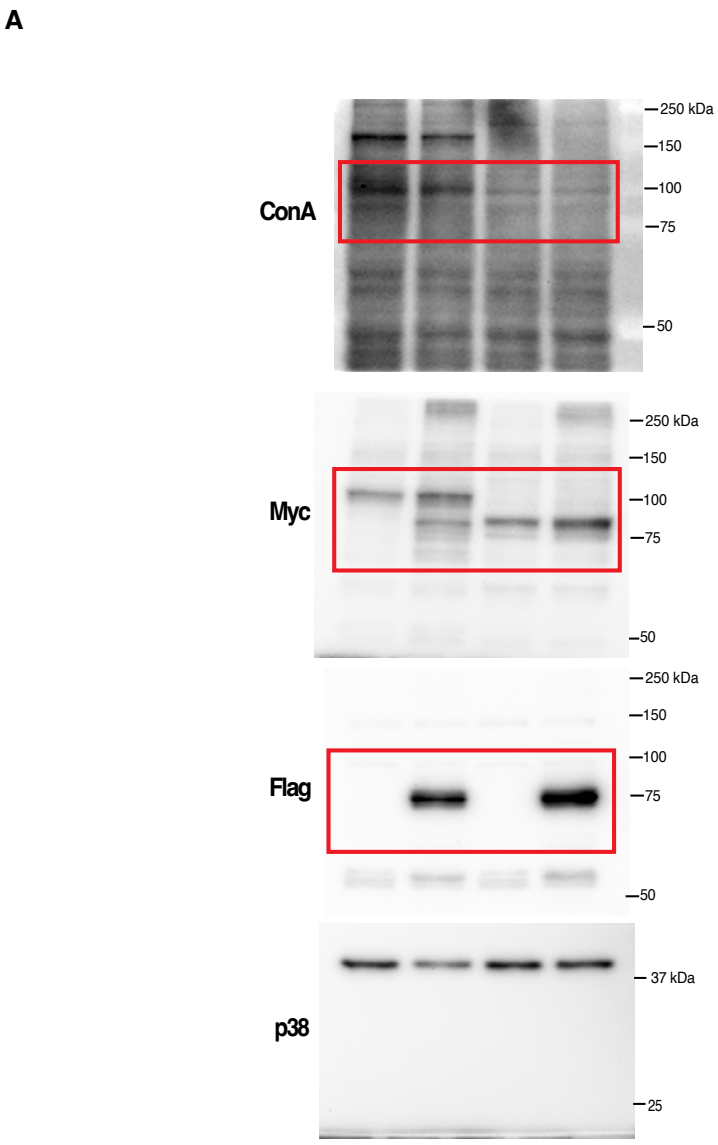

Fig. S34.
A. These are uncropped blots corresponding to Fig. 2B.

Fig. S35.

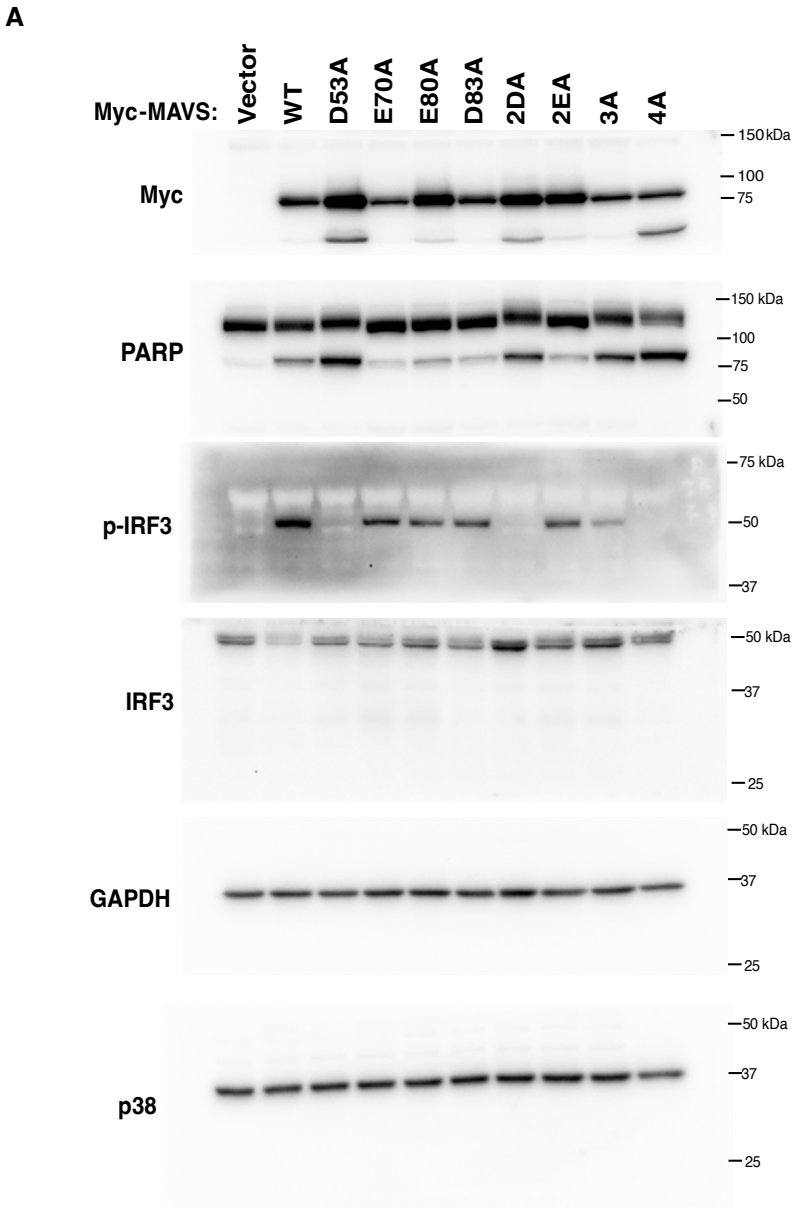

Fig. S35.
A. These are uncropped blots corresponding to Fig. 3B.

Fig. S36.

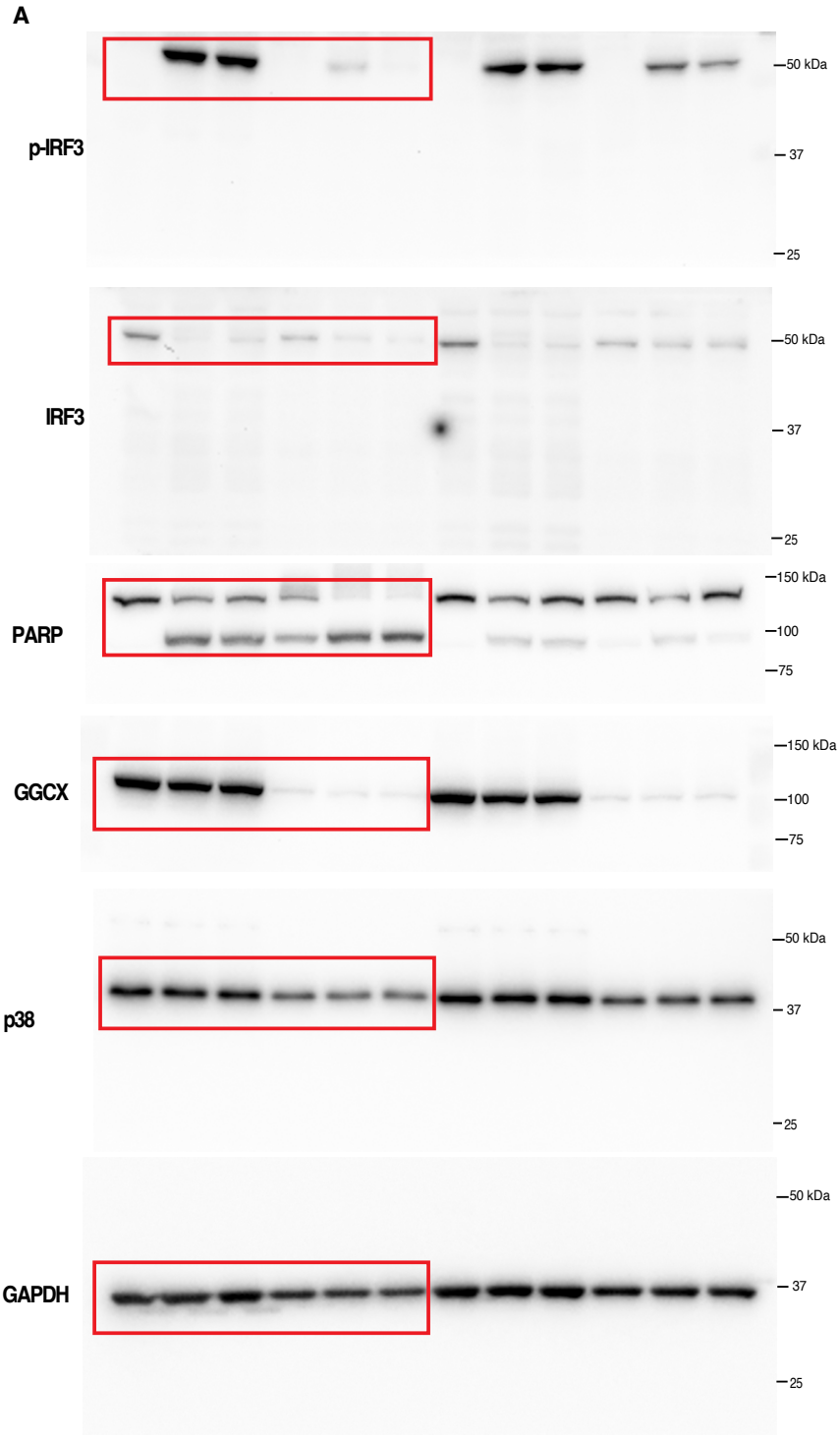

Fig. S36.
A. These are uncropped blots corresponding to Fig. 3G. Most of the blots shown here were derived from regions of the same gel used for Fig. S64, while one blot (p38) was from an independent gel. Samples without zVAD treatment (this figure) and with zVAD treatment were run in parallel and developed together on the same membrane.

Fig. S37.

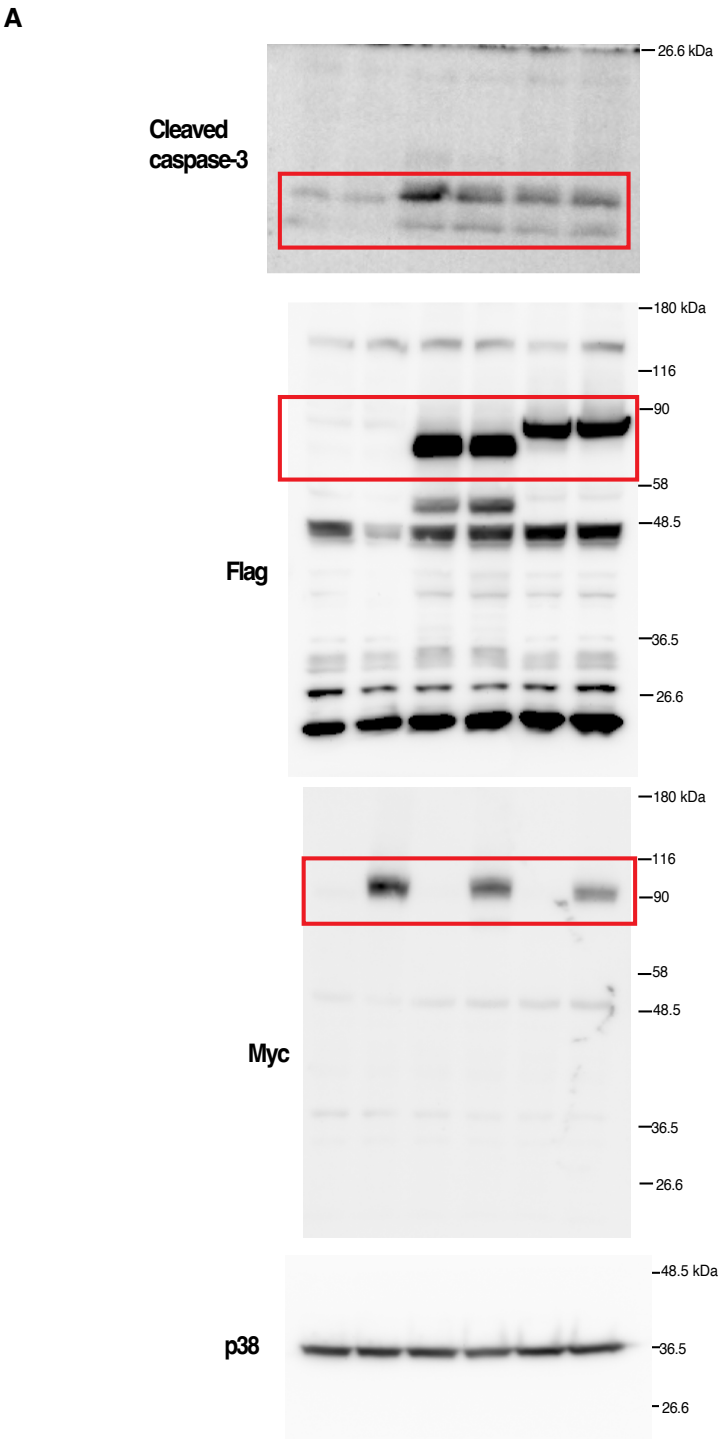

Fig. S37.
A. These are uncropped blots corresponding to Fig. 3I.

Fig. S38.

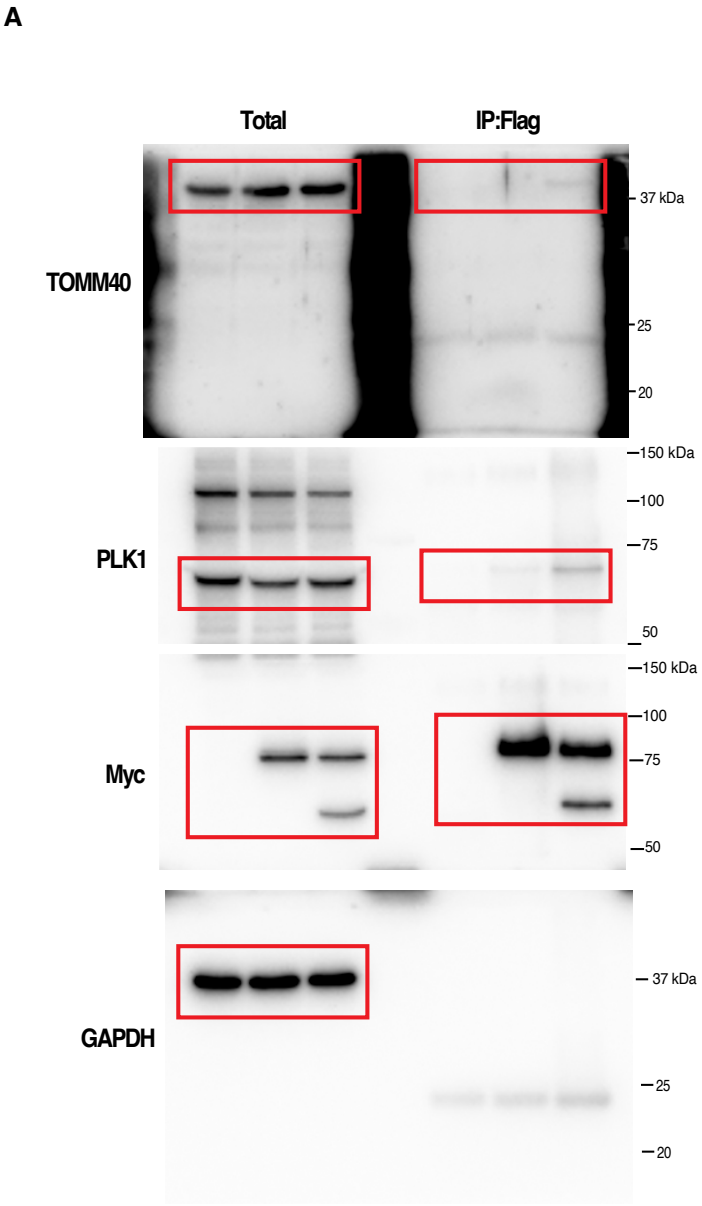

Fig. S38.
A. These are uncropped blots corresponding to Fig. 4B.

Fig. S39.

A

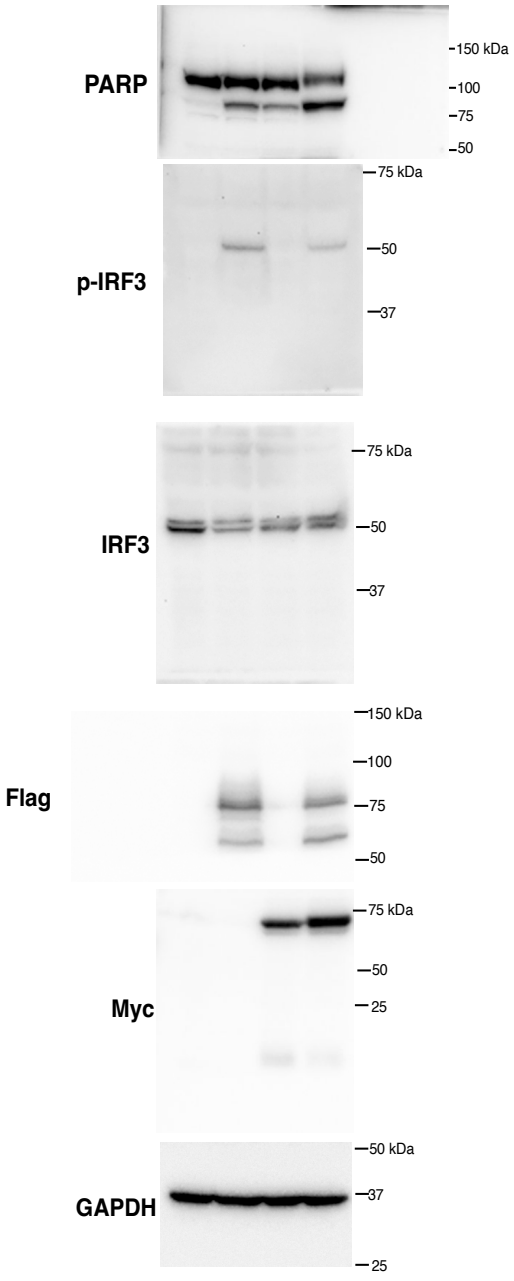

Fig. S39.
A. These are uncropped blots corresponding to Fig. 4C.

Fig. S40.

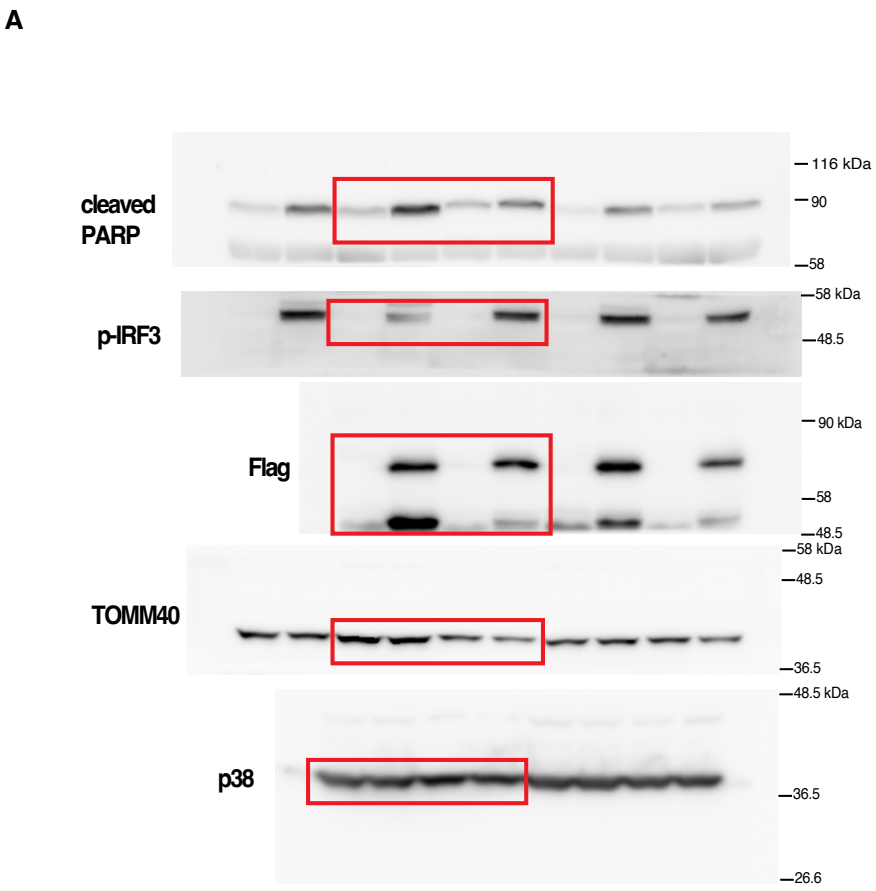

Fig. S40.
A. These are uncropped blots corresponding to Fig. 4E.

Fig. S41.

A

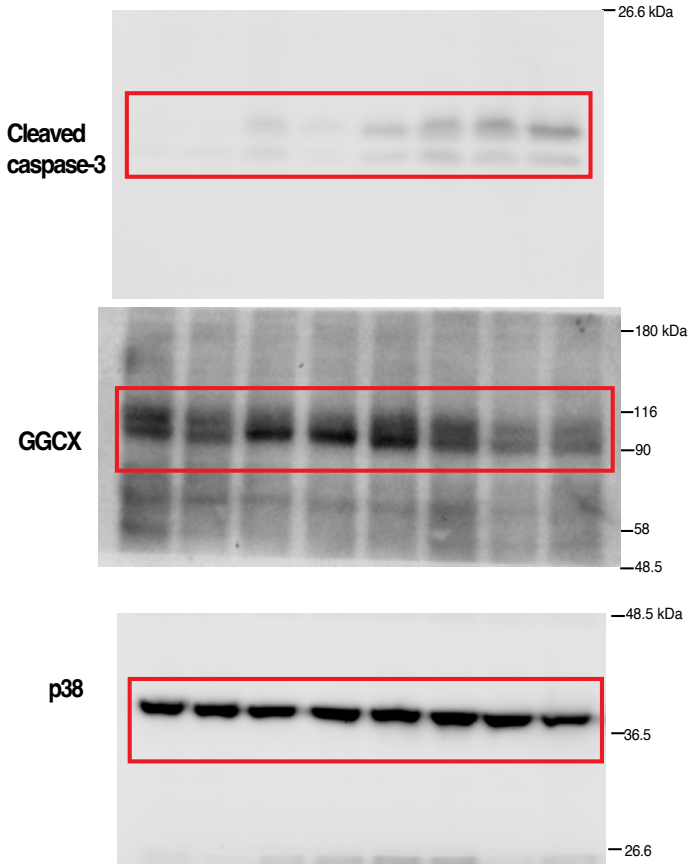

Fig. S41.
A. These are uncropped blots corresponding to Fig. 5E.

Fig. S42.

Fig. S42.
A. This is an uncropped gel corresponding to Fig. S1B.

Fig. S43.

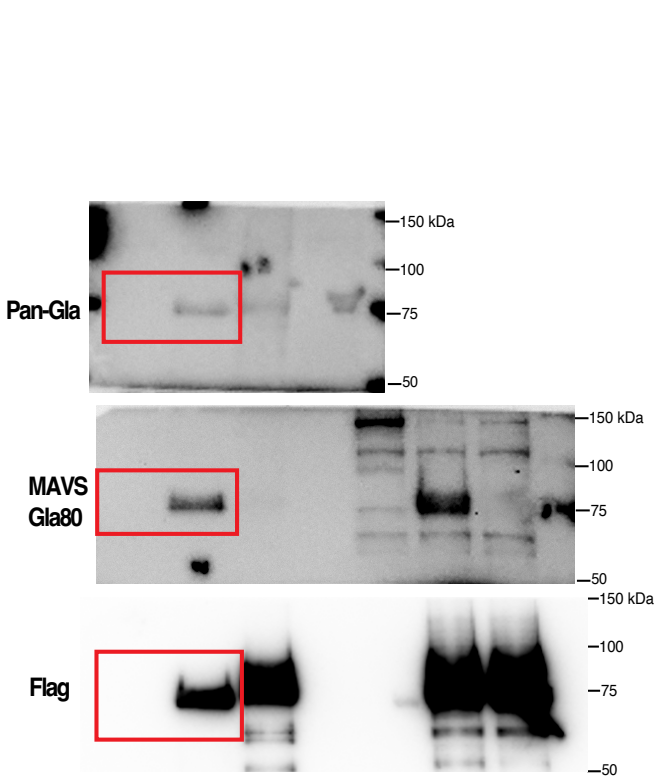

Fig. S43.
A. These are uncropped blots corresponding to Fig. S3A.

Fig. S44.

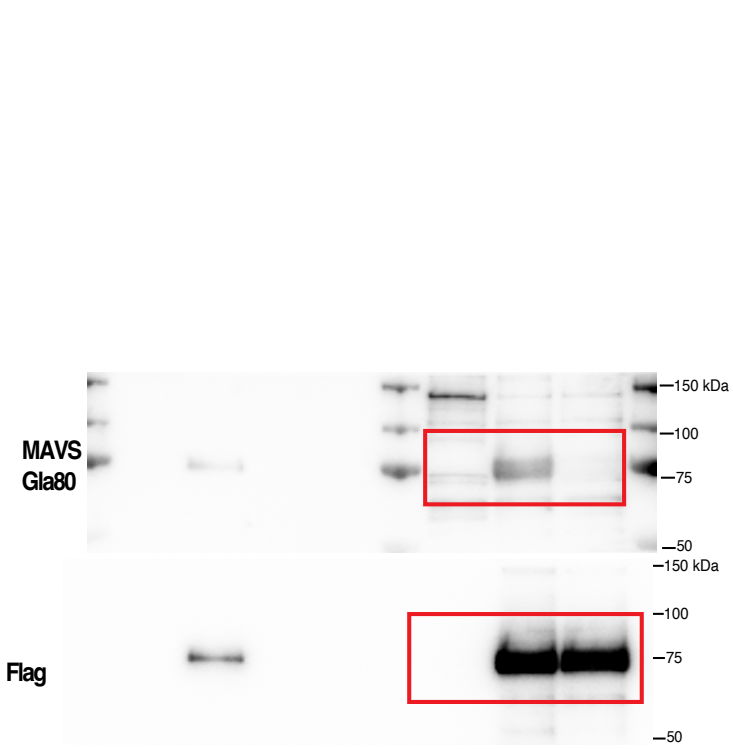

Fig. S44.
A. These are uncropped blots corresponding to Fig. S3B.

Fig. S45.

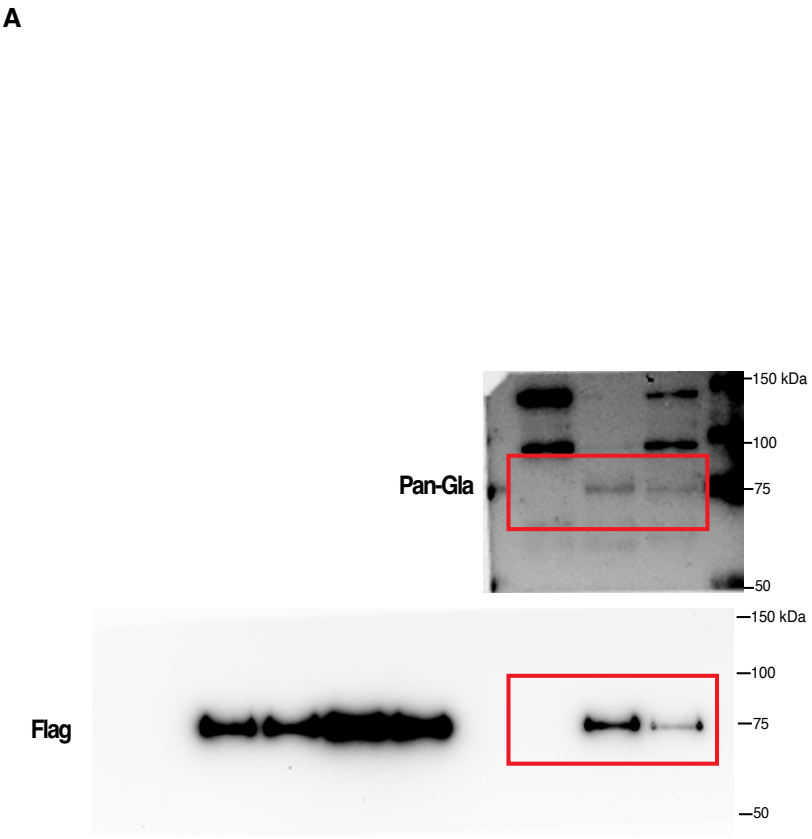

Fig. S45.
A. These are uncropped blots corresponding to Fig. S3C.

Fig. S46.

A

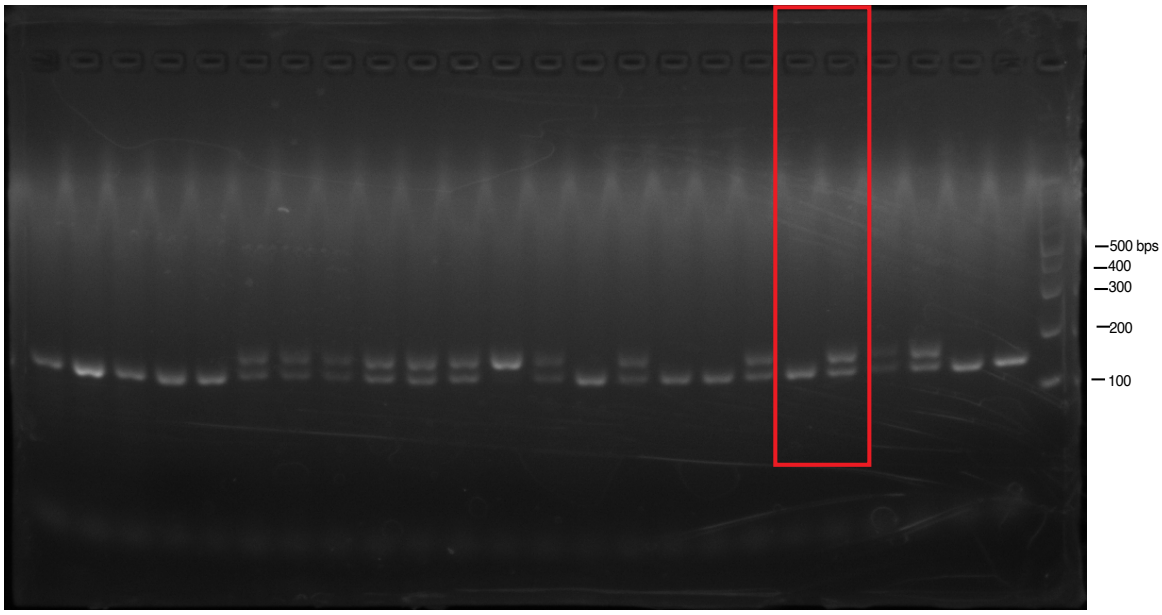

Fig. S46.
A. This is an uncropped gel corresponding to Fig. S5B.

Fig. S47.

A

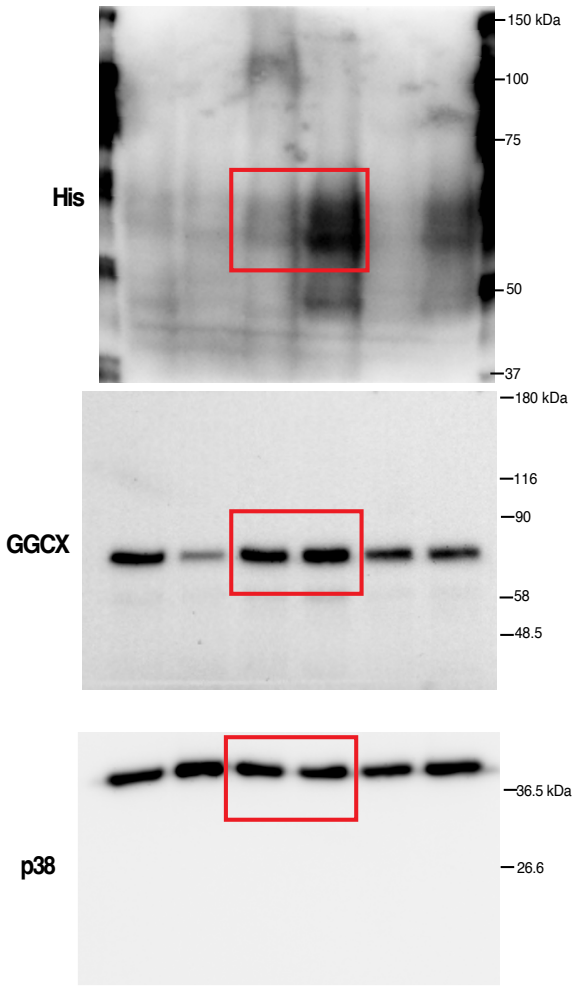

Fig. S47.
A. These are uncropped blots corresponding to Fig. S5C.

Fig. S48.

A

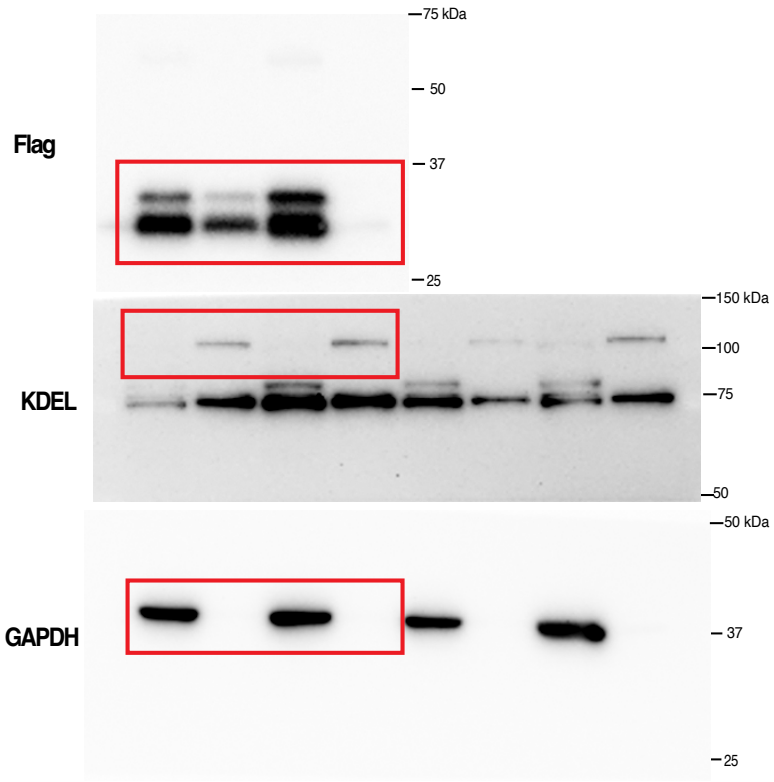

Fig. S48.
A. These are uncropped blots corresponding to Fig. S6B.

Fig. S49.

A

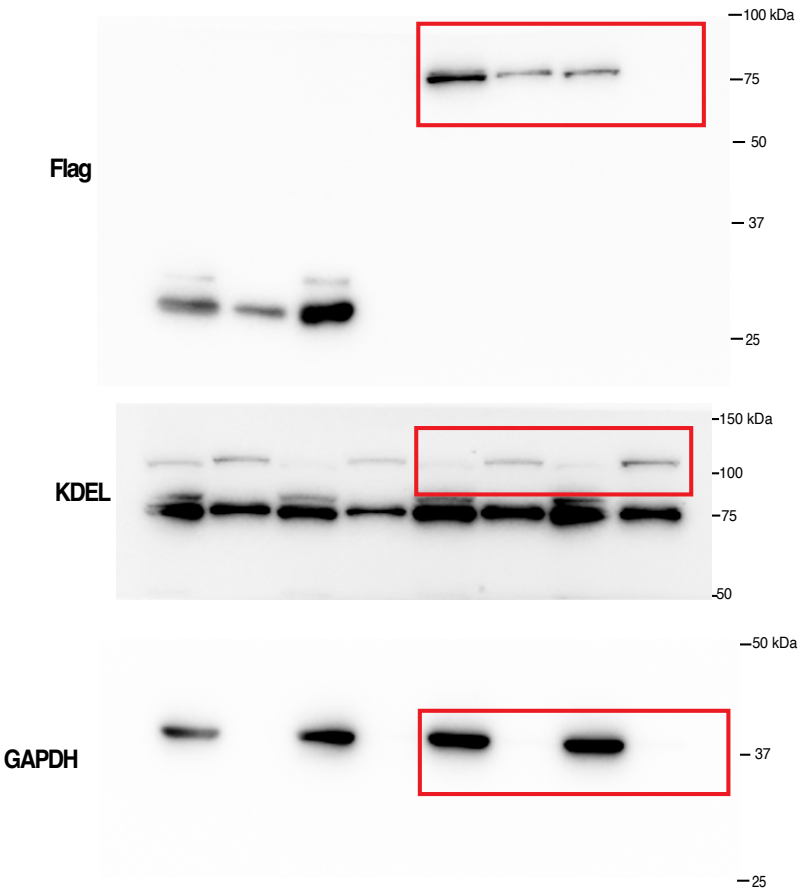

Fig. S49.
A. These are uncropped blots corresponding to Fig. S6C.

Fig. S50.

A

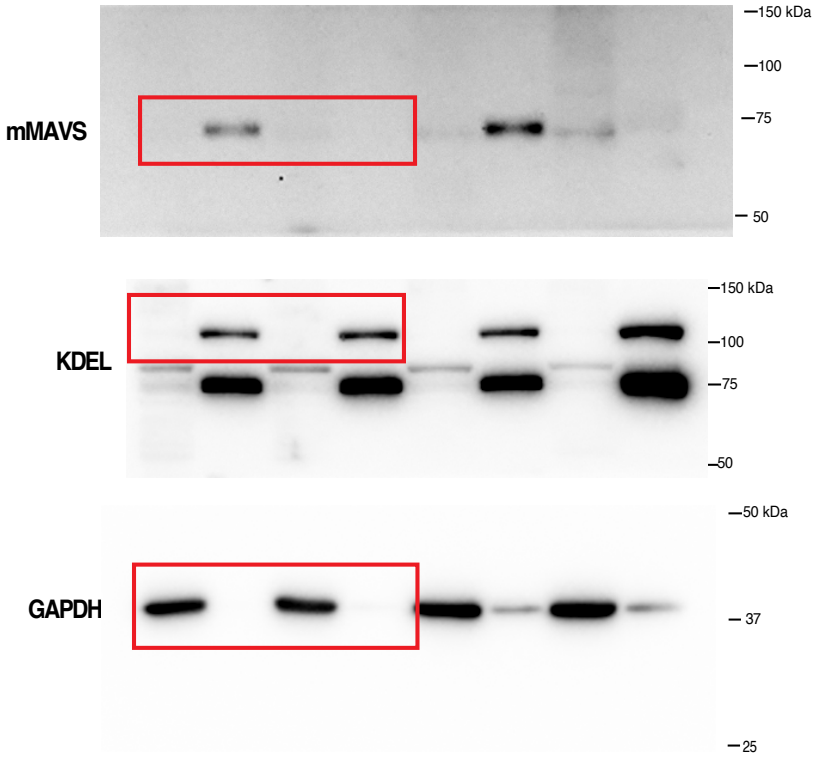

Fig. S50.
A. These are uncropped blots corresponding to Fig. S6D.

Fig. S51.

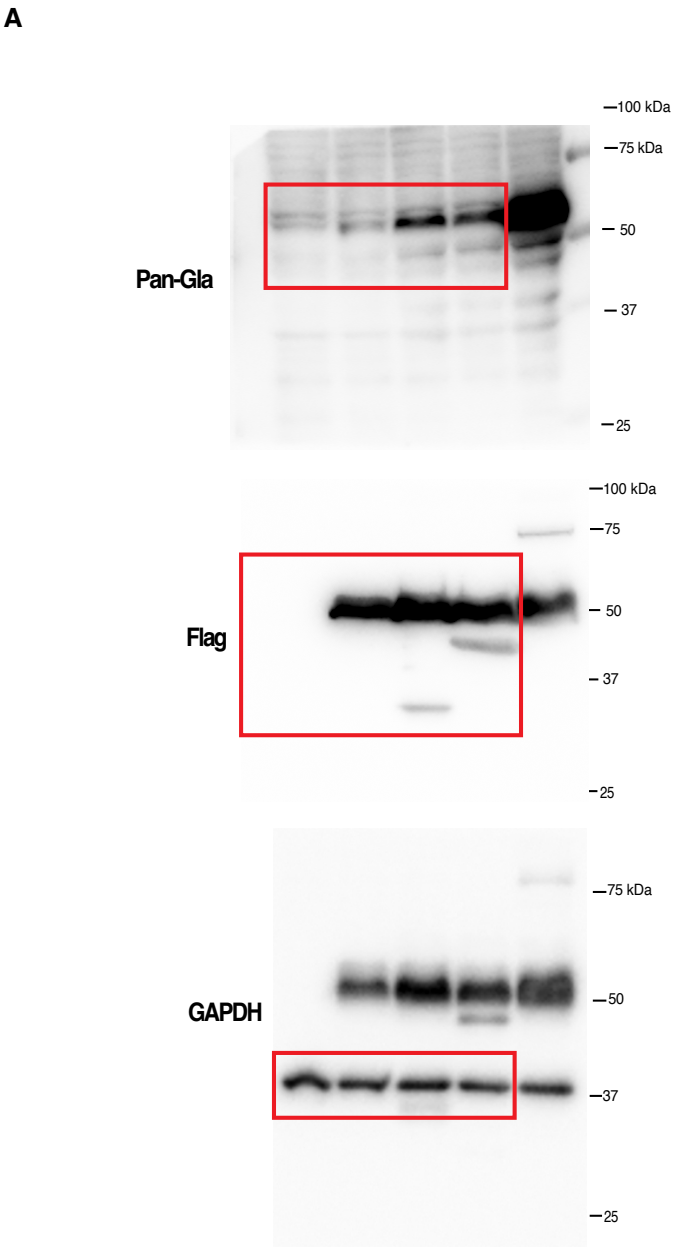

Fig. S51.
A. These are uncropped blots corresponding to Fig. S8A.

Fig. S52.

A

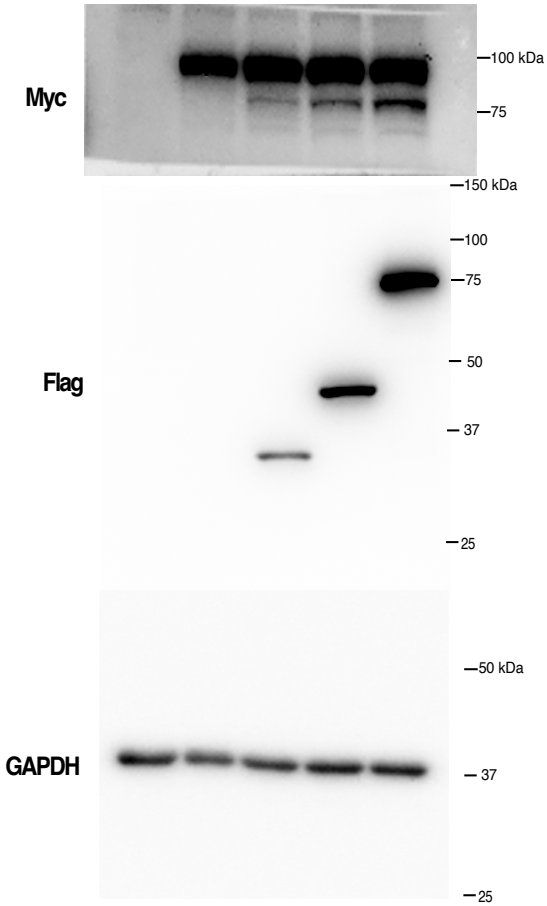

Fig. S52.
A. These are uncropped blots corresponding to Fig. S8B.

Fig. S53.

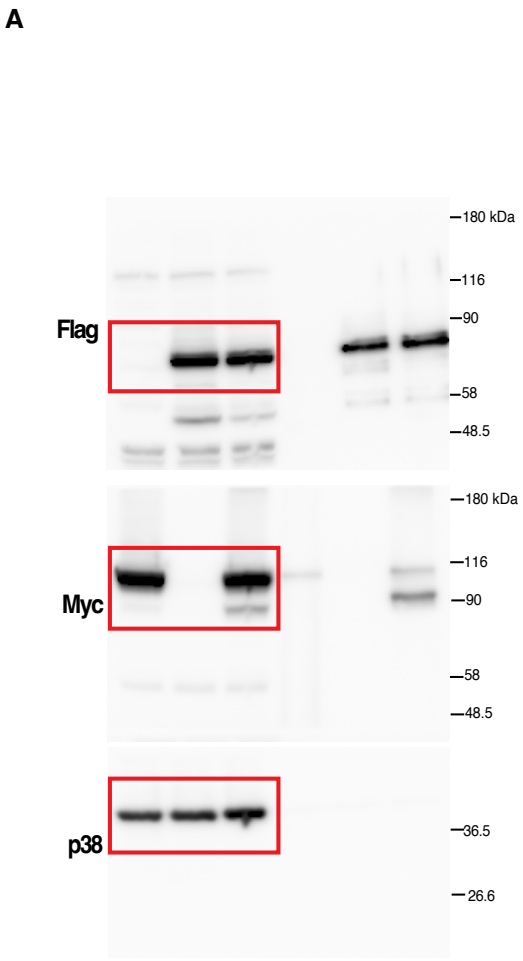

Fig. S53.
A. These are uncropped blots corresponding to Fig. S9A.

Fig. S54.

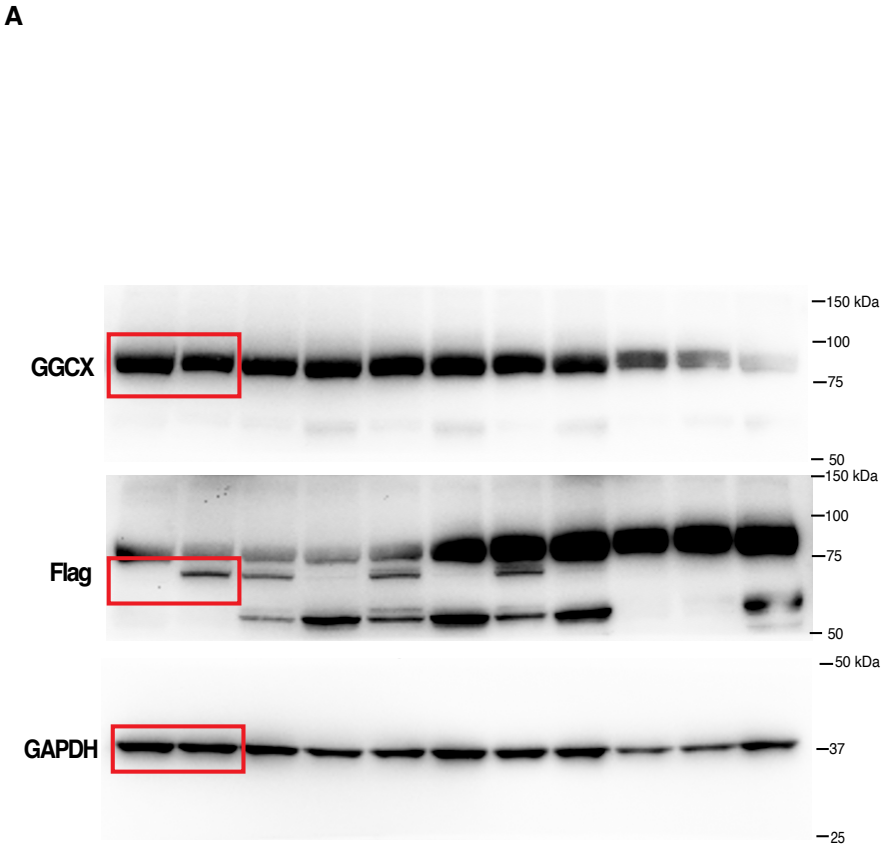

Fig. S54.
A. These are uncropped blots corresponding to Fig. S9B.

Fig. S55.

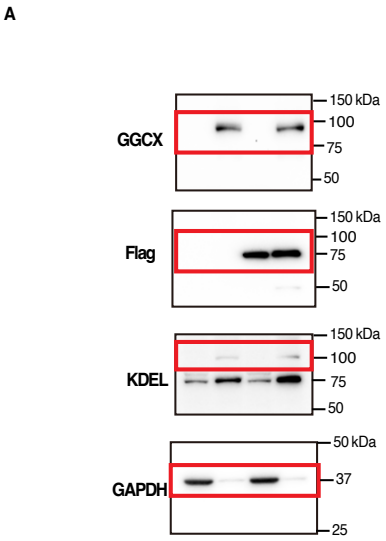

Fig. S55.
A. These are uncropped blots corresponding to Fig. S9C.

Fig. S56.

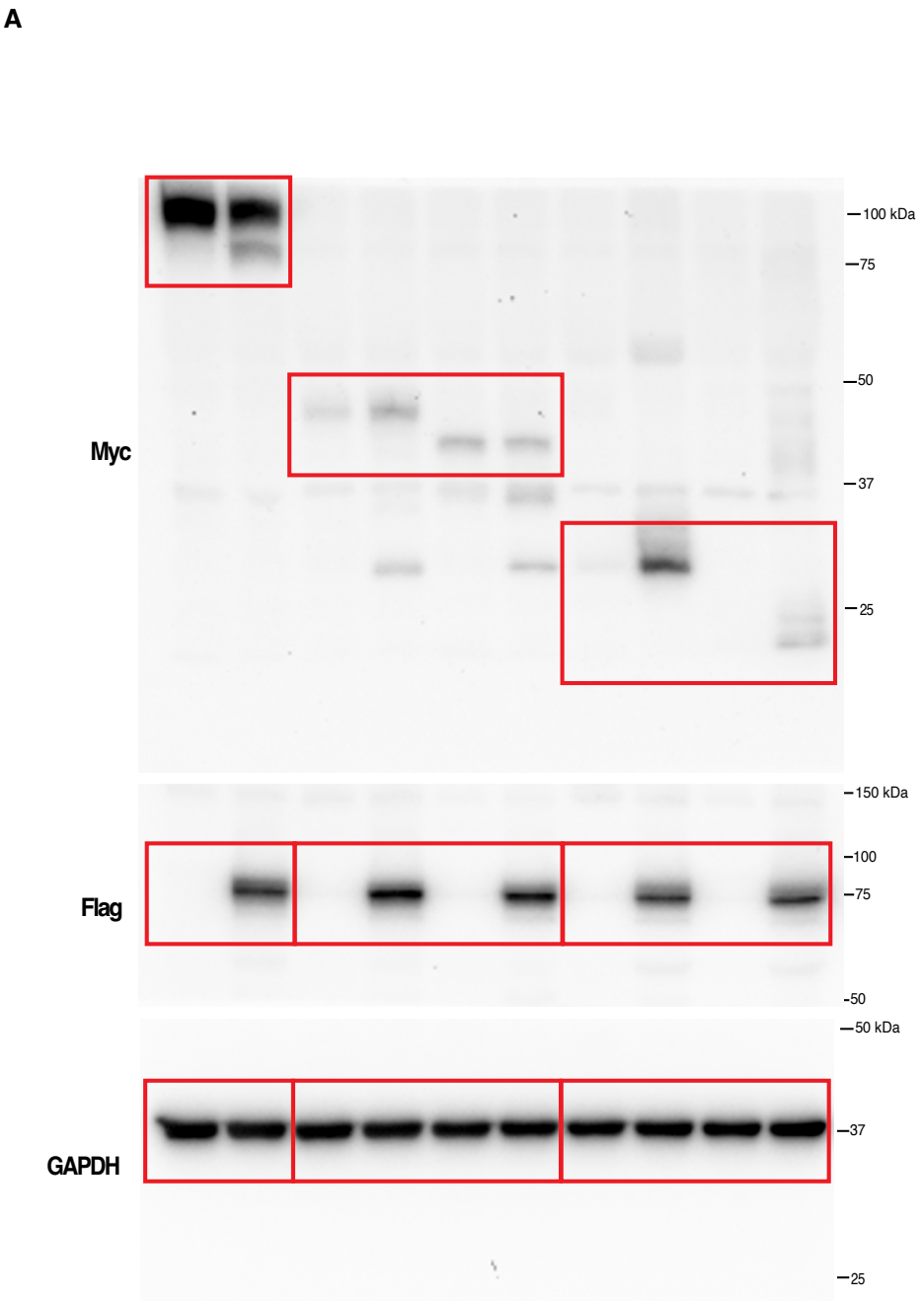

Fig. S56.
A. These are uncropped blots corresponding to Fig. S10A-C.

Fig. S57.

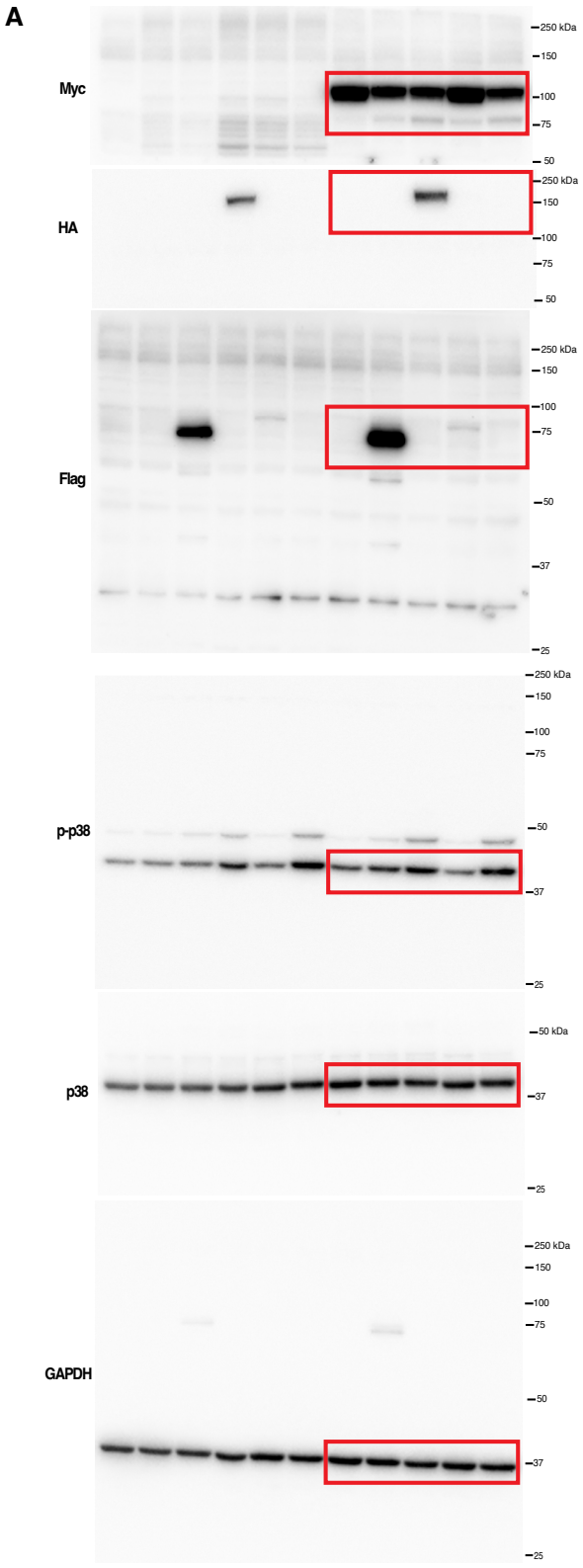

Fig. S57.
A. These are uncropped blots corresponding to Fig. S11A.

Fig. S58.

A

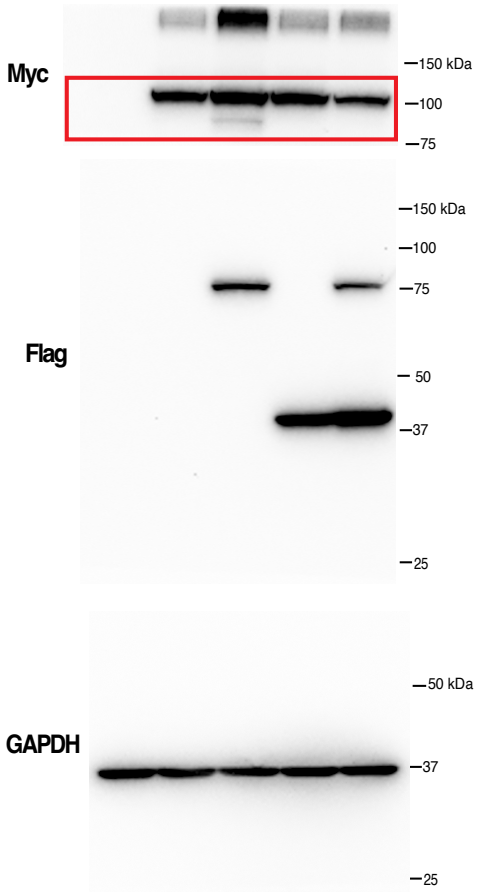

Fig. S58.
A. These are uncropped blots corresponding to Fig. S11B.

Fig. S59.

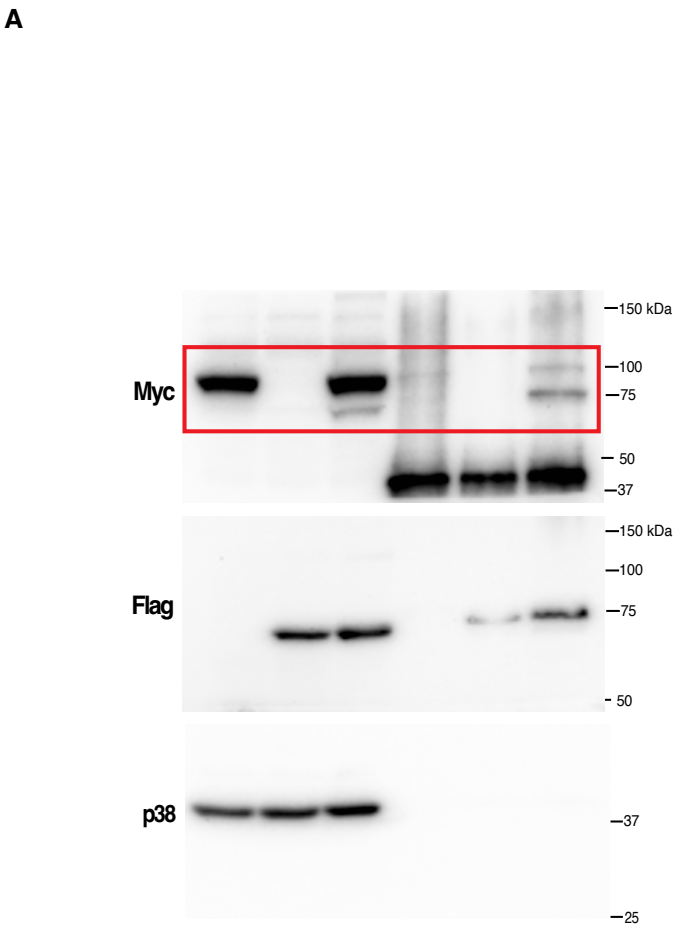

Fig. S59.
A. These are uncropped blots corresponding to Fig. S12A.

Fig. S60.

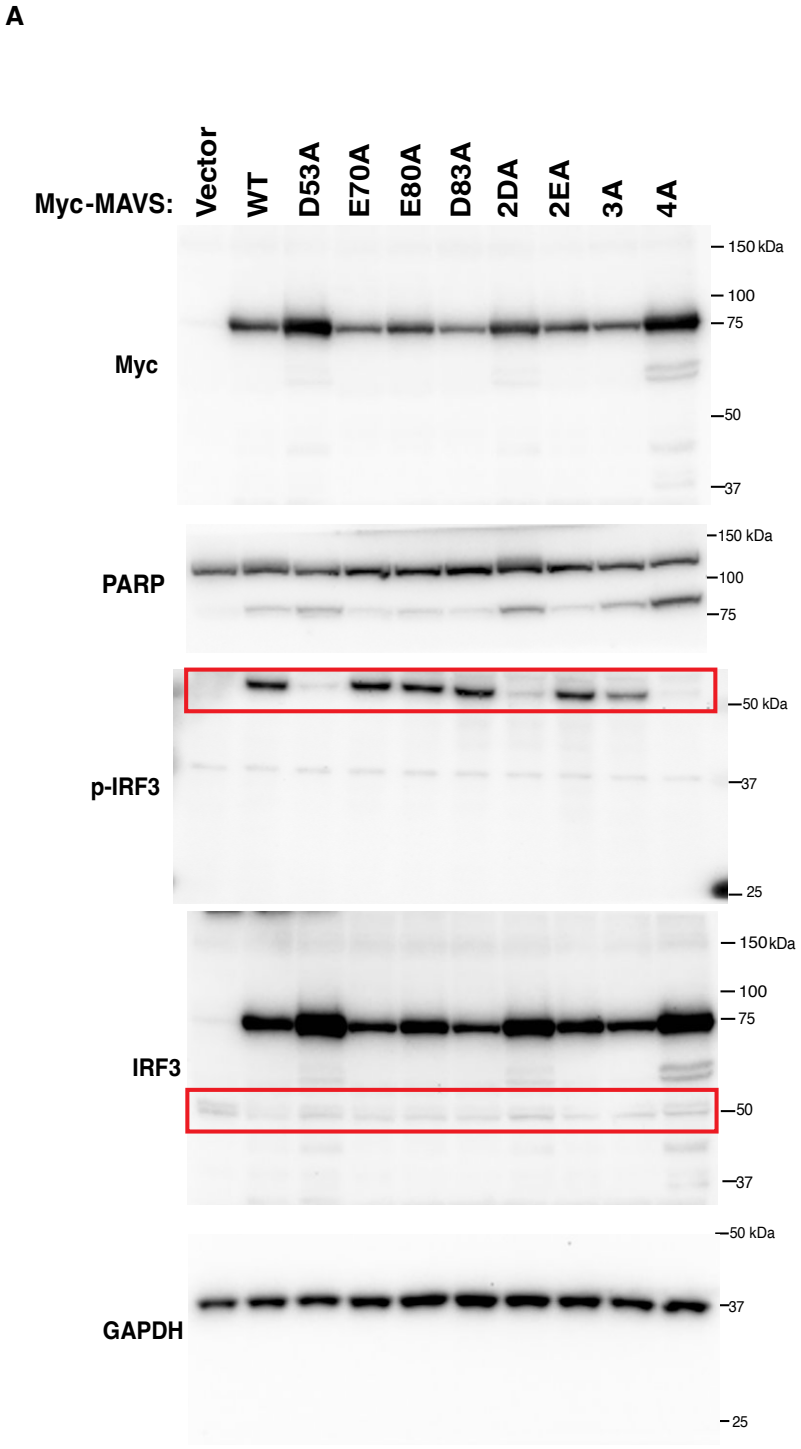

Fig. S60.
A. These are uncropped blots corresponding to Fig. S14A.

Fig. S61.

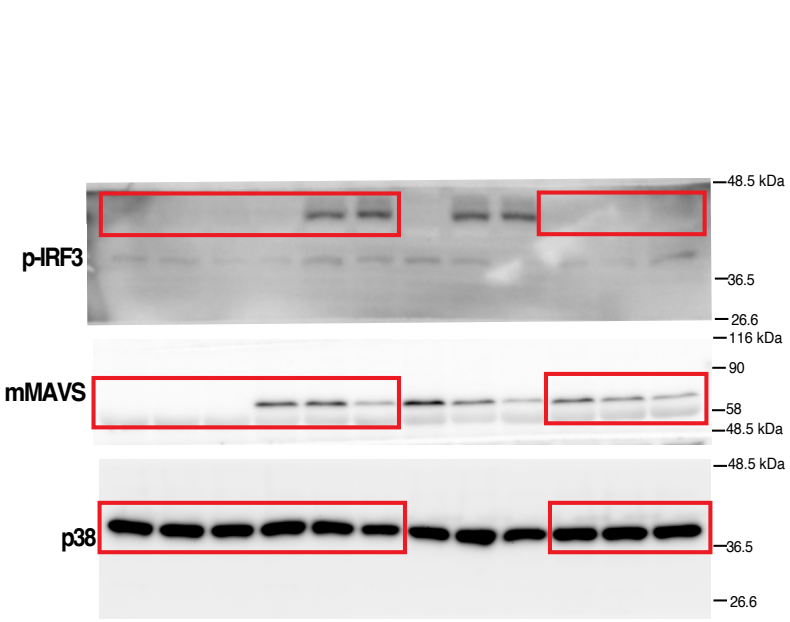

Fig. S61.
A. These are uncropped blots corresponding to Fig. S15A.

Fig. S62.

A

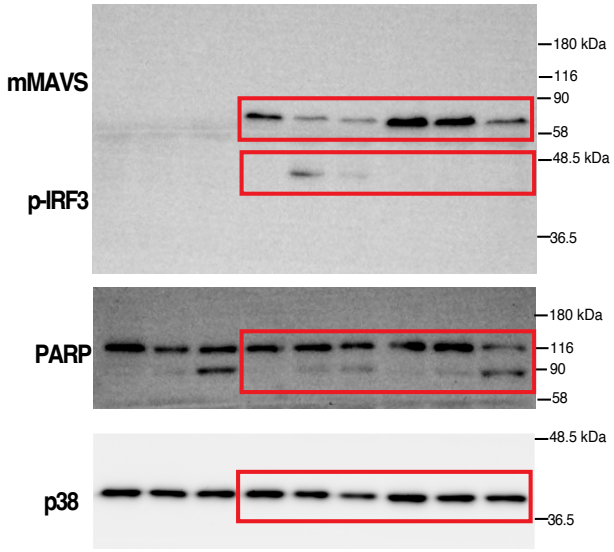

Fig. S62.
A. These are uncropped blots corresponding to Fig. S15B.

Fig. S63.

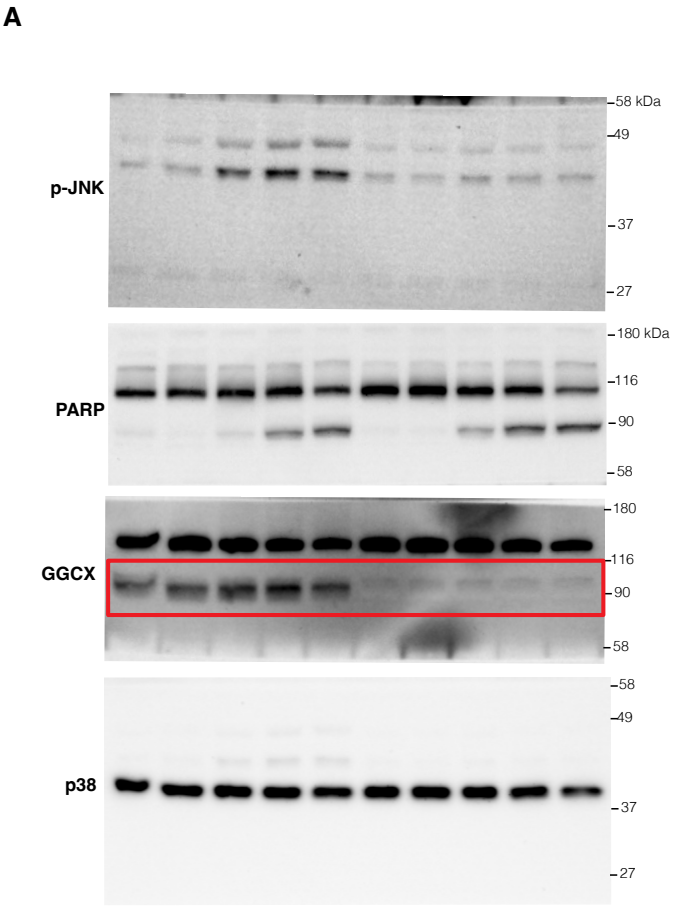

Fig. S63.
A. These are uncropped blots corresponding to Fig. S17A.

Fig. S64.

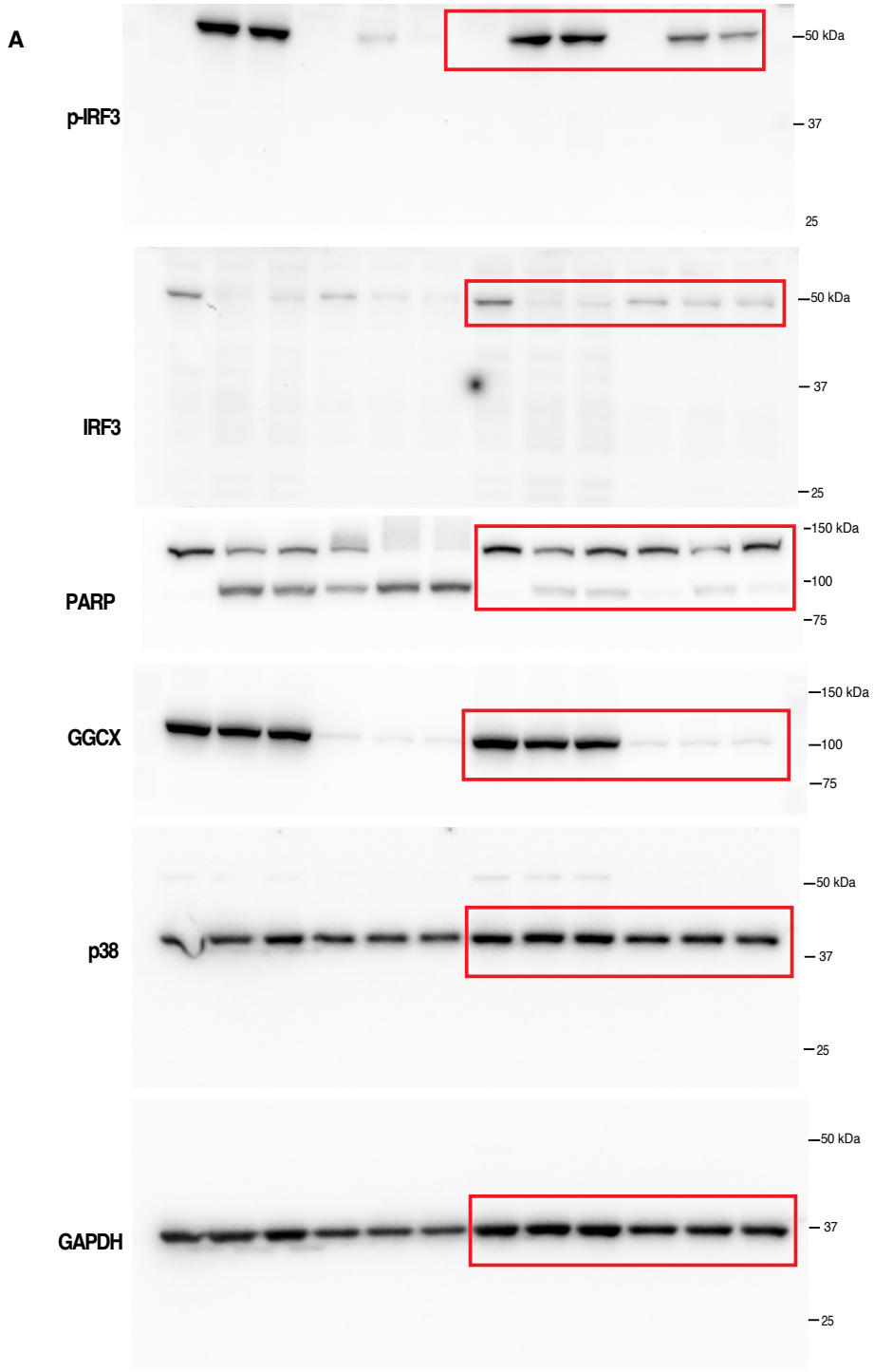

Fig. S64.
A. These are uncropped blots corresponding to Fig. S18B. Most of the blots shown here were derived from regions of the same gel used for Fig. S36. Samples with zVAD treatment (this figure) and without zVAD treatment were run in parallel and developed together on the same membrane.

Fig. S65.

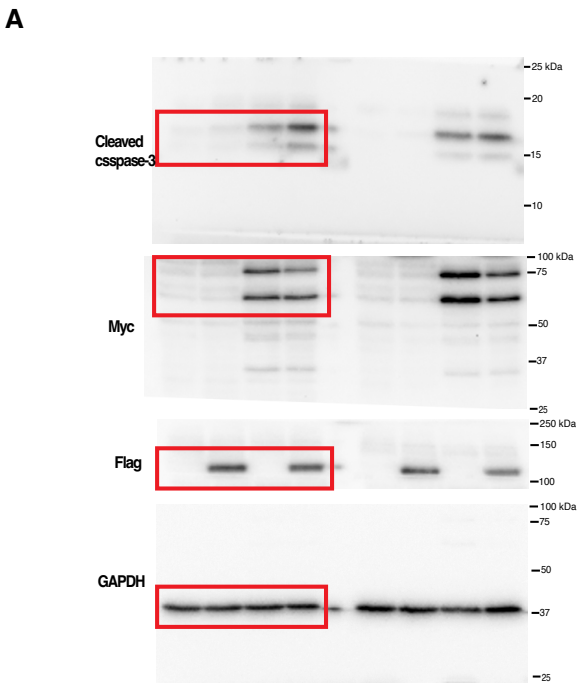

Fig. S65.
A. These are uncropped blots corresponding to Fig. S20C.

Fig. S66.

A

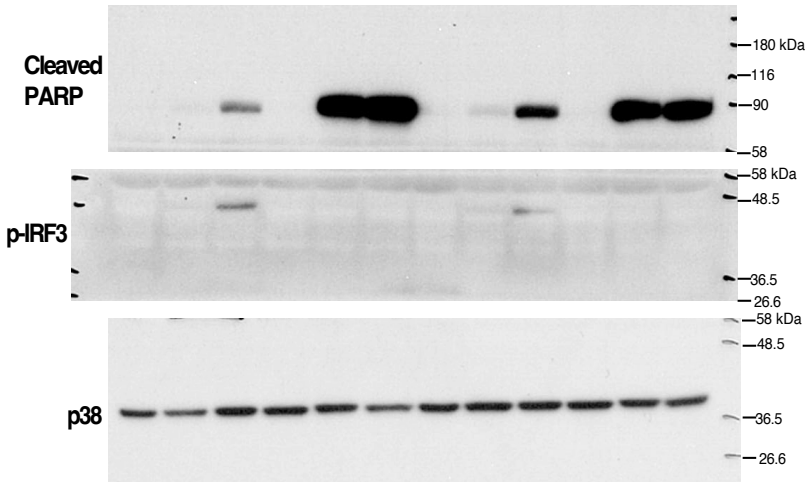

Fig. S66.
A. These are uncropped blots corresponding to Fig. S21B.

Fig. S67.

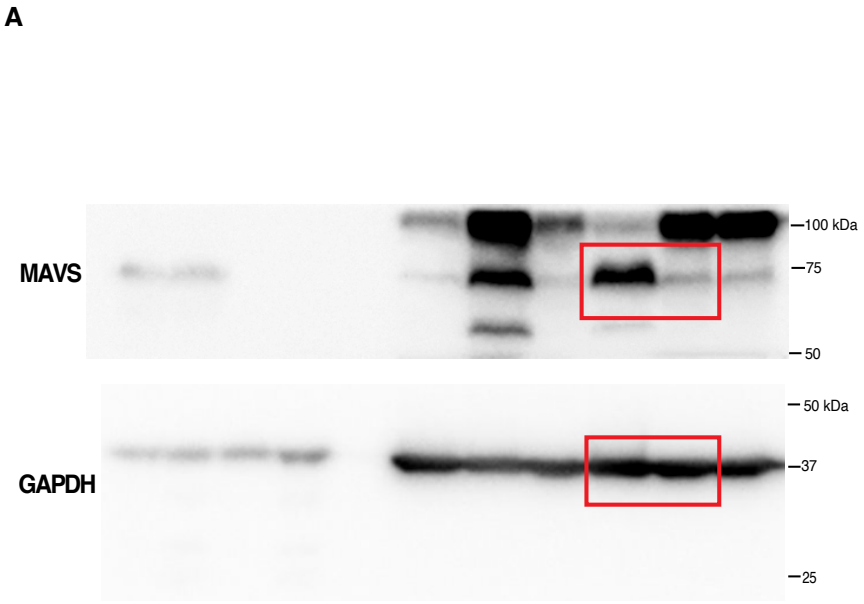

Fig. S67.
A. These are uncropped blots corresponding to Fig. S26C.

Table S1. (separate file)
Table of differentially associated proteins between MAVS WT and MAVS 4A. The table includes log_2 fold changes (log_2 FC) and corresponding P values for each protein.